



Cite this: DOI: 10.1039/c9cs00635d

Towards high-performance solid-state Li–S batteries: from fundamental understanding to engineering design

 Xiaofei Yang, Jing Luo and Xueliang Sun *

Solid-state lithium–sulfur batteries (SSLBs) with high energy densities and high safety have been considered among the most promising energy storage devices to meet the demanding market requirements for electric vehicles. However, critical challenges such as lithium polysulfide shuttling effects, mismatched interfaces, Li dendrite growth, and the gap between fundamental research and practical applications still hinder the commercialization of SSLBs. This review aims to combine the fundamental and engineering perspectives to seek rational design parameters for practical SSLBs. The working principles, constituent components, and practical challenges of SSLBs are reviewed. Recent progress and approaches to understand the interfacial challenges via advanced characterization techniques and density functional theory (DFT) calculations are summarized and discussed. A series of design parameters including sulfur loading, electrolyte thickness, discharge capacity, discharge voltage, and cathode sulfur content are systematically analyzed to study their influence on the gravimetric and volumetric energy densities of SSLSB pouch cells. The advantages and disadvantages of recently reported SSLBs are discussed, and potential strategies are provided to address the shortcomings. Finally, potential future directions and prospects in SSLSB engineering are examined.

Received 12th December 2019

DOI: 10.1039/c9cs00635d

rsc.li/chem-soc-rev

1. Introduction

Lithium–sulfur (Li–S) batteries have been considered as one of the most promising candidates to meet the energy storage

demand of electric vehicles and portable electronic devices due to their high theoretical energy density of 2600 Wh kg^{-1} , low cost, natural abundance, and environmental friendliness.^{1–5} In the last few decades, studies on Li–S batteries have mainly focused on solving problems related to active materials such as polysulfide shuttling effects, volumetric changes during charge/discharge, and concerns regarding the insulating properties of S and Li_2S

Department of Mechanical and Materials Engineering, University of Western Ontario, London, ON N6A 5B9, Canada. E-mail: xsun9@uwo.ca


Xiaofei Yang

Dr Xiaofei Yang is currently a postdoctoral associate in Prof. Xueliang (Andy) Sun's Nano-materials and Energy Group. He received his BE degree in Chemical Engineering from Anhui University, China, in 2013 and PhD degree from Dalian Institute of Chemical Physics, Chinese Academy of Sciences, China, in 2018, under the supervision of Prof. Huamin Zhang. His research interests focus on Li–S batteries, all-solid-state Li-ion and Li–S batteries and battery interface studies via synchrotron X-ray characterizations.


Jing Luo

Jing Luo received her BS degree in Chemical Engineering from the University of Illinois–Urbana Champaign (USA) in 2013 and MS degree under the supervision of Prof. Nae-Lih Wu from National Taiwan University (Taiwan) in 2016. She is now pursuing her PhD degree in Prof. Xueliang (Andy) Sun's group at the University of Western Ontario, Canada. Her current research interests focus on solid electrolytes design and all-solid-state lithium batteries.

since the report of CMK-3 as an effective host for sulfur.^{6–12} Great progress has been achieved in terms of energy density, power density, and cycling life. Promising Li–S batteries exhibited a long cycling life of more than 1500 cycles,^{13,14} high C-rate performance of up to 40C,¹⁵ and high sulfur loadings of over 20 mg cm⁻².^{16,17} More importantly, rechargeable and primary Li–S pouch cells can achieve high practical energy densities of 616 W h kg⁻¹ and 916 W h kg⁻¹, respectively.³ However, despite the great achievements of the liquid electrolyte based Li–S batteries, the electrochemical and thermal instabilities of the system lead to potential safety risks.¹⁸ Replacing the liquid electrolytes by solid-state electrolytes (SSEs) that have high ionic conductivities, wide electrochemical stability windows, and superior thermal stability is a promising strategy for constructing feasible solid-state Li–S batteries (SSLBs).¹⁹

Recently, the applications of different kinds of SSEs such as polymer-based electrolytes (including gel polymer electrolytes (GPEs) and solid polymer electrolytes (SPEs)),^{20–26} ceramic electrolytes (mainly oxide-based electrolytes, sulfide-based electrolytes, and their derivatives)^{27–36} and hybrid electrolytes^{37–44} in SSLBs have been reported. These studies mostly focus on solving the electrode–electrolyte interfacial issues at the research stage. Guo *et al.*, Manthiram *et al.*, Zhang *et al.*, and Yang *et al.* have reviewed interface related topics.^{45–48} In fact, challenges confronting practical SSLBs are more than interfacial issues.

SSLBs using different SSEs could undergo different electrochemical reaction mechanisms and therefore different challenges. For example, using polymer electrolyte in SSLBs, the active sulfur is discharged into Li₂S₂/Li₂S *via* multi-step reactions similar to the liquid ether-based Li–S batteries,^{20,23} in which the shuttling effect is a major concern. Differently, SSLBs based on ceramic electrolytes undergo a one-step solid–solid reaction mechanism, where large interfacial resistances between ceramic grain boundaries and between mismatched electrolyte/electrode interfaces are more challenging

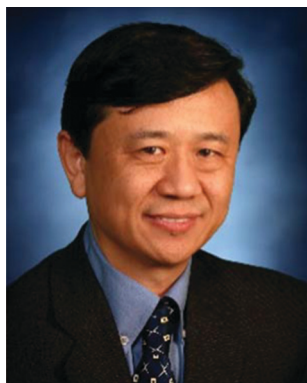
problems;^{45,46,49} meanwhile, Li dendrite growth is more serious in the absence of lithium polysulfides (LiPSs). As for sulfide-based SSEs such as Li₁₀MP₂S₁₂ (M = Ge, Sn, Si) families, even though they have high ionic conductivities on the order of 10⁻³–10⁻² S cm⁻¹, their poor stability against Li metal anodes and narrow electrochemical stability windows seriously limit their application as an individual SSE in SSLBs.^{50,51} In this context, the development of high-performance SSLBs shall focus not only on the interfacial issues, but also on comprehensive management of volumetric fluctuations during cycling, Li dendrite problems, and electrochemical/chemical stability of SSEs against electrodes.

Moreover, practical SSLBs for commercial electronic devices and electric vehicles require engineering efforts to consider a complete assembly of SSLBs and to bridge the gap between fundamental research and practical applications. High-performance SSLB design needs to comprehensively consider energy and power densities in terms of gravimetric and volumetric bases as well as manufacturing costs. At the current stage, poor rate performance (typically <0.3 mA cm⁻²) due to low Li⁺/e⁻ conductivity of sulfur electrodes and interfacial problems is still limiting the improvements of power density;^{34,52,53} low active material loadings and thick SSEs significantly lower the practical energy density;³ SSEs such as Li₁₀GeP₂S₁₂ (LGPS), LPS (including Li₇P₃S₁₁ and Li₃PS₄) and Li₇La₃Zr₂O₁₂ (LLZO) are expensive for pouch cell type SSLBs. It is urgent to explore strategies for improving the power and energy densities while lowering cost.

This review aims to provide an overview of SSLBs and challenges related to various types of SSEs, so as to offer guidance for reasonable structural and parameter designs for practical SSLBs. Working principles, challenges, and materials design in various SSLB systems are introduced as the basis. Recent progress in solving critical problems such as LiPSs shuttling effects, interfacial issues and Li dendrites is summarized to provide a library of approaches. Advanced characterization techniques such as nuclear magnetic resonance (NMR), *in situ* studies (using X-ray photoelectron spectroscopy (XPS), transmission electron microscopy (TEM), three-dimensional magnetic resonance imaging (3D MRI), *etc.*), and density functional theory (DFT) calculations are systematically reviewed to create a toolbox for interfacial and mechanistic studies. Following that, engineering technical improvements and relationships between key parameters (*e.g.* sulfur loading, electrolyte thickness, sulfur content, porosity in the cathode) and energy density (gravimetric and volumetric energy density) will be clarified. A comparison and statistical analysis of the reported SSLBs shall clarify the determining factors of SSLB performance and inspire potential solutions and future directions.

1.1 Principles of SSLBs

A typical SSLB is composed of a Li metal anode, an SSE, and a sulfur-based cathode. Fig. 1 schematically presents three different SSLB configurations and two typical charge/discharge voltage profiles undergoing distinct reaction mechanisms. Generally, during the discharge process, the Li metal



Xueliang Sun

Prof. Xueliang (Andy) Sun is a Canada Research Chair in Development of Nanomaterials for Clean Energy, Fellow of the Royal Society of Canada and Canadian Academy of Engineering and Full Professor at the University of Western Ontario, Canada. Dr Sun received his PhD in materials chemistry in 1999 from the University of Manchester, UK, which he followed up by working as a postdoctoral fellow at the University of British Columbia,

Canada, and as a Research Associate at L' Institut National de la Recherche Scientifique (INRS), Canada. His current research interests are focused on advanced materials for electrochemical energy storage and conversion.

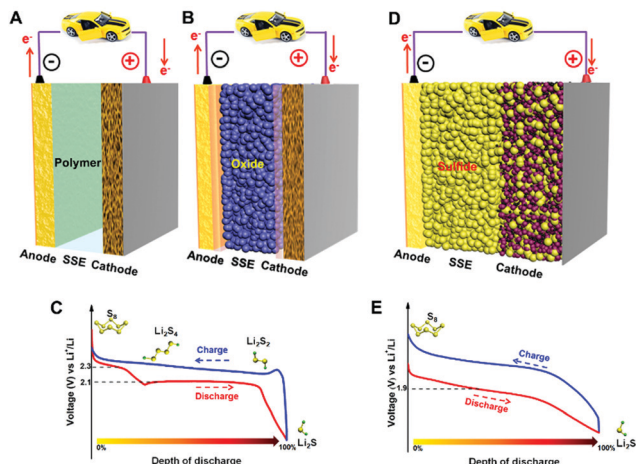


Fig. 1 Schematic configurations of SSLSBs using (A) polymer, (B) oxide-based SSEs and (D) sulfide based SSEs. Typical charge/discharge voltage profiles of (C) solid-liquid dual-phase Li-S reactions and (E) solid-phase Li-S reactions.

anode loses electrons to an outer circuit and forms Li ions (Li^+) that diffuse to the cathode side through the SSE; at the cathode, Li^+ electrochemically reacts with the S active materials to form LiPSs or Li_2S . Fig. 1A and B present the configurations of SSLSBs using polymer-based SSEs and oxide-based SSEs, respectively. The rigid property of oxide-based SSEs can cause serious mismatch problems towards electrodes, limiting their application in SSLSBs as a single component. In most cases, oxide-based SSEs are coupled with polymer electrolytes, liquid electrolytes, or ionic liquids as hybrid SSEs to address the interface with electrodes.⁵⁴ In the presence of liquid electrolytes or polymer electrolytes, the SSLSBs usually demonstrate a typical discharge-charge profile corresponding to a solid-liquid dual-phase reaction, similar to that of Li-S cells using ether-based liquid electrolytes.⁵⁵ As shown in Fig. 1C, the two plateaus in the discharge profile correspond to the two-step reduction from sulfur to Li_2S . At the first plateau around 2.3 V, S_8 is reduced to Li_2S_4 . Based on 1/2 electron transfer per sulfur atom, the SSLSBs have the potential to deliver a theoretical capacity of 418 mA h g^{-1} at this plateau. As the discharge continues, Li_2S_4 is further reduced to Li_2S at the plateau around 2.1 V, corresponding to a theoretical capacity of 1254 mA h g^{-1} . During charging, Li_2S is oxidized back to S_8 via the formation of intermediate LiPSs.

In the absence of solvents to dissolve LiPSs, SSLSBs follow an alternative solid-solid reaction route that involves direct conversions between S and Li_2S without intermediate LiPSs. This reaction route is common in all-ceramic-based SSE systems, especially in sulfide-based SSE systems (Fig. 1D). Such a one-step discharge is also observed in liquid carbonate-based Li-S cells with bonded sulfur or a perfect coating on the sulfur cathode, where LiPS dissolution cannot occur. The “solid-phase” reaction exhibits a single discharge plateau at around 2.0 V (Fig. 1E). Occasionally, in SSLSBs using hybrid SSEs with a small amount of liquid or polymer electrolyte, both solid-liquid reactions and solid-solid reactions occur simultaneously, so

that a mixed discharge profile presents multi-discharge plateaus. Such a reaction route is also known as a quasi-solid-phase reaction route, which shares characteristics of the two existing reaction routes. The two different electrochemical reaction routes of SSLSBs lead to different challenges and materials design in SSEs and sulfur-based cathodes. In the following sections, SSLSB components, fundamental challenges, and strategies for material/structural designs for SSEs and sulfur-based cathodes are reviewed and discussed in detail.

1.2 Components of SSLSBs

1.2.1 Anodes.

In SSLSBs, metallic Li is an ultimate anode choice due to its ultra-high theoretical capacity (3860 mA h g^{-1}) and lowest negative electrochemical potential (-3.040 V vs. the standard hydrogen electrode), resulting in Li-S batteries with a high theoretical energy density of 2600 W h kg^{-1} (Fig. 2).⁵⁶ However, Li metal anodes still suffer from Li dendrite problems during Li plating/stripping because of the unstable Li metal/SSE interface. Li dendrite induced short circuit can lead to battery failure and safety risks in flammable liquid-containing SSLSB systems. Moreover, the highly reducing Li metal is reactive to many highly ionic conductive SSEs such as LGPS.⁵⁷ As a compromise, the Li_3PS_4 SSE with better stability towards Li metal but a lower ionic conductivity of $\sim 10^{-4} \text{ S cm}^{-1}$ is often used in SSLSBs, which thus exhibit poor rate performance at room temperature (RT).⁵⁸⁻⁶⁰ Alternatively, Li-M alloys ($M = \text{In, Sn, Ge}$)^{28,35,61-63} and metallic In^{29,64} are chosen as anodes to avoid Li dendrites and alleviate the side reactions. The Li component is stored in an ionic form rather than a metallic

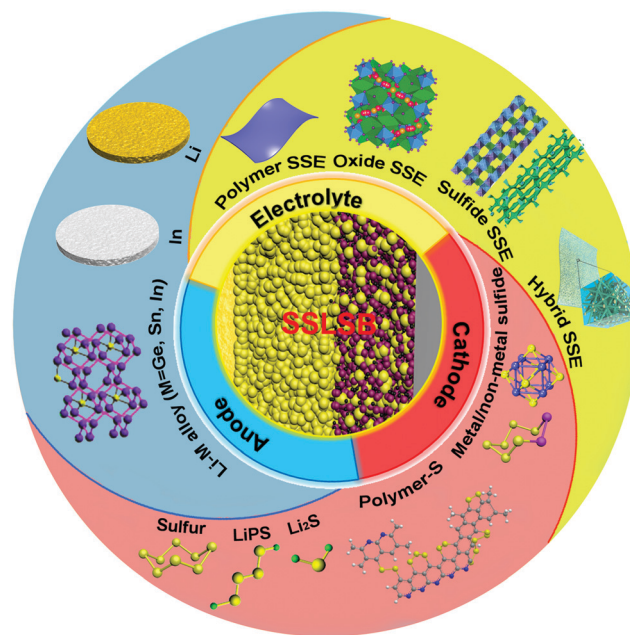


Fig. 2 Typical examples of anodes, SSEs, and cathodes for SSLSBs. Reprinted with permission from ref. 77, Copyright 2015, Elsevier, Ltd. Reprinted with permission from ref. 96, Copyright 2016, National Academy of Sciences. Reprinted with permission from ref. 82, Copyright 2011, Nature Publishing Group. Reprinted with permission from ref. 83, Copyright 2016, Nature Publishing Group.

form in Li–M alloys, which is beneficial for suppressing Li dendrites and stabilizing the Li–M alloy/SSE interface. However, the relatively higher operating potentials of Li–M alloys and metallic In inevitably lower the energy density.²⁸ Another limitation is that the metallic In anode requires a Li-containing sulfur-based cathode such as Li₂S, where the cathode itself has unsolved challenges.

1.2.2 Solid-state electrolytes

1.2.2.1 Polymer-SSEs. As an important component of SSLSBs, SSEs act as both a separator and a Li⁺ conductor. Several kinds of SSEs such as polymer SSEs, ceramic SSEs (including oxide- and sulfide-based SSEs), and hybrid SSEs are investigated in SSLSBs.

Polymer-based SSEs can be classified into GPEs and SPEs depending on whether liquid electrolytes/solvents are involved or not.⁶⁵ GPEs are popular due to their flexibility, good interfacial compatibility, and high ionic conductivity comparable to liquid electrolyte.²⁰ Nevertheless, GPEs still have safety concerns in combination with metallic Li anodes due to the liquid electrolyte component. Eliminating liquid electrolytes for safety consideration, SPEs are attractive alternatives but limited by their low ionic conductivities (typically 10⁻⁸–10⁻⁶ S cm⁻¹) at RT.⁶⁶ In most cases, the SPE-based SSLSBs need to be operated at an elevated temperature over 60 °C.^{67–70} The poor mechanical properties of SPEs at working temperatures often fail to suppress Li dendrite growth.^{71,72} Moreover, the high solubility of LiPSs in the common polymer matrixes can cause LiPSs shuttling problems. To address the challenges of SPEs for SSLSBs, the development of cross-linked SPEs and incorporation of ceramic fillers are the popular strategies.^{37–39,73} The decreased crystallinity of polymers and increased mechanical strength can lead to improvements in ionic conductivity and Li dendrite suppression. Filler added SPEs are also a known class of hybrid SSEs to be discussed in Section 1.2.2.4.

1.2.2.2 Oxide-SSEs. As another major category of SSEs, inorganic SSEs with high RT ionic conductivities of 10⁻⁴–10⁻² S cm⁻¹ have attracted great research attention in recent years. Inorganic SSEs include two widely studied families, oxide-based SSEs and sulfide-based SSEs. Developed oxide-based SSEs primarily involve NASICON-type Li_{1+x}Al_xTi_{2-x}(PO₄)₃ (LATP) and Li_{1+x}Al_xGe_{2-x}(PO₄)₃ (LAGP),^{74,75} garnet-type Li₂La₃Zr₂O₁₂ (LLZO),^{76,77} and perovskite-type Li_{3x}La_{(2/3)-x}TiO₃ (LLTO),⁷⁸ which have RT ionic conductivities of over 10⁻⁴ S cm⁻¹. One drawback of the single-component oxide-based SSEs is the large electrolyte/electrode interfacial resistance that limits their application in SSLSBs. Often, oxide-based SSEs are coupled with polymer-based SSEs, liquid electrolytes, or ionic liquids to reduce the interfacial resistance. These classic hybrid SSEs will be discussed in Section 1.2.2.4.

1.2.2.3 Sulfide-SSEs. Among all SSEs, sulfide-based SSEs present the highest ionic conductivities as high as beyond 10⁻² S cm⁻¹ at RT, being comparable to liquid electrolytes. Sulfide-based SSEs can be further divided into glass, crystalline, and glass-ceramic sulfide SSEs based on their different crystal structures. The xLi₂S(1 - x)P₂S₅ and the xLi₂S(1 - x)SiS₂ systems are the two representatives of glass sulfide SSEs,

exhibiting ionic conductivities of over 10⁻⁴ S cm⁻¹ at RT.^{79,80} Compared with glass sulfide SSEs, the glass-ceramic and crystalline sulfide SSEs exhibit higher ionic conductivities and some of them are comparable to liquid electrolytes. For instance, the glass-ceramic Li₇P₃S₁₁ shows a high RT ionic conductivity of 1.7 × 10⁻² S cm⁻¹.⁸¹ Crystalline Li₁₀MP₂S₁₂ (M = Ge, Sn, Si) and their derivatives (e.g. Li_{9.54}Si_{1.74}P_{1.44}S_{11.7}Cl_{0.3}, LiSiPSCl) also exhibit particularly outstanding ionic conductivities of over 10⁻² S cm⁻¹ at RT.^{82–86} Despite the high ionic conductivity of sulfide SSEs, there are still many issues to be solved for practical applications. Interfacial issues, narrow electrochemical stability windows (typically in the range of 1.5–2.5 V), chemical instability in the ambient environment, and reactivity with Li metal anodes are major obstacles.⁵⁰

1.2.2.4 Hybrid-SSEs. To compromise the drawbacks of single-component SSEs, a new concept of hybrid SSE is developed by rationally combining two or more SSEs. Hybrid SSEs intend to balance the merits and drawbacks of each component. The most common hybrid SSEs are composed of a soft component (such as SPE or liquid electrolyte) and a rigid inorganic SSE, where the inorganic SSEs contribute to a high ionic conductivity/mechanical strength and the flexible component ensures a good electrolyte/electrode interface. Before the development of high ionic conductive inorganic SSEs, Al₂O₃,^{87,88} TiO₂,^{88–90} ZrO₂,⁹¹ and SiO₂^{37,92,93} were used as effective fillers to improve the ionic conductivity of SPEs by almost two orders of magnitude to the 10⁻⁵ S cm⁻¹ level at RT. The improvement in ionic conductivity is mainly attributed to the formation of Li⁺-filler complexes by Lewis acid–base interactions between the functional groups on the surface of fillers and acidic Li⁺. The lowered reorganization tendency promotes Li⁺ fast transport on the fillers' surface.⁹⁴ Beyond insulating fillers, oxide-based SSEs fillers are more favorable that enable high RT ionic conductivities of over 10⁻⁴ S cm⁻¹ while maintaining mechanical flexibility.^{95–97} The application of sulfide-based SSEs as fillers is sparse because of the poor chemical stability of sulfides in solvents.^{98,99} Another configuration of hybrid electrolyte sandwiches the oxide SSEs between two layers of SPEs, liquid electrolytes, or ionic liquids. Benefitting from the dense structure of oxide-based SSE pallets and high Young's modulus, the LiPS shuttling effects and Li dendrite problems in SSLSBs are significantly suppressed. Nevertheless, the risk of reducing ionic conductivity and safety hazards should be balanced during the introduction of SPEs and liquid components.

1.2.2.5 Other-SSEs. Additionally, other novel high-ionic conductive SSEs like halide Li₃MX₆ (M = In, Y, Er; X = Cl, Br) and Li₂(BH₄)(NH₂) 0.7Li(CB₉H₁₀)–0.3Li(CB₁₁H₁₂) with high ionic conductivities of over 10⁻³ S cm⁻¹ show potential application in SSLSBs.^{100–106} The air stability of halide SSEs and thermal stability of the Li₂(BH₄)(NH₂) 0.7Li(CB₉H₁₀)–0.3Li(CB₁₁H₁₂) SSE show promise for easy handling in a dry room and SSLSB operation under all climate conditions. The Li₂(BH₄)(NH₂) 0.7Li(CB₉H₁₀)–0.3Li(CB₁₁H₁₂) SSE based SSLSBs achieve amazing electrochemical performance at RT. Specifically, the

0.7Li(CB₉H₁₀)-0.3Li(CB₁₁H₁₂) SSE presents a high RT ionic conductivity of $6.7 \times 10^{-3} \text{ S cm}^{-1}$. High stability against Li metal is another advantage, evidenced by the stable cycling of Li-Li symmetric cells for over 300 cycles with an extremely low overpotential of around 6–7 mV at 0.2 mA cm^{-2} . With a sulfur loading of 2.5 mg cm^{-2} , the SSLSBs achieved a high reversible discharge capacity of 1239 mA h g^{-1} after 20 cycles at 1C ($25 \text{ }^\circ\text{C}$) and 1017 mA h g^{-1} after 100 cycles at 5C ($60 \text{ }^\circ\text{C}$).¹⁰⁵

1.2.3 Cathodes. Various types of sulfur cathodes have been developed for liquid Li-S batteries, with S/C composites as the most common cathodes. In most cases, in order to solve the issues of insulating properties of S/Li₂S and accommodating volumetric expansion, the sulfur is confined in porous conductive matrixes with high specific surface areas and pore volumes.^{10,107–112} Sometimes, LiPSs and Li₂S are used as the starting active materials.^{27,58} A group of cathodes involve bonded S in polymers (polymer-S) such as polyacrylonitrile (PAN)-S,^{113,114} 1,3-diisopropenylbenzene (DIB)-S^{115,116} and trithiocyanuric acid (TTCA)-S^{117,118} by polymerizing the sulfur chains into the scaffold of polymers. Therefore, LiPS dissolution and shuttling effects are reduced. The PAN-S is a successful example that can be operated in a carbonate electrolyte for a thousand cycles *via* solid-phase reactions.

Intuitively, the sulfur cathodes should be universal for both liquid Li-S batteries and SSLSBs, but in fact, the different reaction mechanisms in SSLSBs require special designs of materials and structures. In the SSLSB systems involving polymer and/or liquid electrolytes, most cathode designs adopt from the liquid Li-S systems based on the solid-liquid dual-phase reaction mechanism. The formation of soluble LiPS intermediates (except for the polymer-S type cathodes) can

facilitate the electrochemical reactions during charging/discharging. Meanwhile, the good wettability of liquid electrolytes or the semi-molten polymers on the S/C composite and other cathode materials enables low interfacial resistance. However, it is well known that the electrochemical reaction can only occur at the tri-phase interface of the active material, Li⁺ conductor, and electronic conductor. The cathode designs for the inorganic SSE based SSLSB systems are more complicated, in which the slow solid-phase reactions involve direct conversions between sulfur and Li₂S during charging/discharging. Even upon confining sulfur in a porous carbon matrix, the electrochemical reaction will be limited by the poor access of SSEs for Li⁺ in spite of the fast electron transport. Hence, the concept of a balanced cathode design mixing active materials, SSEs and carbon additives is widely adopted. In addition to the development of nano-sized active materials/SSEs and liquid-phase SSE coating on the surface of active materials to create more available tri-phase interfaces and facilitate Li⁺ transport,^{31,32,119} some metallic or non-metallic elements with higher electronic conductivity are combined with sulfur as active materials to enhance the electrochemical kinetics. For instance, sulfur-rich SeS_x,¹²⁰ Li₃PS_{4+x},⁶⁰ P₂S_{5+x},³⁴ as well as metal sulfides such as Co₉S₈,¹¹⁹ FeS_x,¹²¹ CuS,⁶² and MoS₃,^{122–124} have been reported and have shown promising electrochemical performance. Drawbacks include lower theoretical capacities and lower discharge voltages and thus lower energy density for SSLSBs.

1.3 Fundamental challenges of SSLSBs

Despite the advantages and great progress in the development of SSLSBs, fundamental challenges are still there, as summarized in Fig. 3. These challenges need to be overcome in order to

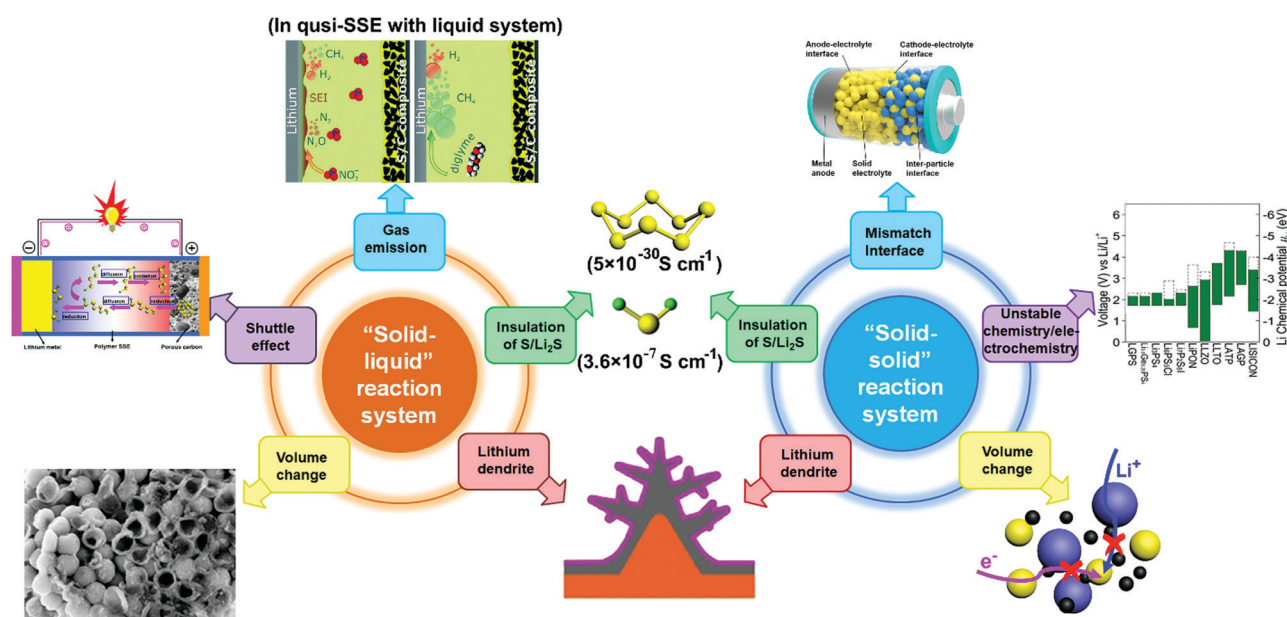


Fig. 3 Challenges in SSLSBs systems based on solid-liquid or solid-solid mechanisms. Reprinted with permission from ref. 142, Copyright 2013, American Chemical Society. Reprinted with permission from ref. 127, Copyright 2016, Royal Society of Chemistry. Reprinted with permission from ref. 3, Copyright 2018, Springer. Reprinted with permission from ref. 143, Copyright 2016, Wiley-VCH. Reprinted with permission from ref. 144, Copyright 2018, Cell press. Reprinted with permission from ref. 50, Copyright 2015, American Chemical Society.

improve the electrochemical performance and eventually realize commercialization. The solid–liquid dual-phase and solid-phase reaction systems are separately discussed here. In the solid-phase reaction system, the interfacial problems and chemical/electrochemical instabilities are the main issues, while the shuttling effects and gas emission (in liquid-containing systems) remain key drawbacks in the solid–liquid dual-phase reaction systems. Nevertheless, these two different reaction mechanisms share some common challenges such as the insulating properties of S/Li₂S, Li dendrite growth, and volumetric changes during cycling.

(1) The “shuttle effect”, a common problem in liquid Li–S batteries, results from the dissolution of LiPSs into the electrolyte. Under a concentration gradient and electric field force, the LiPSs shuttle between the anode and cathode, leading to the loss of active material, Li metal anode corrosion, and low Coulombic efficiencies (CEs).^{3,125,126} These problems also occurred in the liquid electrolyte and polymer involved SSLSB systems due to the high solubility of LiPSs in the matrixes.

(2) Gas emission. During the charge/discharge process, complex side reactions occur at the interface of the electrolyte and Li metal (in liquid electrolyte containing systems) and produce gaseous by-products such as CH₄, H₂, N₂, N₂O, *etc.*¹²⁷ In sealed Li–S battery systems, the increased internal pressure will worsen the electrochemical performance and result in safety issues.

(3) Mismatch interface. In solid-phase systems, rigid ceramic SSEs are widely used. In the absence of soft polymers and liquid electrolytes as the interfacial modification layer, the SSEs contact with the electrode materials and electrodes (anode and cathode) by point-to-point contacts. The Li⁺/e[−] transport across the interface is significantly limited, resulting in low electrochemical kinetics and unsatisfactory electrochemical performance of SSLSBs.

(4) Chemical/electrochemical instabilities. Most sulfide-based SSEs are unstable in the ambient environment. Exposure to O₂ and H₂O generates hazardous H₂S followed by SSE decomposition.¹²⁸ Moreover, such sulfide-SSEs present a discharge plateau of over 2.0 V and deliver capacities of 150–300 mA h g^{−1}.^{129,130} That is to say, the sulfide-SSE will participate in electrochemical reactions in the operating voltage windows of SSLSBs. The effect of Li de-intercalation from sulfide-SSEs on the ionic conductivity is still unclear. Even without charging or discharging, particular SSEs such as LGPS and LiSiPSCl are reactive with the Li anode upon contact. In the presence of Li metal, the Ti⁴⁺ in LATP and LLTO is readily reduced to low-valence Ti^{x+}, significantly lowering the ionic conductivity of SSEs.^{131,132}

(5) Insulating properties of S and Li₂S. Using S, LiPSs, or Li₂S as the active materials, the charge/discharge end products are S and Li₂S, showing natural electrical conductivities of 5×10^{-30} S cm^{−1} and 3.6×10^{-7} S cm^{−1} at 25 °C, respectively.^{133–135} Moreover, the Li⁺ transport in S and Li₂S is also extremely slow. The conversion reaction between S and Li₂S is limited, especially in the SSLSB systems where sulfur is not confined in the carbon matrixes, resulting in low active materials utilization and discharge capacity output.

(6) Lithium dendrite growth. The non-uniform charge distribution and the existence of defects on the Li metal surface result in unstable Li deposition and Li dendrite formation.^{56,136,137} The Li dendrites can easily penetrate the soft SPE and cause internal short-circuits. Also, growth of Li dendrites along the crystal boundaries in ceramic SSEs can cause cell short circuit despite their high mechanical strength.^{138–140} Moreover, the evolution of dead Li from dendrites during the repeated charging/discharging process increases interfacial resistance and shortens battery lives. The lithium dendrite growth in solid-phase reaction systems is more serious than that of solid–liquid dual-phase reaction systems because of the absence of LiPSs, where LiPSs can react with Li and consume Li dendrite to some extent.

(7) Large volumetric changes during charging/discharging. Because of the different densities of Li₂S and S (1.66 g cm^{−3} vs. 2.07 g cm^{−3}), large volumetric changes occur upon de-lithiation of Li₂S and lithiation of sulfur. In solid–liquid dual-phase systems, the active materials in most cases are encapsulated in conductive matrixes. The volumetric changes can cause pulverization of the cathode materials and cathode structural disintegration, resulting in fast capacity decay.^{6,7,141,142} In solid-phase reaction systems with a mixture of active materials, SSEs, and conductive additives, the volumetric changes result in detachment of active materials from the Li⁺/e[−] conductors, leading to a rapidly increased overpotential and fast capacity decay.

2. Rational designs towards high-performance SSLSBs

Different strategies are proposed to solve the challenges and improve the comprehensive electrochemical performance of SSLSBs. In solid–liquid dual-phase reaction systems, the volumetric changes and insulating properties of S/Li₂S can be well-resolved by encapsulating active materials in various porous conductive matrixes.^{145–147} Increasing efforts are dedicated to addressing the shuttle effects, lithium dendrite problems, and instability between the Li anode and electrolytes. In solid-phase reaction systems, the development of new electrolytes with high stability against H₂O/O₂ and Li anodes as well as wide electrochemical stability windows are in progress.^{103–106} Strategies for materials and structural designs, such as building conductive networks and decreasing the size of active materials, are proposed to alleviate the drawbacks of insulating properties of S/Li₂S. Interfacial modifications have also drawn much attention that aim to decrease the interfacial resistance, facilitate the Li⁺/e[−] transport, and suppress Li dendrite growth along the grain boundary. The interfacial modifications for Li dendrite suppression are discussed as a Li protection method in Section 2.3. Moreover, strategies for alleviating volume changes to enhance the electrochemical performance are summarized. Subsequently, various *ex/in situ* characterizations and DFT calculations as power tools for interfacial study are reviewed. Finally, the development of Li protection methods will be discussed.

2.1 Electrolyte designs for suppressing LiPS shuttling

“Shuttle effects” refer to the problems caused by the soluble LiPSs shuttling between the anode and the cathode, and widely occur in Li-S systems involving liquid electrolytes and polymers due to their high solubility for LiPSs. Studies regarding shuttle effects are reviewed by He and co-workers.⁴⁹ Direct consequences are low CEs, active material loss, and fast capacity decay. GPEs, SPEs, SPE-based hybrid SSEs, and oxide-based hybrid SSE are vulnerable to shuttle effects. Confinement of sulfur in a conductive host (including multi-functional and multi-architectural conductive hosts) can be effective for alleviating the shuttle effects.^{26,67,148,149} These sulfur composite cathodes have been systematically reviewed for liquid electrolyte-based Li-S batteries^{1-3,150} and are readily transferable to relevant SSLSB systems. Therefore, we will focus on more discussed viewpoint of rational SSE design instead of cathode design for alleviating the shuttle effects.

2.1.1 GPE-based systems. GPEs are fabricated by impregnating liquid electrolytes into designated polymer matrixes. GPEs generally show excellent flexibility, good interfacial compatibility with electrodes, and comparably high ionic conductivity as liquid electrolytes. From a broad technical perspective, both carbonate-based and ether-based electrolytes are suitable for GPEs. However, the use of carbonate electrolytes is limited by their irreversible reactions with LiPSs, so only cathodes free of LiPSs intermediates such as small sulfur molecules,^{151,152} polymer-S such as PAN-S^{114,153} and molecular layer deposition (MLD) protected sulfur^{154,155} are compatible with carbonate-based GPEs. For broader applicability, ether-based GPEs, especially those incorporating 1 M LiTFSI in 1,3-dioxolane (DOL)/1,2-dimethoxyethane (DME) (v/v = 1/1) with a LiNO₃ additive, are the most widely used in SSLSBs. In addition to flexibility, ionic conductivity, and interfacial capability, an ideal GPE for SSLSBs should possess strong mechanical properties, electrochemical/thermal stabilities, and LiPS shuttle suppressing capability for high-performance and safe SSLSBs.

A porous poly(vinylidene fluoride) (PVDF) membrane fabricated by a phase inversion method is a promising polymer matrix due to its good mechanical properties, high stability, and high porosity for liquid electrolyte accommodation. However, both the -F on the branch and -CH₂- on the main chain show low binding energies with LiPSs, which cannot capture or confine LiPSs. Considering that oxygen/nitrogen-functional groups (-O-C=O, -C=O, -C-O-C, -C=N, etc.) exhibit strong interactions with LiPSs,¹⁵⁶ oxygen/nitrogen-functional groups containing polymers and metal/non-metal oxides/nitrides are promising for alleviating the LiPS shuttling. Wu *et al.* developed a sandwiched GPE with a poly(methyl methacrylate) (PMMA) middle layer and PVDF outer layers. The PVDF layers provide sufficient space for accommodating ether-based electrolytes and facilitate Li⁺ transport, while the PMMA layer can trap the dissolved LiPSs to improve cycling stability. Benefitting from the effective LiPS confinement and the fast Li⁺ transport, the resultant Li-S batteries delivered a high initial discharge capacity of 1711.8 mA h g⁻¹ and maintained 1145.3 mA h g⁻¹ after 50 cycles at 200 mA g⁻¹.¹⁴⁵ Similarly, Zhao and co-workers

impregnated a pentaerythritol tetraacrylate (PETEA) GPE into a PMMA-based electrospun network. Due to the synergistic effect between the PMMA network and the PETEA-based GPE, the composite GPE exhibited a high ionic conductivity of 1.02×10^{-3} S cm⁻¹ and excellent LiPS immobilization capability. According to the DFT calculation results, both PETEA and PMMA showed high binding energies with Li₂S₈ (-0.79 eV), which were much higher than that of polypropylene (PP)/polyethylene (PE) (-0.16 eV). Using this composite GPE, SSLSBs achieved a high rate capability of 645 mA h g⁻¹ at 3C and maintained excellent capacity retention of 91.9% after 500 cycles.²² Gao and co-workers fabricated a lithiophilic GPE *via* self-polymerizing a thin polydopamine (PDA) layer on the surface of PVDF to stabilize the Li anode and trap LiPSs. As shown in Fig. 4A, the pyrrolic nitrogen in the PDA structure can effectively confine LiPSs by their strong interactions, thus reducing the LiPS shuttling to the anode side. Moreover, the nitrogen functional groups play a key role in facilitating uniform Li nucleation during the stripping/plating process owing to their Lewis acid-base interactions with Li⁺, leading to a smooth anode surface with a stable SEI during long-term cycling. As a result, the SSLSBs assembled with such multi-functional GPEs exhibited excellent electrochemical performance comparable to the liquid electrolyte, which maintained a capacity of 868.8 mA h g⁻¹ with a low capacity decay of 0.14% per cycle within 200 cycles and obtained a capacity of 747.1 mA h g⁻¹ at 2C.¹⁵⁷

Oxygen/nitrogen-functional groups containing metal/non-metal oxides/nitrides such as Al₂O₃,¹⁵⁸ ZrO₂,¹⁵⁹ and g-C₃N₄¹⁶⁰ can be functional fillers to block the LiPS shuttling. Ran *et al.* developed a GPE by reinforcing a poly(vinylidene fluoride-co-hexafluoropropylene) (PVDF-HFP) electrolyte into an electrospun polyimide (PI) membrane coated with nano-Al₂O₃, where the PI membrane acted as a mechanical support and Al₂O₃ adsorbed LiPSs for enhancing the cycling stability. As a result, the Li-S batteries achieved a stable discharge capacity of 820 mA h g⁻¹ over 100 cycles at 0.1C.¹⁵⁸ Even though the GPEs possess high porosity for liquid electrolyte accommodation and exhibit high ionic conductivities of over 10^{-3} S cm⁻¹, the large electrolyte/sulfur (E/S) ratio significantly limits the energy density, especially when sulfur loading of cathodes is low. Gao *et al.* fabricated a dense PVDF/PEO/ZrO₂ (PPZr)-GPE (Fig. 4B) by solution-casting. Despite the relatively low electrolyte uptake of 147.3%, an RT-ionic conductivity of 5.25×10^{-4} S cm⁻¹ was achieved because of the interactions between the Lewis-base center in the PEO chains and the oxygen atoms on the surface of ZrO₂ that enhanced the Li⁺ mobility. Due to the strong interactions between ZrO₂ and LiPSs, as shown in Fig. 4C, the Li-S battery using PPZr-GPE and the rGO/S cathode maintained a capacity of 847.2 mA h g⁻¹ after 500 cycles at 1C and realized stable CEs of around 100% without a LiNO₃ additive. As a reminder, high sulfur loading and low E/S ratio are two important parameters for achieving high energy density for Li-S batteries. Based on the rational design of the PPZr-GPE with low electrolyte uptake, fast electron transport in rGO/S, and LiPS shuttling suppression by ZrO₂, the SSLSB with a high

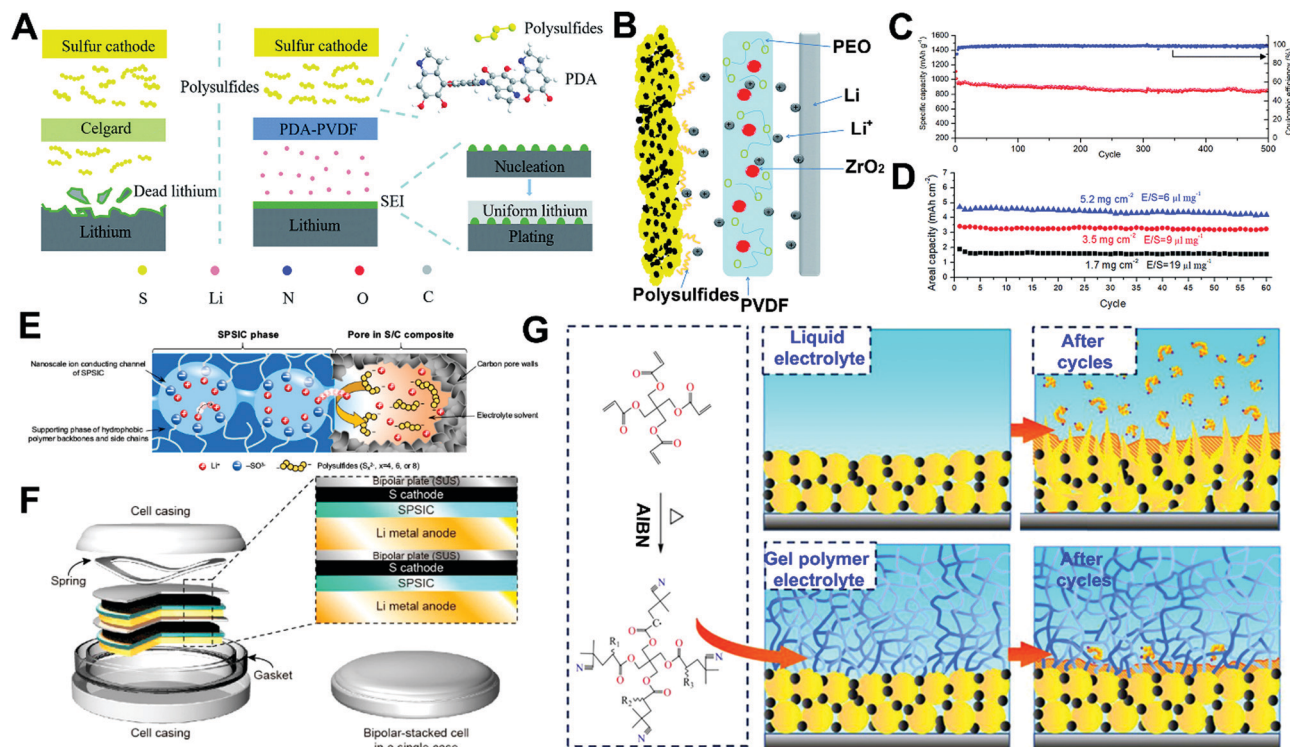


Fig. 4 (A) Schematic illustration of the multiple functions of PDA-PVDF GPE in facilitating uniform Li nucleation and trapping LiPSs, Reprinted with permission from ref. 157, Copyright 2018, Royal Society of Chemistry. (B–D) The illustration of Li^+ transport and LiPSs blocking mechanism for the membrane of PPZr-GPE (B). The long cycle performance of the Li-S battery comprising PPZr-GPE and S@rGO cathode at 1C (C). The cycling performance of Li-S batteries with different sulfur loadings with controllable E/S ratios at a current density of 2.84 mA cm^{-2} (D). Reprinted with permission from ref. 159, Copyright 2017, Royal Society of Chemistry. (E and F) Li^+ transport and LiPS rejection at the interface between the SPSIC and S/C composite (E). Schematic illustration of the bipolar stack type Li-S battery (F). Reprinted with permission from ref. 24, Copyright 2017, American Chemical Society. (G) Polymerization mechanism of the PETEA monomers and the immobilization mechanism for LiPSs by capitalizing on PETEA-based GPE compared with liquid electrolytes. Reprinted with permission from ref. 21, Copyright 2016, Elsevier Ltd.

sulfur loading of 5.2 mg cm^{-2} and a low E/S ratio of $6 \mu\text{L mg}^{-1}$ achieved a high areal capacity of 4.6 mA h cm^{-2} at 2.8 mA cm^{-2} (Fig. 4D).¹⁵⁹ Considering that the heavy metal oxides can lower the gravimetric energy density, an ultra-light $g\text{-C}_3\text{N}_4$ was proposed for GPE preparation. The pyridinic nitrogen group in $g\text{-C}_3\text{N}_4$ can not only confine the LiPSs but also suppress the Li dendrite growth. As a result, the Li- FeS_2 battery can stably run for 400 cycles with a capacity of over 250 mA h g^{-1} at 0.1C.¹⁶⁰

Even though the adsorption strategy can prevent the LiPSs from shuttling to the anode side for high CEs, a large amount of LiPSs are generally immobilized in the electrically insulating GPEs and isolated from subsequent electrochemical reactions. The loss of active material leads to fast capacity decay. The development of a GPE that cannot dissolve LiPSs would be more effective. Single-ion conductive GPEs are promising options, conducting Li^+ but blocking the negatively charged LiPSs. Lithiation of commercial proton exchange membranes is a good strategy for achieving single-ion conductive GPEs. Zhao *et al.* exchanged the protons in the Nafion membrane with Li^+ and obtained a single-ion conducting GPE after activating with a solution of $1.0 \text{ M LiN}(\text{CF}_3\text{SO}_2)_2$ in DOL/DME (1 : 2 w/w). When the Li^+ dissociated from the side chains, the $-\text{SO}_3^-$ groups formed an electrostatic shield that gave passage to the Li^+ but prevented the S_n^{2-} ($3 \leq n \leq 8$) diffusion. Improved cycling

performance was demonstrated.¹⁶¹ A lithiated perfluorinated sulfonic acid (Li-PFSA) polymer and a sulfolane/diglyme mixture were intentionally used for the solvent-swollen polymeric single-ion conductor (SPSIC). The LiPSs were significantly suppressed by the Donnan exclusion principle (Fig. 4E), achieving a high capacity of 720 mA h g^{-1} and a capacity retention of 79% after 100 cycles for the SSLSBs with SPSIC (50% sulfolane/50% diglyme solvent). Interestingly, the bipolar-stack cell (Fig. 4F) showed similar electrochemical performance as the single cell, which showed promise for future pouch cells.²⁴ However, due to the dense structure of commercial fluorinated sulfonic acid membrane with low electrolyte uptake and low dissociation of Li^+ in organic electrolytes, the RT ionic conductivity is relatively low ($\sim 10^{-5} \text{ S cm}^{-1}$). Practical applications with high cathode loading and high-rate performance are hindered. Similarly, lithium trimetaphosphate (LTMP) was synthesized from sodium trimetaphosphate by ion exchange. Using LTMP as a functional additive in the PVDF matrix led to a high ionic conductivity of $2.6 \times 10^{-3} \text{ S cm}^{-1}$ at RT. The LTMP additive can reduce the crystallinity of the polymer membrane and inhibit the LiPS diffusion *via* strong electronegativity, resulting in enhanced ionic conductivity and improved cycling performance.¹⁶² A sp^3 boron-based single-ion-conducting polymer electrolyte film (called PDTAB) was sandwiched between

two carbon films and used together with a Celgard separator as a composite electrolyte for SSLSBs. The uniformly distributed negative charges in the PDTAB electrostatically repulse LiPSs from diffusing into the polymer matrix, which effectively blocked the LiPS shuttling and improved the cycling performance. At a 2C rate, the PDTAB containing SSLSBs maintained a capacity of 1185 mA h g⁻¹ after 100 cycles, which was significantly higher than 688 mA h g⁻¹ of the SSLSB without PDTAB.¹⁶³

Kang and co-workers proposed a different approach trying to stabilize the electrolyte/electrode interfacial passivation layer, so as to alleviate the fast capacity decay due to the volume change during the lithiation/de-lithiation process. A GPE with a high ionic conductivity of 1.13×10^{-2} S cm⁻¹ was synthesized by *in situ* polymerization of PETEA and azodiisobutyronitrile (AIBN) in a liquid electrolyte, which acted as a flexible protective layer covering on the surface of S cathode. As shown in Fig. 4G, in the conventional liquid electrolyte, the passivation layer on the cathode can be easily broken because of the serious volume change during cycling, resulting in the exposure of a fresh sulfur surface in the liquid electrolyte. The exposed active sulfur accelerates the diffusion of LiPSs and further participate in the chemical reactions of reconstructing the passivation layer. The repeating breakdown–reconstruction process leads to gradual thickening of the passivation layer and inevitable active material loss and thus fast capacity decay. Replacing the liquid electrolyte with a PETEA-containing GPE promoted the formation of a flexible and stable passivation layer on the sulfur electrode, which effectively inhibited the polysulfide diffusion and improved the cycling performance. As a result, the SSLSBs assembled with PETEA-containing GPEs retained a discharge capacity of 529.7 mA h g⁻¹ after 400 cycles at 0.5C, corresponding to a capacity retention of 81.9%. In contrast, the SSLSBs assembled with only liquid electrolytes delivered a low discharge capacity of only 70.2 mA h g⁻¹ after 200 cycles.²¹

In summary, obstructing the LiPS diffusion to the anode side *via* chemical absorption and the electrostatic repulsion effect are two common and effective strategies for improving the cycling performance of GPE-based SSLSBs. Incorporating polymers or inorganic fillers with functional groups can trap the LiPSs in the GPE matrix and inhibit their passage to the anode side, thus reducing the corrosion of the Li anode and loss of sulfur active material for stable cycling. A drawback is that the LiPSs anchored by the functional groups become immobile for capacity delivery. The development of single-ion conductive GPEs can be a good alternative. In general, the stronger the electrostatic repulsion force between the GPE and LiPSs, the more the LiPSs restricted in the cathode side for better cycling performance. However, a stronger electrostatic repulsion force is accompanied by a stronger adsorption energy between the GPE and Li⁺, to some extent, reducing the ionic conductivity of GPEs. The balance should be well addressed when designing the single-ion conductive GPEs in the future. Moreover, the SSLSB systems aim to supply power to electric vehicles and portable electronic devices, which require a high energy density. Even though creating GPEs with high porosity and high electrolyte uptake *via* the phase inversion method can

significantly improve the ionic conductivity to 10^{-3} – 10^{-2} S cm⁻¹, comparable to that of the liquid electrolyte, it also reduces the energy density of SSLSBs. Hence, for future development, the E/S ratio should be well-controlled to meet the requirements of high energy density. Additionally, a high-loading electrode is another parameter to ensure high energy density. The wettability of GPEs for thick electrodes and the Li⁺ transporting capability within the thick electrode should be investigated. More importantly, GPE-based SSLSBs contain liquid components that inherit safety concerns, especially for GPEs with high electrolyte uptake.

2.1.2 SPEs and SPE-based hybrid SSE systems. As mentioned above, despite the high ionic conductivity of GPEs, safety concerns related to the organic liquid component remain challenging. Complete removal of the liquid electrolyte in GPEs for dry SPEs is highly important. Among various SPE systems, poly(ethylene oxide) (PEO)-based SPEs with excellent electrochemical stability and good interfacial compatibility with electrodes have attracted wide applications in SSLSBs. However, limited by their low RT ionic conductivity of 10^{-8} – 10^{-7} S cm⁻¹, the PEO-based SSLSBs are mostly operated at an elevated temperature of over 60 °C.^{67–70} At the operating temperature, PEO is in a semi-molten state with fast Li⁺ mobility, resulting in a decent ionic conductivity of above 10^{-4} S cm⁻¹. Nevertheless, similar to the ether-based liquid electrolyte, LiPSs are highly soluble in the PEO matrix, as indicated by the two-plateau discharge curve. Therefore, problems related to the LiPS shuttling effects also challenge the SPE-based SSLSBs.

The correlation between LiPS dissolution and capacity decay was demonstrated by scanning electron microscopy (SEM) and ultraviolet-visible absorption spectroscopy (UV-vis) for SPE-based SSLSBs. As shown in Fig. 5A and B, during the charging/discharging process, a large amount of LiPSs escaped from the cathode side and dissolved into the SPE forming a catholyte. In addition, some LiPSs further diffused to the anode side and produced a sulfur-rich passivation layer on the anode surface. The lost LiPSs in the SPE and sulfur-rich passivation layer were unable to deliver capacity during subsequent cycles. Moreover, the evolution of sulfur species during cycling was performed by *in operando* UV-vis focusing on the SPE. As shown in Fig. 5C, when the shuttle effect became observable (after 90 h), corresponding to curves 12–14, the S₄²⁻ species at 420 nm and the S₆²⁻ species at 480 nm appeared to be anti-correlated, indicating that S₆²⁻ was consumed to form S₄²⁻. When the S₆²⁻ diffused to the anode side under the electric field, the S₆²⁻ anions were partially reduced to the insoluble Li₂S₂/Li₂S as a passivation layer on the anode surface and the rest were reduced to S₄²⁻ continuously driving the consumption of the S₆²⁻.¹⁶⁴ In another study, real-time optical microscopy (OM) imaging was developed to monitor the evolution of electrode/electrolyte interfaces at working state. It was found that the bright-white color of the polymer–ceramic composite electrolyte gradually turns dark-brown, further confirming the existence of the LiPS shuttle and clarifying the reason for the capacity degradation in SPE-based SSLSBs.¹⁶⁵

To alleviate the effect of LiPSs, *in situ* formation of a stable SEI on the Li anode surface by introducing effective electrolyte

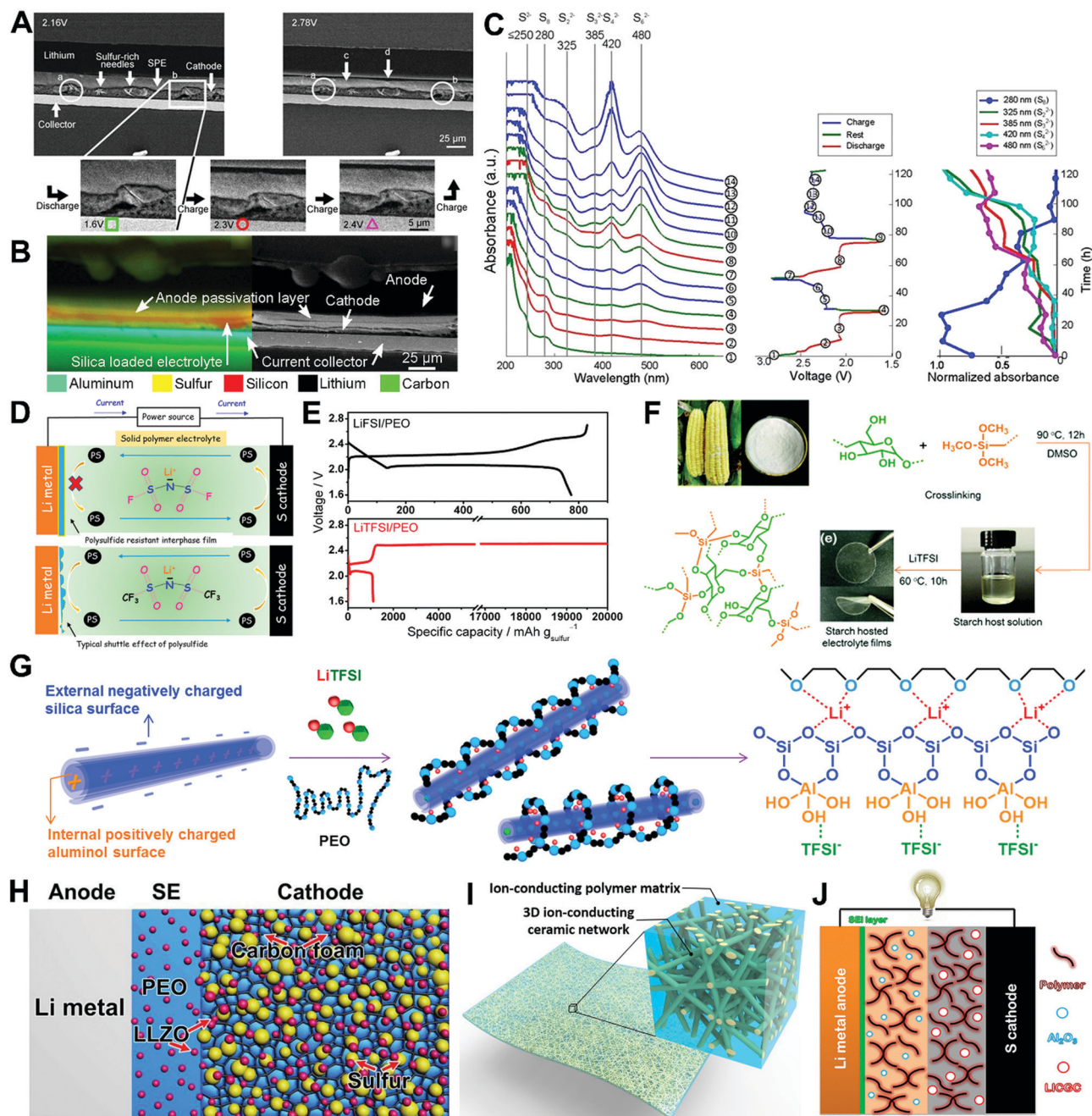


Fig. 5 (A–C) *In operando* SEM images (A) and EDS mappings (B). *In operando* UV-vis results during the charging/discharging process (C). Reprinted with permission from ref. 164, Copyright 2016, Elsevier Ltd. (D and E) Schematic illustration of SPE-based Li-S batteries with LiTFSI and LiFSI as Li salt (D) and corresponding charge/discharge profiles at 0.1C (E). Reprinted with permission from ref. 166, Copyright 2017, American Chemical Society. (F) Preparation of starch hosted SPE. Reprinted with permission from ref. 168, Copyright 2016, Royal Society of Chemistry. (G) Preparation of HNT modified SPE and mechanism of HNT filler for enhanced ionic conductivity. Reprinted with permission from ref. 38, Copyright 2017, Elsevier Ltd. (H) Schematic illustration of an SSLSB based on LLZO nanostructures. Reprinted with permission from ref. 39, Copyright 2017, American Chemical Society. (I) Schematic diagram of 3D LLZO network-reinforced polymer electrolyte. Reprinted with permission from ref. 96, Copyright 2016, National Academy of Sciences. (J) Schematic illustration of an SSLSB with a bilayer electrolyte configuration. Reprinted with permission from ref. 177, Copyright 2017, American Chemical Society.

additives was developed to achieve high CEs and stable cycling performance. As shown in Fig. 5D and E lithium bis(fluorosulfonyl)imide (Li[N(SO₂F)₂], LiFSI) was chosen as the Li salt for SPE preparation. The result showed that the LiFSI helped in the formation of a stable Li anode/electrolyte interface, which is beneficial for alleviating the shuttle effect and leading to high

CEs of around 100% and a high discharge capacity of around 800 mA h g⁻¹. In contrast, overcharging was observed for SSLSBs assembled with LiTFSI salt during the charging process.¹⁶⁶ In another study, LiN₃ was proposed as a promising electrolyte additive. It was found that the LiN₃ can be oxidized into N₂ on the cathode side and then reduced to *in situ* form a

Li₃N layer on the Li anode surface. Even though using LiTFSI as the salt, no overcharging was observed and high CEs of around 100% were achieved. Moreover, the Li-S batteries assembled with the LiN₃ additive delivered a high reversible discharge capacity of approximately 800 mA h g⁻¹ with a capacity retention of around 76% after 30 cycles.²³

Besides the vulnerability to the shuttle effect, the poor mechanical properties and low RT ionic conductivity of SPEs limit the wide application of SPE-based SSLSBs. A cross-linking structure has been widely adopted to effectively decrease the crystallinity of SPEs for improving the ionic conductivity and simultaneously serve as a mechanical support for enhancing mechanical strength. For instance, *in situ* cross-linking the poly(ethylene glycol) diacrylate (PEGDA) and divinylbenzene (DVB) into the PEO matrix reduced the crystallinity of PEO from 34% to 23% and lowered the melting temperature from 50 to 34 °C. As a result, the cross-linked PEO electrolyte with 10% DVB exhibited a high ionic conductivity of over 10⁻⁴ S cm⁻¹ at 70 °C, 2–3 times higher than those of pure PEO electrolytes.¹⁶⁷ In another study, Lin *et al.* developed a novel SPE by cross-linking the -Si-(OCH₃)₃ group on to the molecular structure of starch, as shown in Fig. 5F. Benefitting from the high dielectric constant of the starch host, the as-prepared SPE exhibited a high lithium ion transference number of 0.80 at 25 °C. Moreover, a high RT-ionic conductivity of 3.39 × 10⁻⁴ S cm⁻¹ was achieved, almost two orders of magnitude higher than those of the recently reported PEO electrolytes, enabling successful SSLSB operation at RT. As a result, average discharge capacity values of 864 ± 16 mA h g⁻¹ at 0.1C for 100 cycles and 562 ± 118 mA h g⁻¹ at 0.5C for 1000 cycles were presented.¹⁶⁸

Metal organic frameworks (MOFs) have a high specific surface area well-organized with metallic ions and organic ligands, which can be effective nanofillers for SPEs.^{169,170} MIL53(Al) was developed as a multifunctional filler to improve the ionic conductivity and suppress LiPS shuttling.¹⁷¹ The results showed that the MIL53(Al) fillers can significantly decrease the crystallinity of SPE and result in a high ionic conductivity of 2.41 × 10⁻⁴ S cm⁻¹ at 80 °C, which was 2.6 times the original SPE without fillers (9.24 × 10⁻⁵ S cm⁻¹).¹⁶⁹ Moreover, with the PANI@C/S cathode, the assembled SSLSBs delivered a high discharge capacity of 1520 mA h g⁻¹ at 0.2C and retained a reversible discharge capacity of 558 mA h g⁻¹ and 87% capacity retention over 1000 cycles at 0.5C. The excellent cycling performance of the SSLSBs is attributed to the strong Lewis acid properties, which can absorb abundant anionic groups (TFSI⁻). The MIL-53(Al)-TFSI⁻ can significantly inhibit the LiPS shuttling by electrostatic interactions.¹⁷¹

Besides the cross-linked structure and MOF fillers, inorganic fillers with functional groups show promises in improving the ionic conductivity of SPEs as well as inhibiting LiPS shuttling. Lin *et al.* reported a halloysite (Al₂Si₂O₅(OH)₄) nanotube (HNT) modified SPE and demonstrated to be effective in SSLSBs. The negatively charged outer silica surface and positively charged inner aluminol surface can separately absorb Li⁺ and anions, facilitating Li⁺ transport and suppressing LiPS shuttling (Fig. 5G). As a result, an ionic conductivity of 1.11 × 10⁻⁴ S cm⁻¹ was

achieved at 25 °C. The assembled RT-SSLSBs with a PANI@C/S cathode delivered an initial capacity of 800 mA h g⁻¹ and excellent cycling stability with a capacity retention of 93% within 100 cycles at 0.1C.³⁸ In another study, Tao *et al.* reported the use of highly ionic conductive garnet-type LLZO as a filler to improve the ionic conductivity of SPE. The PEO electrolyte with 15 wt% LLZO fillers achieved the highest ionic conductivity, which was 1.1 × 10⁻⁴ S cm⁻¹ and 1.9 × 10⁻³ S cm⁻¹ at 40 °C and 70 °C, respectively. At a normal human body temperature of 37 °C, the assembled SSLSBs with S@LLZO@C cathode (Fig. 5H) delivered a reversible capacity of around 900 mA h g⁻¹ and high CEs of 100% within 200 cycles at 0.05C.³⁹

Compared with the dispersed nanoparticle fillers, nanofiber fillers and 3D integrated oxide-based SSE scaffolds with fast Li⁺ transport pathways are more promising for highly ionic conductive PSE-based hybrid SSE fabrication.^{96,172–176} Cui and co-workers firstly reported the use of LLTO nanowires to replace the conventional nanoparticles.^{173,174} They found that the Li⁺ can move faster on the surfaces of ceramic nanowires compared with the nanoparticles, resulting in an improved ionic conductivity compared with nanoparticle fillers. The 3 wt% LLTO nanowire modified PAN-LiClO₄ SPE exhibited an ionic conductivity of 5.40 × 10⁻⁶ S cm⁻¹ at 30 °C, which was more than 5 times that of 3 wt% LLTO nanoparticle modified PAN-LiClO₄ SPE (1.02 × 10⁻⁶ S cm⁻¹). Interestingly, they found that the ionic conductivity can be further improved by using well-aligned LLTO nanowires (6.05 × 10⁻⁵ S cm⁻¹ at 30 °C).¹⁷⁴ Fabricating a bi-continuous Li⁺ transport network by infusing the SPE into a 3D ceramic SSE scaffold is another effective strategy to pursue high ionic conductivities. Hu and co-workers proposed a 3D LLZO Li⁺ conductive network *via* electrospinning to improve the mechanical properties and ionic conductivity of PEO-based SPEs, as shown in Fig. 5I. Benefitting from the interconnected Li⁺ transport network in both 3D LLZO and PEO SSE, the hybrid SSE presented a high RT-ionic conductivity of 2.5 × 10⁻⁴ S cm⁻¹.⁹⁶ Later on, a hydrogel-derived LLTO framework and a vertically-aligned LAMP structure were developed as 3D Li⁺ conductive networks, which can improve the ionic conductivities to a level of around 10⁻⁴ S cm⁻¹ at RT.^{175,176} Considering the significantly improved ionic conductivities, the above 3D Li⁺ conductive networks and nanowire fillers show great potential in SSLSBs, especially for near-RT SSLSB application, even though no relative electrochemical performance of SSLSBs was reported in the literature.

The above research studies focused on a single layer of SPE and SPE-based hybrid SSEs for improving the mechanical strength, ionic conductivity as well as suppressing LiPS shuttle. However, in most cases, it is difficult to fabricate an individual SSE with all desired features. Therefore, bilayer and multi-layer SSEs integrating different functions were proposed to synergistically tackle the challenges (Fig. 5J). For example, a bilayer hybrid SSE can consist of a layer of hybrid SSE with inorganic Al₂O₃ fillers and another Li-ion conducting glass-ceramic (LICGC, Li₂O-Al₂O₃-SiO₂-P₂O₅-TiO₂-GeO₂)-containing layer. The former layer helped stabilize the Li/SSE interface, while

the latter layer played an important role in improving the sulfur utilization by suppressing the diffusion of LiPSs into the electrolyte. With the synergistic effect of the two layers, the assembled SSLSBs delivered a capacity of 993 mA h g⁻¹ at the first cycle at 0.05C and CEs higher than 99% after 50 cycles at 70 °C. In contrast, the SSLSBs with a single SSE layer of LICGC experienced a rapid drop in the CEs because of the poor Li/SSE interface; the SSLSBs with a single layer of Al₂O₃ modified SSE delivered very low discharge capacity. Rational designs of multi-layered SSEs can be a good strategy to coherently tackle different challenges for high-performance SSLSBs.¹⁷⁷

In summary, SPEs feature enhanced safety compared with GPEs, because SPEs are free of liquid electrolytes. However, similar to GPEs, the LiPS shuttling problem persists in SPE-based SSLSBs because of the high solubility of LiPSs in the SPE matrix. Meanwhile, the low ionic conductivity at RT limits the wide applications of SPEs. In most cases, the SSLSBs need to be operated at a temperature of over 60 °C. Even higher ionic conductivities to the 10⁻⁴ S cm⁻¹ level at an elevated temperature are still lower than those of GPEs and liquid electrolytes by one or two orders of magnitude, resulting in low discharge capacities and limited operating current densities. The limitation in ionic conductivity is no doubt detrimental to the development of high-energy-density and high-power-density SSLSBs. What is worse, at a high operating temperature, the mobility of LiPSs is enhanced, leading to serious shuttle effects. Overall, the LiPS shuttling problems and the low ionic conductivity SPEs are the two main challenges for the SPE-based SSLSBs. Recently, cross-linked polymers with functional groups and the addition of inorganic fillers were demonstrated to reduce the crystallinity of SPEs and suppress LiPS shuttling. Inorganic conductor fillers like LLZO and LLTO are favorable. Compared to nanoparticle fillers, nanowires and 3D Li⁺ conductive networks with an interconnected Li⁺ transport network can further improve the ionic conductivity to the 10⁻⁴ level at RT. It is meaningful for the development of RT- and near-RT SSLSBs. Developing multi-layered SSEs with each layer having different functionalities is also a good strategy for the development of high-performance SSLSBs. For practical applications, the proportion of the high-density inorganic fillers needs to be controlled. Insufficient fillers show limited improvements in ionic conductivity and LiPS suppression. Overloaded fillers can cause interfacial issues and reduce practical energy density.¹⁷⁸ Developing ultra-thin SPEs and SPE-based hybrid SSEs is urgent for practical energy density, rate capability of SSLSBs, and active material preservation.^{179,180} SPEs and SPE-based hybrid SSEs with low thicknesses, high ionic conductivities (especially at RT and near-RT), and excellent cycling stability are ultimate goals.

2.1.3 Oxide-based hybrid SSE systems. Due to the high solubility of LiPSs in the liquid electrolyte and SPE matrixes, GPEs and SPEs cannot completely avoid the shuttle effects, leading to poor cycling stability. An SSE separator that eliminates the LiPS problems will be a key to achieve excellent cycling stability for SSLSBs. A desired SSE shall either block the

LiPSs from shuttling out of the cathode to the anode or bypass the LiPS formation during charge/discharge (where the cathode possibly undergoes direct conversions between S and Li₂S without soluble intermediates). In this context, oxide- and sulfide-based SSEs are developed for SSLSBs. The sulfide-based SSEs are often used as a single-component SSE in SSLSBs with no LiPSs involved in the charge/discharge process. Their softness and processability are also favorable features. However, the chemical and electrochemical instabilities of sulfides remain the main issues for interfacial compatibility with electrodes. Many ongoing research studies focus on different interface modifications, which will be discussed in detail in the interfacial section of 2.2. For oxide-based SSEs, the large interfacial resistance and rigid properties limit their application as a single-component SSE in SSLSBs. They are usually combined with liquid electrolytes, GPEs, or SPEs to ensure interfacial contacts with electrodes and decrease the interfacial resistance. While the interfacial electrolyte may cause recurrence of the LiPS issue, the oxide SSEs prevent further shuttling of LiPSs.

Xia and co-workers reported a novel dual-phase electrolyte system with LISICON-type LATP as the separator. As shown in Fig. 6A, the LATP SSE enables separation between the catholyte and anolyte, using an ether-based electrolyte for the Li₂S cathode and a carbonate-based electrolyte for the anode. As a superionic conductor, Li⁺ can easily transport through the LATP SSE from the cathode to the anode while the polysulfide-ions are blocked. As a result, side reactions associated with LiPS shuttling were eliminated and the assembled SSLSBs delivered a stable capacity of more than 900 mA h g⁻¹ and CEs of 100% for 150 cycles at 0.05C.⁴⁴ Subsequent applications of LATP and LAGP SSEs as shuttle-alleviating separators are widely adopted for quasi- or semi-SSLSBs.¹⁸¹⁻¹⁸⁴ Interestingly, Gu *et al.* found that the capacity decay of SSLSBs was obstinate when using the same ether-based electrolyte on both cathode and anode sides of the LATP pallet. Therefore, they added 80 wt% of 1,3-(1,1,2,2-tetra-fluoroethoxy)propane (FDE) into the ether-based electrolyte. Benefitting from the low solubility of LiPSs in FDE, the shuttle effect was significantly alleviated and a capacity of 668 mA h g⁻¹ was retained after 1200 cycles at 1C (sulfur loading: 1 mg cm⁻²). Additionally, high capacities of over 1200 mA h g⁻¹ were demonstrated by the 3 mg cm⁻² sulfur-loaded cathode for 5 cycles at 0.1C.¹⁸³

To decrease the ratio of liquid electrolytes in the system, direct evaporation of Li metal onto one side of the LATP SSE pellet is a favorable method to ensure the anode interface (Fig. 6B). The good contact between the Li anode and LATP SSE significantly reduces the interfacial resistance without using a liquid anolyte. The quasi-SSLSBs delivered a high initial discharge capacity of 1510 mA h g⁻¹ which was maintained at 1400 mA h g⁻¹ after 30 cycles at 20 mA g⁻¹.⁴⁰ Nevertheless, the instability of LATP/LAGP with Li metal and LiPSs could still limit their practical application. As shown in Fig. 6C, after soaking a LATP SSE in a Li₂S₆ containing catholyte for 1 day, a permanent color change was observed for the LATP SSE due to the reduction of Ti⁴⁺ to Ti³⁺. As confirmed by XRD (Fig. 6D), a new phase of LiTiOPO₄ appeared. Alternatively, Manthiram

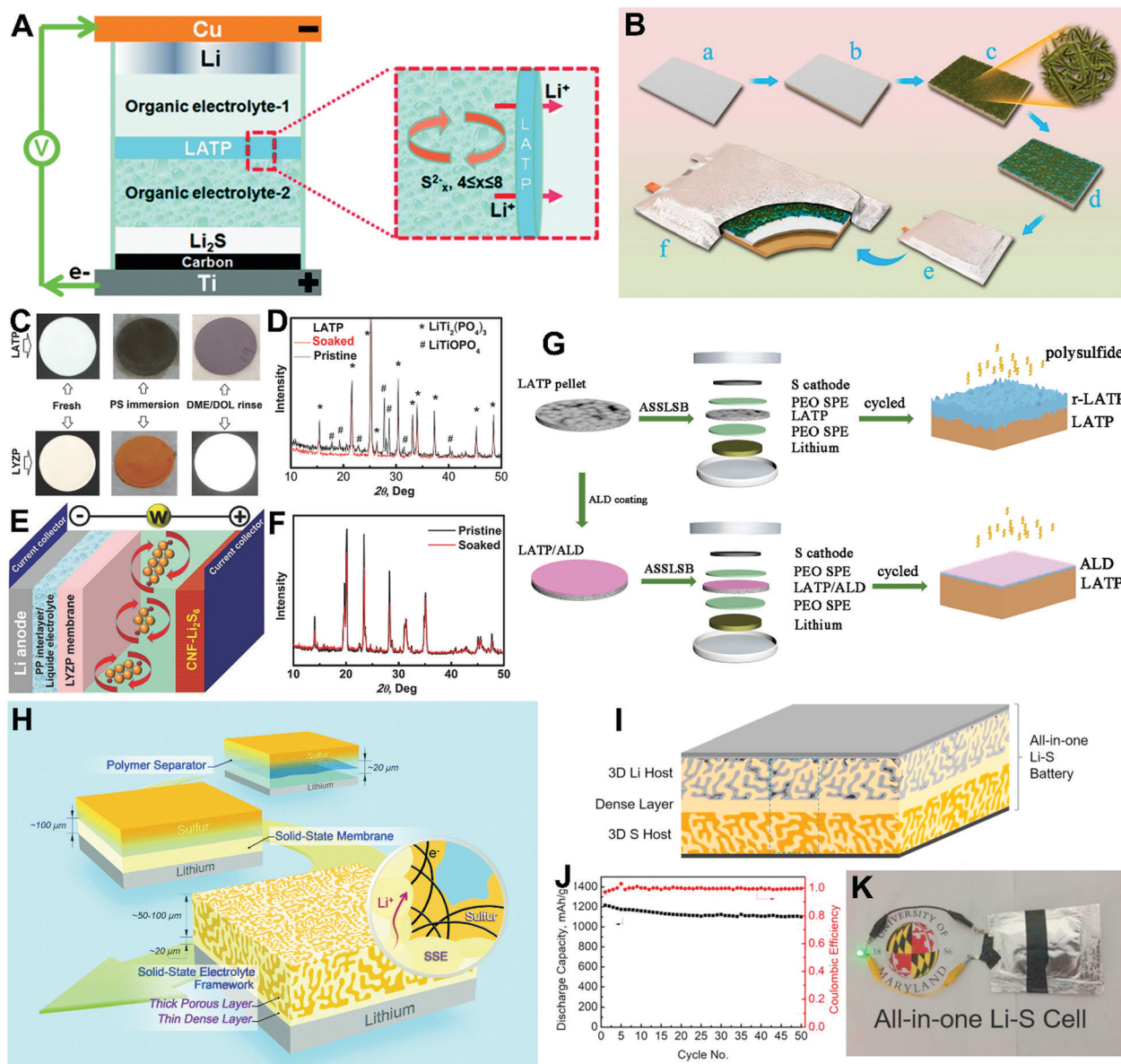


Fig. 6 (A) Schematic of the architecture for the LAMP-based SSLSBs with a dual-phase liquid electrolyte. Reprinted with permission from ref. 44, Copyright 2015, Royal Society of Chemistry. (B) Schematic diagram of LAMP-based SSLSBs with evaporated Li for anode/SSE interface modification. Reprinted with permission from ref. 40, Copyright 2017, American Chemical Society. (C–F) Chemical compatibility tests for the LYZP and LAMP SSEs with the LiPS catholyte (C). Schematic of the architecture of LYZP-based SSLSBs (E). XRD patterns of the LAMP SSE (D) and LYZP SSE before and after being soaked with the 0.25 M Li_2S_6 catholyte (F). Reprinted with permission from ref. 41, Copyright 2016, Wiley-VCH. (G) Schematic diagram showing the preparation of an ALD coated LAMP SSE and the configuration of SSLSBs. Reprinted with permission from ref. 147, Copyright 2018, Royal Society of Chemistry. (H) Schematic of the novel bilayer solid-state electrolyte framework in comparison with traditional soft polymer separators ($\sim 20 \mu\text{m}$) and rigid solid-state membrane architectures ($\sim 100 \mu\text{m}$). Reprinted with permission from ref. 43, Copyright 2017, Royal Society of Chemistry. (I–K) Schematic of the all-in-one SSLSB structure (I). Cycling performance of the all-in-one SSLSBs (J). Optical photo of an all-in-one SSLSB pouch cell (K). Reprinted with permission from ref. 185, Copyright 2018, Elsevier Ltd.

proposed a stable $\text{Li}_{1+x}\text{Y}_x\text{Zr}_{2-x}(\text{PO}_4)_3$ (LYZP) SSE (Fig. 6E) which exhibited excellent stability against Li_2S_6 with no color change or impurity phase formation even after resting the Li_2S_6 catholyte for 7 days (Fig. 6C and F). Benefitting from the high chemical stability of the LYZP SSE and its capability in suppressing LiPS shuttle, the corresponding SSLSBs delivered a stable capacity of around 850 mA h g^{-1} after 150 cycles and high capacity retention of 89.5% at 0.2C.⁴¹

Despite the great progress and excellent RT-electrochemical performance achieved by the quasi- and semi-SSLSBs with liquid electrolyte wetting, the safety concerns are still a big challenge. Using SPEs instead of liquid electrolytes to modify the SSE/electrode interface could be a better option. Our group developed a sandwich-structure hybrid SSE with a middle layer of LAMP SSE and outer layers of PEO SPE (Fig. 6G). To eliminate the side reactions between LAMP SSE and LiPSs, an ultrathin

Al₂O₃ protective layer was coated on the surface of the LATP SSE by atomic layer deposition (ALD). A CE of almost 100% was achieved, which was in sharp contrast to the serious shuttle effect observed for the SSLSBs using only PEO SPE. If only LATP SSE was used, the SSLSBs will experience fast capacity decay due to the active materials loss from side reactions between LATP and LiPSs. A nano-scale Al₂O₃ coating was designed to prevent direct contact between LiPSs and LATP, leading to improved cycling performance. The optimized sandwich-structure hybrid SSE enabled a discharge capacity of 823 mA h g⁻¹ over 100 cycles at 0.1C for SSLSBs.¹⁴⁷ However, minor Ti reduction was still observed in the XPS results. Meanwhile, the low ionic conductivity of the PEO SPE requires a high operating temperature of 60 °C.

In the next step forward, Hu's group developed hybrid bilayer and all-in-all SSLSBs using stable Garnet SSEs (stable against both Li metal and LiPSs).^{43,185} A Li₇La_{2.75}Zr_{1.75}Nb_{0.25}O₁₂ (LLCZNO) bilayer with controlled thicknesses of a 35 μm dense layer and a 70 μm porous layer was fabricated using the tape-casting technique (Fig. 6H). The dense structure was designed to suppress the LiPS shuttling, while the porous structure served to accommodate sulfur and liquid electrolyte infusion. High-temperature sintering at 1100 °C effectively integrates the two layers with small interfacial resistance. As a result, the SSLSBs delivered a capacity of around 600 mA h g⁻¹ as well as a high average CE of 99% with a high sulfur loading of 7 mg cm⁻² at a current density of 0.2 mA cm⁻².⁴³ Nevertheless, the low sulfur utilization (less than 40% of the theoretical value) limits the practical application of high-energy-density SSLSBs. To further decrease the interface resistance between the SSE layers, an all-in-one SSLSB was reported with a porous-dense-porous structure for Li metal host, separator, and sulfur infusion, respectively (Fig. 6I). Impressively, the thickness of the porous matrix and the dense layer can be controlled to as thin as 50 and 15 μm, respectively. The all-in-one structure showed several advantages, including continuous fast pathways for Li⁺ and electrons in the anode/cathode, low local current density by the 3D distribution in the porous structure, locally confined volume changes for avoiding dead Li formation and S isolation, and suitability for cell manufacturing and packaging. As a proof of concept, a high discharge capacity of 1200 mA h g⁻¹ was realized over 50 cycles with a sulfur loading of 5.4 mg cm⁻² and liquid electrolyte usage of less than 1 μL mg⁻¹ S (Fig. 6J). Moreover, a pouch cell was demonstrated from a practical perspective (Fig. 6K).¹⁸⁵

In summary, the dense structure of oxide SSEs shows excellent performance in suppressing the LiPS shuttle and demonstrates improved cycling performance as well as high CEs. However, the oxide SSEs suffer from large electrode/electrolyte interfacial resistance, limiting their application as a single-component SSE for SSLSBs. Modifying the oxide-based SSEs with liquid electrolytes and SPEs is often adopted to reduce the interfacial resistance with electrodes. Nevertheless, the introduction of liquid electrolytes still has inherent safety risks, while the low ionic conductivity of SPEs usually requires high operating temperatures. Further decreasing the amount of liquid electrolyte and developing highly ionic conductive SPEs

for oxide SSE-based SSLSBs are the important directions. Considering the durability of SSEs, LISICON-type SSEs such as LATP and LAGP show poor stability against LiPSs and Li metal, where the Ti⁴⁺ will be reduced to Ti³⁺ during cycling, limiting their direct contact with electrodes. Alternatively, NASICON-type and Garnet-type SSEs show high stability against both Li anode and LiPSs, demonstrating great promise for SSLSBs. Additionally, considering the heavy oxide-based SSEs, the development of ultrathin SSEs is particularly important for high-energy-density SSLSBs. The tape casting technique has been proved to be reliable in fabricating ultrathin SSEs as thin as less than 100 μm.^{185,186} Looking into the future, further development of high-performance SSLSBs with high sulfur loadings and long cycle lives at a reasonable operating temperature is the goal.

2.2 Interface engineering in SSLSBs

Compared to liquid Li-S batteries, the challenges of SSLSBs mainly lie in the interfacial problems from poor solid-solid contact to limited Li⁺ transport at the electrode/electrolyte interface. In the last few years, tremendous efforts have been dedicated to reducing the interfacial resistance, especially for the oxide- and sulfide SSE-based SSLSBs. In Section 2.1.3, we introduce the problem-solving strategies and progress in combination with the suppression of LiPS shuttle effects for oxide SSE-based SSLSBs. In this section, we will focus on the sulfide-based SSLSB system. In the following sections, we will discuss the progress in structural designs for reducing the interfacial resistance of the cathode/electrolyte and the anode/electrolyte interfaces. Physical, chemical, and electrochemical characterizations for the electrode/electrolyte interface will be introduced. In addition to empirical studies, theoretical calculations such as DFT calculations used to help with understanding the interfacial mechanisms will be discussed.

2.2.1 Structural designs for the electrolyte/cathode interface. The cathode layer in SSLSBs usually consists of active materials, binders, Li-ion conductors and electronic conductors. Having multiple components, interfaces within the cathode layer vary from an active materials/Li-ion conductor interface to an active materials/electronic conductor interface. In liquid electrolyte-based Li-S batteries, the flowable liquid electrolytes can easily wet the whole cathode and contribute to low interface resistance. SSLSBs relying on a solid-solid contact experience extra challenges. The large interfacial resistance significantly hinders the electrochemical performance of SSLSBs. In particular, the rate of Li⁺ transport at the SSE/cathode interface is particularly limited. During the charging/discharging cycling, Li⁺/e⁻ pathways could be disconnected due to the volume change of cathode materials. In the following sections, the effects of mixing methods, particle size, and host construction for alleviating the large electrolyte/cathode resistance will be summarized. Moreover, strategies to alleviate the interfacial resistance because of volumetric change during cycling will be discussed.

2.2.1.1 Effect of mixing methods. Sulfide SSEs with high ionic conductivities and good compatibility with sulfur sources are considered as the most promising type of SSEs for SSLSB construction. In the past few years, the mechanical mixing

method has been widely adopted for composite cathode preparation by mixing sulfide-based SSEs with active materials and conductive additives.^{61,64,187–192} Nagao *et al.* found that the electrochemical performance of SSLSBs was significantly dependent on the option of a mechanical mixing method. According to their results, the electrochemical performance of SSLSBs using the composite cathode obtained by ball-milling acetylene black (AB), SSEs and S/Li₂S (labeled as S (or Li₂S)-AB-SE) was superior to that using the cathode prepared by hand grinding the same composition (labeled as S (or Li₂S) + AB + SE).^{61,64} Reversible capacities of 853 and 996 mA h g⁻¹ were achieved at current densities of 1.3 and 0.64 mA cm⁻² after 200 cycles using the S-AB-SE cathode at 25 °C, but the S + AB + SE cathode delivered almost no capacity output. The results were similar using Li₂S as the active material. As shown in Fig. 7C, the SSLSBs with the Li₂S-AB-SE cathode delivered a capacity of around 700 mA h g⁻¹ for 10 cycles, while almost 0 mA h g⁻¹ was delivered using the Li₂S + AB + SE cathode. The high capacities of S-AB-SE and Li₂S-AB-SE cathodes

were mainly attributed to the reduced particle size and homogeneous mixing by ball-milling (Fig. 7A and B), which effectively reduced the electrolyte/cathode interfacial resistance.⁶⁴

The electrochemical reaction is known to occur at the tri-phase interface of active materials, electronic conductors, and Li-ion conductors. During the mixing process, some electronic conductors (or SSE) would be covered with the Li-ion conductive SSE (or electronic conductor) instead of building electronic/ionic conductive pathways for active materials, lowering the capacity output. To avoid the interruption of electronic pathways, a two-step ball-milling strategy is developed. Electronic conductive pathways are built *via* mixing the active materials with conductive additive (Step-I); and then SSEs are introduced for Li-ion conductive pathways (Step-II).¹⁸⁸ Based on this concept, the composite cathode (using sulfur as the active material, vapor grown carbon fiber (VGCF) as the conductive additive, and Li₃PS₄ as the SSE) was prepared by milling durations of 10 and 20 h for Step-I and -II. A high initial discharge capacity of over 1300 mA h g⁻¹ and subsequent capacities higher than 1200 mA h g⁻¹ were delivered over 50 cycles. Moreover, considering that electrochemical performance is highly dependent on the particle size and the uniformity of the cathode components, the size and distributions of the cathode materials with different milling durations were investigated. The results showed that a more homogeneous composite cathode can be obtained upon increasing the milling time, and the capacity increases from around 500 mA h g⁻¹ (Step II: 3 h) to 1333 mA h g⁻¹ (Step II: 20 h) with a constant milling time of 10 h for Step-I.¹⁸⁸

To further decrease the electrolyte/cathode interfacial resistance, a high-temperature-assisted ball-milling method was proposed.^{28,193} As shown in Fig. 7D, at a temperature higher than the melting point of sulfur, the sulfur was melted as a flux. After cooling, the sulfur was precipitated in contact with both SSE and conductive additive. Besides the reduced particle size of sulfur, the introduction of liquid phase enabled effective mixing under moderate milling conditions rather than high-energy ball milling. This helps maintain the intrinsic properties of materials and reduce possible side reactions between the SSE and active materials during high-energy milling.²⁸ Based on the uniform distribution of cathode materials, reduced particle sizes, and decreased interfacial resistance, the resulting cathode showed enhanced electrochemical performance compared to the cathodes prepared by conventional ball-milling at RT. With the sulfur active material, AB conductive additive, Li₂S-P₂S₅ SSE, and Li-In anode, the SSLSBs delivered a capacity of over 1050 mA h g⁻¹ for 50 cycles at a current density of 0.064 mA cm⁻² (milled at 155 °C), which is double the value of its counterpart milled at RT (500 mA h g⁻¹ for 10 cycles). It should be noted that the initial discharge capacities of the two SSLSBs were similar (1087 mA h g⁻¹ for 155 °C milling *vs.* 1180 mA h g⁻¹ for RT milling). The large irreversible capacity of RT milling-based SSLSBs was possibly attributed to the poor contact among the cathode materials that failed to tolerate volume change during cycling. In contrast, the high-temperature milling used the sulfur active material as a binder between the conductive additive and SSE, resulting in high reversible capacity

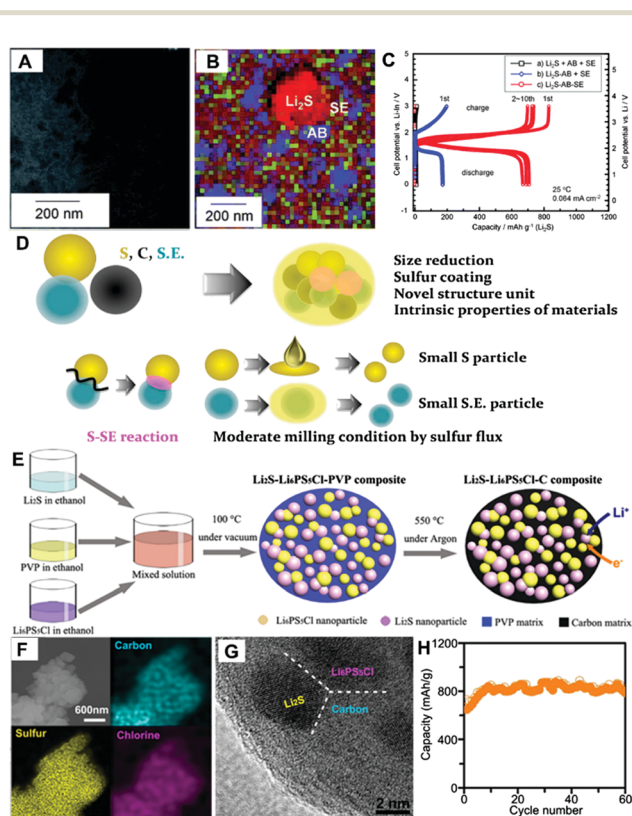


Fig. 7 (A–C) The HAADF-STEM image (A) and corresponding EELS map of the Li₂S-AB-SE composite electrode (B). Charge/discharge profiles of the SSLSBs assembled with Li₂S-AB-SE and Li₂S + AB + SE cathodes (C). Reprinted with permission from ref. 64, Copyright 2012, Royal Society of Chemistry. (D) Schematic of the effects of high-temperature mechanical milling on the structures and electrochemical properties. Reprinted with permission from ref. 28. Copyright 2017, Elsevier Ltd. (E–H) Schematic diagram of Li₂S-Li₆PS₅Cl-C composite cathode fabrication based on a solution process (E). SEM images and elemental mappings of the Li₂S-Li₆PS₅Cl-C composite (F). The high-resolution TEM image of the Li₂S-Li₆PS₅Cl-C composite (G). Cycling performance of SSLSBs assembled with the Li₂S-Li₆PS₅Cl-C composite cathode at 50 mA g⁻¹ (H). Reprinted with permission from ref. 32, Copyright 2016, American Chemical Society.

and excellent cycling stability.²⁸ Similar results were observed for the SSLSBs using 80Li₂S–20P₂S₅ as the SSE, further highlighting the potential application of the high-temperature milling method for SSLSBs.¹⁹³

Since the introduction of liquid phase during ball milling helps reduce the interfacial resistance, fabrication of composite cathodes *via in situ* synthesis of SSEs or recrystallization of SSE/active materials in a solution could be another promising strategy. Eom *et al.* fabricated a Li₂S–VGCF nanocomposite using a liquid-phase approach by dissolving Li₂S in ethanol solvent, enabling the Li₂S nanoparticles with controlled size growth along with the VGCF conductive matrix. Benefiting from the liquid phase, the Li₂S nanoparticles contacted well the SSE and VGCF, which significantly reduced the interfacial resistance and improved the Li⁺/e⁻ transport. As a result, the assembled SSLSBs delivered a high capacity of 600 mA h g⁻¹ and high CEs with 20 cycles.²⁷ In another study, Wang and co-workers developed a composite cathode based on a solution-processable Li₆PS₅Cl SSE (Fig. 7E). As shown in the SEM and high-resolution TEM images in Fig. 7F and G, the Li₂S active material and Li₆PS₅Cl SSE were uniformly confined in a nano-scale carbon matrix, enabling a mechanically robust and mixed ionic/electronic conductive sulfur electrode for SSLSBs. As a result, the assembled SSLSBs with a high Li₂S loading of 3.6 mg cm⁻² exhibited a reversible capacity of 830 mA h g⁻¹ for 60 cycles.³² Besides the Li₆PS₅Cl SSE, Li₇P₃S₁₁ was also reported as an SSE based on the solution method.^{119,194} Xu and co-workers *in situ* grew a thin layer of Li₇P₃S₁₁ SSE on the surface cobalt sulfide by using Li₂S and P₂S₅ as precursors in an acetonitrile solvent. The results showed that the Li₇P₃S₁₁ SSE layer exhibited high ionic conductivity and consisted of nanoparticles with sizes of around 10 nm. Benefitting from the high ionic conductivity and uniform distribution of the Li₇P₃S₁₁ SSE, the assembled SSLSBs exhibited excellent cycling performance for 1000 cycles.¹¹⁹

2.2.1.2 Effect of particle size. Previous discussions briefly gave a hint that the particle size and distribution uniformity have great impacts on the electrochemical performance of SSLSBs. In this section, we will focus on the effect of particle size in detail. Generally, smaller particles have higher surface area for ionic/electronic connection and short diffusion paths within the particle, leading to higher rate performance than bulky materials.¹⁹⁵ Therefore, nano-sized active materials are favorable for SSLSBs. Xu and co-workers proposed to chemically deposit a conformal coating of ~2 nm amorphous sulfur onto reduced graphene oxide (labeled as rGO@S in Fig. 8A). The amorphous rGO@S showed better electrochemical performance compared with a 6 nm crystalline sulfur coating on rGO. For instance, at a C-rate of 0.5C, the SSLSBs with amorphous rGO@S (40 wt% sulfur content) and a double-layer SSE (LGPS/75% Li₂S–24%P₂S₅–1%P₂O₅, Fig. 8B) deliver a high reversible capacity of 1340 mA h g⁻¹ after 30 cycles at 60 °C, which is much higher than that of its counterpart (987 mA h g⁻¹). The higher discharge capacity output can be attributed to the improved Li⁺/e⁻ transport and reduced interfacial resistance

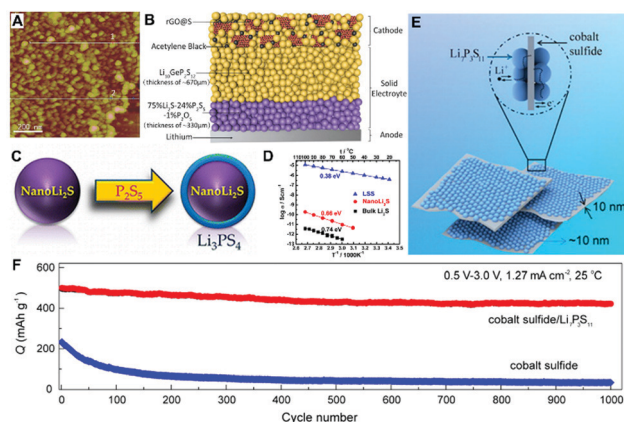


Fig. 8 (A and B) Atomic force microscopy (AFM) image of amorphous rGO@S nanocomposite (A). Schematic diagram of an SSLSB with amorphous rGO@S nanocomposite cathode (B). Reprinted with permission from ref. 31, Copyright 2017, Wiley-VCH. (C and D) Schematic diagram of a lithium superionic sulfide (LSS) nanocomposite preparation (C). Temperature dependency of ionic conductivities of the bulk Li₂S, nano Li₂S, and LSS (D). Reprinted with permission from ref. 58, Copyright 2013, American Chemical Society. (E and F) Schematic diagram of cobalt sulfide–Li₇P₃S₁₁ nanocomposite (E). Cycling stability of SSLSBs assembled with cobalt sulfide–Li₇P₃S₁₁ nanocomposite cathode at a current density of 1.27 mA cm⁻² (F) Reprinted with permission from ref. 119, Copyright 2016, American Chemical Society.

with reduced sulfur coating thickness. Interestingly, they also found that the interfacial resistance of SSLSBs using the amorphous rGO–S cathode was further reduced during cycling due to the improved contact induced by the volume expansion. Despite the slight increase in ionic resistance, the SSLSBs assembled with amorphous rGO@S with a sulfur content of 40 wt% demonstrated stable cycling performance for 750 cycles at 1C with a retained discharge capacity of 830 mA h g⁻¹.³¹ The nano-sized sulfur obtained by the solvent exchange method also demonstrated excellent electrochemical performance with CNTs as a conductive network. The corresponding SSLSBs (sulfur content = 58.55%) delivered a discharge capacity of 1140.9 mA h g⁻¹ at 0.176 mA cm⁻² and maintained a capacity retention of 100% for 400 cycles. Additionally, even after 1000 cycles, the SSLSBs still exhibited a discharge capacity of 834.3 mA h g⁻¹ at 0.44 mA cm⁻².¹⁹⁶

According to Nagao's report, the reaction process and final discharge products were found to be dependent on the particle size. When the Li₂S particle size was less than 10 nm, a reversible and complete conversion process between amorphous sulfur and nanosized Li₂S was achieved, while LiPSs (Li₂S₂ or Li₂S₄) were observed when the particle size was larger than 50 nm. The incomplete conversion reaction resulted in low discharge capacity. In addition, well-dispersed nano-sized Li₂S, SSEs, and conductive additives were necessary to reduce the interfacial resistance and enhance the reversible capacity in SSLSBs.²⁹ To further increase the kinetics of nano Li₂S, a novel Li₂S@Li₃PS₄ core–shell structure was developed as a lithium superionic sulfide (LSS) for enhancing the electrode–electrolyte interface, as shown in Fig. 8C. The LSS cathode exhibited 4 and 6 orders of magnitude improvements compared with the nano

Li_2S and bulk Li_2S , respectively (Fig. 8D). As a result, the SSLSB assembled with the LSS cathode delivered a high discharge capacity of 848 mA h g^{-1} based on Li_2S and high capacity retention of 71% over 100 cycles at 60°C under 0.1C .⁵⁸ Recently, Xu *et al.* *in situ* grew a nano-sized $\text{Li}_7\text{P}_3\text{S}_{11}$ SSE on the Co_9S_8 nanosheets with a thickness of $\sim 10 \text{ nm}$ *via* a solution method (Fig. 8E). Benefitting from the high electronic conductivity of Co_9S_8 , high ionic conductivity of $\text{Li}_7\text{P}_3\text{S}_{11}$ SSE, and reduced cathode/electrolyte interface, the assembled SSLSBs exhibited a reversible discharge capacity of 421 mA h g^{-1} at 1.27 mA cm^{-2} after 1000 cycles (Fig. 8F).¹¹⁹

2.2.1.3 Porous sulfur host. In liquid-based and SPE-based Li–S battery systems, S/C composites with sulfur confined in a porous conductive host have been widely reported as high-performance cathode materials.^{37,197–199} This type of structure possesses several merits. (1) The confinement of sulfur in the

nano-sized or sub-nano-sized pores can significantly facilitate the electronic transport from the conductive host to sulfur; (2) the LiPS intermediates can be confined in the porous structure *via* physical absorption, thus alleviating the shuttle effect and improving the cycling performance; (3) the pre-set volume of the porous structure can buffer the volume changes of sulfur during cycling. However, the use of S/C composites is not often seen in SSLSB systems. Mechanical mixing of conductive carbon, active materials, and SSE is the most popular preparation method for sulfide SSE-based SSLSBs. The reason is that the conductive carbon conducts only electrons but not Li^+ , so the SSLSB would fail to work in short of Li^+ transport channels. Interestingly, a few studies actually demonstrated better SSLSB performance using S/C composites than using cathodes prepared by the popular mechanical mixing method. Sakuda *et al.* impregnated sulfur into a mesoporous carbon matrix (called CNovel) *via* a melt-diffusion process (Fig. 9A). The CNovel possessed a large

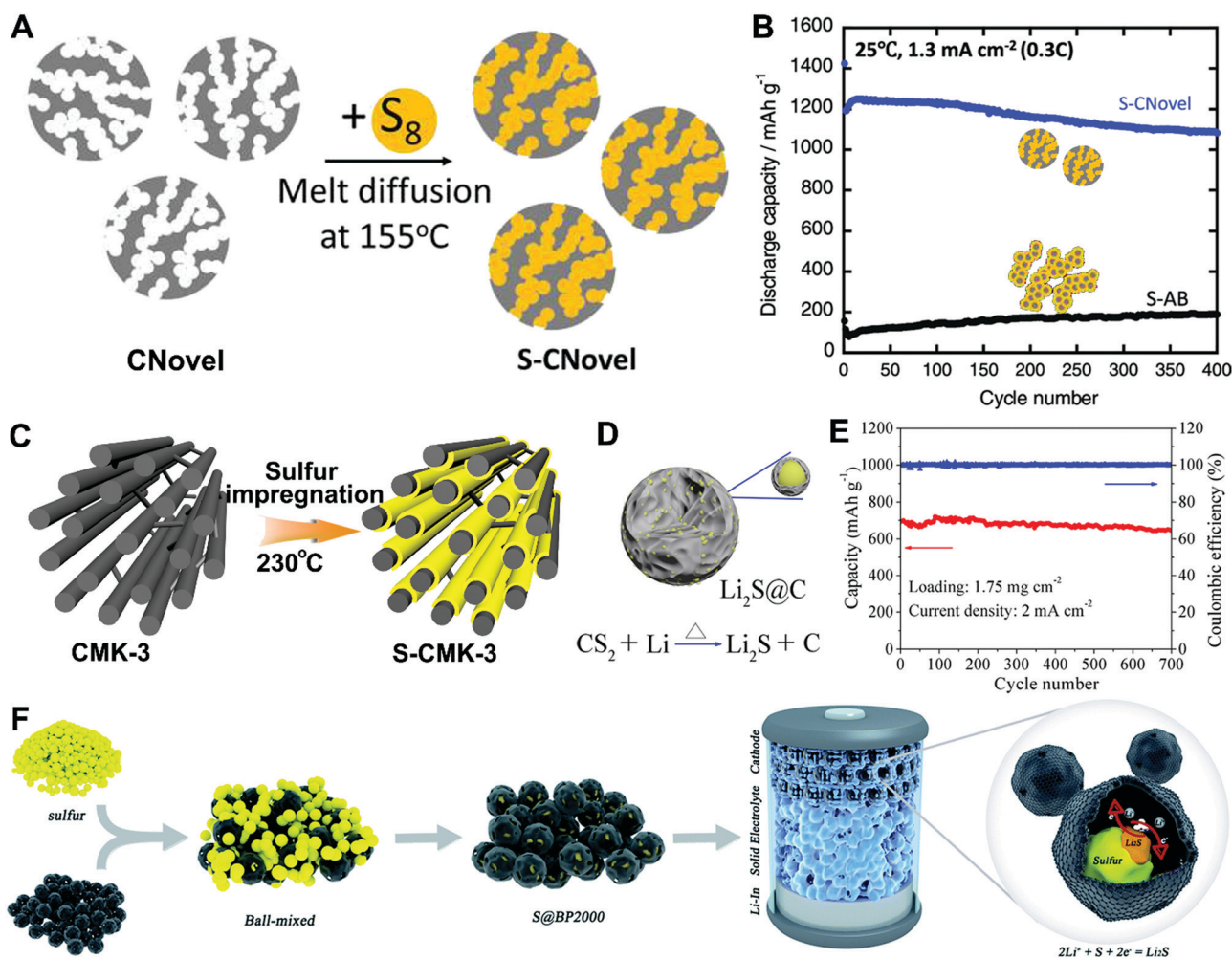


Fig. 9 (A and B) Schematic diagram of S-CNovel composite preparation. (A) Cycling performance of SSLSBs with the S-CNovel and S-AB composites at 1.3 mA cm^{-2} . (B) Reprinted with permission from ref. 200. Copyright 2019, Wiley-VCH. (C) Schematic diagram of S-CMK-3 composite preparation. Reprinted with permission from ref. 201. Copyright 2013, Elsevier Ltd. (D and E) Schematic diagram of the $\text{Li}_2\text{S}@C$ composite generated by the combustion of lithium metal with CS_2 . (D) Cycling stability of SSLSBs assembled with the $\text{Li}_2\text{S}@C$ composite cathode at 2 mA cm^{-2} at 60°C . (E) Reprinted with permission from ref. 202. Copyright 2019, American Chemical Society. (F) Schematic diagram of the prepared S@BP2000 composite and assembled SSLSB. Reprinted with permission from ref. 203. Copyright 2019, Royal Society of Chemistry.

number of “interconnected mesopores” with an average diameter of 5 nm, which provided a large space for sulfur accommodation with interconnected conductive pathways. As shown in Fig. 9B, the SSLSBs assembled with the S-CNovel composite electrode exhibited a high discharge capacity of 1100 mA h g⁻¹ within 400 cycles at a high current density of 1.3 mA cm⁻² at 25 °C. For comparison, a Denka Black carbon (labeled as AB in this work) with a lower pore volume and a lower specific surface area was also chosen as the sulfur host, where the sulfur was coated outside of AB carbon. The assembled SSLSBs present a reversible capacity of only around 200 mA h g⁻¹.²⁰⁰ In another study, as shown in Fig. 9C, an S-CMK-3 composite electrode was obtained by the same melt-diffusion process at 230 °C, where the CMK-3 is also a mesoporous carbon with interconnected pores. With the same sulfur host, the heat-treated S-CMK-3 composite electrode delivered higher discharge capacities and better cycling stability than its counterparts without heat treatment.²⁰¹

Recently, novel structural designs and rational sulfur host selections show promise for further improving the electrochemical performance of SSLSBs. Yang and co-workers developed a Li₂S@C nanocomposite by combustion of Li metal with CS₂, where the Li₂S nanocrystals with particle sizes of 50–100 nm were uniformly embedded in the conductive carbon matrix (Fig. 9D). Benefiting from its unique structure and the interconnected conductive network supplied by the carbon matrix, the SSLSBs assembled with the Li₂S@C composite electrode (Li₂S loading: 1.75 mg cm⁻²) exhibited excellent cycling stability. Capacities of 644 mA h g⁻¹ at 2 mA cm⁻² after 700 cycles at 60 °C and 790 mA h g⁻¹ at 0.5 mA cm⁻² after 100 cycles at RT were demonstrated (Fig. 9E). Moreover, with a high Li₂S loading of 7 mg cm⁻², a high capacity of 1067 mA h g⁻¹ was delivered at 0.2 mA cm⁻² under an operating temperature of 60 °C, corresponding to 91% of Li₂S utilization.²⁰² In a recent study, the micro-pore-rich BP-2000 carbon matrix was chosen as the sulfur host. As shown in Fig. 9F, the S@BP-2000 nanocomposite was obtained by heating the mixture of BP-2000 carbon and sulfur at 155 °C. The BP-2000 carbon delivered a high surface area of 1739 m² g⁻¹ and a pore volume of 2.747 cm³ g⁻¹, which provided a large surface area for sulfur nanoparticle accommodation and facilitated the activity of sulfur nanoparticles and decreased the reaction energy barrier. Moreover, the BP-2000 carbon enabled fast electronic transport and volume expansion accommodation, which significantly reduced the ohmic polarization and enhanced the structural stability of the electrode. As a result, the SSLSB exhibited outstanding specific capacity (1391.3 mA h g⁻¹ at 0.2C), rate performance (678.6 mA h g⁻¹ at 4C) and excellent cycling stability (capacity retention of nearly 100% after 1200 cycles at 3C) at RT. Additionally, upon further increasing the temperature to 80 °C, higher specific capacity (1597.7 mA h g⁻¹, 0.2C) and rate performance (1092.9 mA h g⁻¹, 8C) were achieved.²⁰³ Despite the relatively low sulfur content of around 30 wt% and sulfur loading of around 0.6 mg cm⁻², such excellent electrochemical performance is exciting and comparable to that of liquid Li-S batteries.

The S/C composite with active materials confined in the conductive hosts shows excellent electrochemical performance.

However, the detailed reaction mechanism and Li⁺ transporting pathway shall be further clarified. The requirements of porous carbon host for sulfur need to be further investigated.

2.2.1.4 Alleviation of volume change. The interfacial problems not only affect the electrode materials synthesis and SSLSBs assembly but could also exacerbate during the charging/discharging process. It is known that a serious volume change of 80% occurs between the sulfur and Li₂S during lithiation/de-lithiation. As a result, the active materials can easily detach from the Li⁺ and electronic conductors, causing large interfacial resistance and fast capacity decay. To solve the interfacial issues for stable cycling, external pressure is sometimes applied to ensure good contact within the cathode layer. Actually, before the application for SSLSBs, the concept of external pressure was firstly proposed for the Si anode and Li-ion batteries to solve the contact problem resulting from volume change.^{204–207} Janek's group investigated the internal pressure change during the charging/discharging process using the model cell in Fig. 10A with a pressure sensor. They showed that an elastic stress of around 0.8 MPa was produced during the charging process (LiCoO₂ (LCO) as cathode materials) due to the volume change, which is harmful to the electrochemical performance of solid-state lithium batteries (SSLBs). It should be noted that the volume expansion of LCO is only ~2%, which is 40 times less than that of sulfur.^{205,207} We can imagine the serious challenge of volume changes for SSLSBs. Therefore, it is necessary to solve the volume change issue for high-performance SSLSBs.

In 2016, Li *et al.* demonstrated improved electrochemical performance in terms of both capacity output and cycling stability by externally applied pressure to SSLSBs using a TiS₂ cathode. The unpressed TiS₂/LGPS/In-Li SSLSB experienced gradual capacity decay with increasing overpotential. After 10 cycles, a capacity of only around 120 mA h g⁻¹ was maintained at 1C. In contrast, the SSLSBs with an externally applied pressure of 230 MPa delivered a higher capacity of 168 mA h g⁻¹ from the 2nd cycle to the 10th cycle and no obvious increase in overpotential. Considering the two SSLSBs used the same electrode and electrolyte, the improved electrochemical performance can be attributed to the externally applied pressure that maintained good contact between the active material and SSE during cycling. In another study, with a sulfur/carbon replica (S/CR) composite cathode, LGPS as the SSE, and Li-In alloy as the anode, the assembled SSLSBs exhibited excellent cycling stability under an externally applied pressure of 213 MPa. As shown in Fig. 10B, the SSLSB displayed an extremely high initial discharge capacity of 2000 mA h g⁻¹ and maintained it at 1500 mA h g⁻¹ at 50 cycles at 0.5C. Moreover, stable CEs close to 100% were achieved with a negligible increase in overpotential.²⁰⁸ Recently, our group demonstrated high-performance SeS_x solid-solution cathodes with different Se/S ratios,¹²⁰ where the Se element was introduced for high electronic conductivity and fast electrochemical reaction kinetics.^{63,120,209} Together with an externally applied pressure of 100 MPa, the SSLSBs using a SeS₂ cathode (Se:S = 1/2, Fig. 10C) and Li metal anode demonstrated highly promising electrochemical performance. As shown in

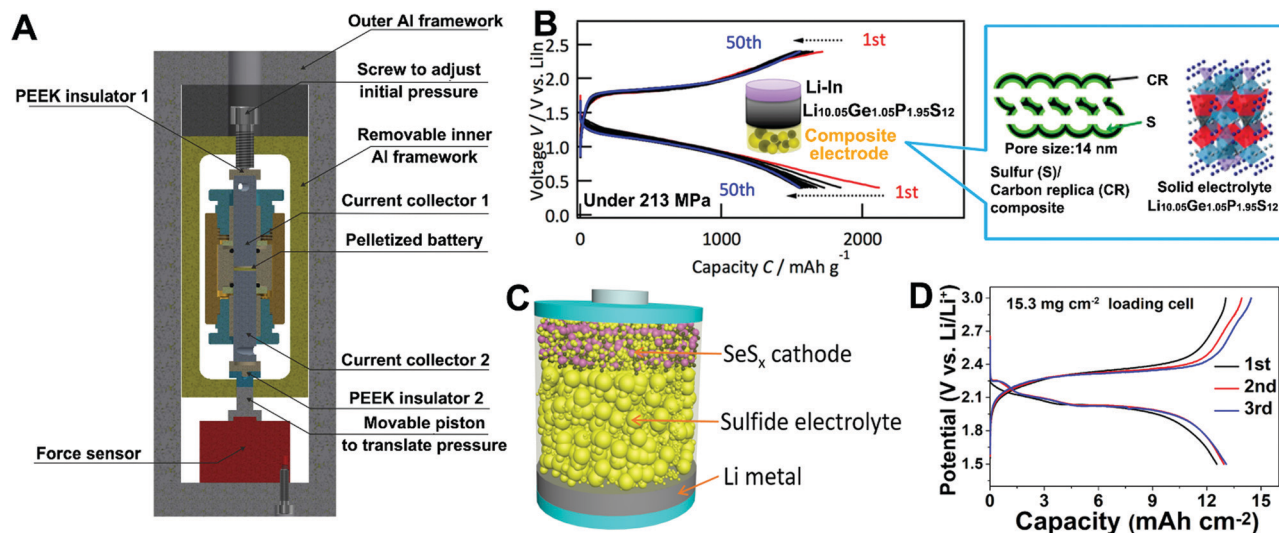


Fig. 10 (A) Schematic diagram of a model cell with a pressure sensor from Janek's group. Reprinted with permission from ref. 207. Copyright 2018, Royal Society of Chemistry. (B) Cycling performance of an S/CR/LGPS/In-Li SSLSB at 0.5C under an externally applied pressure of 213 MPa. Reprinted with permission from ref. 208. Copyright 2018, American Chemical Society. (C and D) Schematic diagram of a Li/Se_x SSLSB (C). Cycling stability of a Li/Se₂ SSLSB with a Se₂ loading of 15.3 mg cm^{-2} at 30 mA g^{-1} under an externally applied pressure of 100 MPa (D). Reprinted with permission from ref. 120. Copyright 2019, Wiley-VCH.

Fig. 10D, the Li/Se₂ SSLSBs assembled with a high loading of 15.3 mg cm^{-2} Se₂ delivered a capacity of 824 mA h g^{-1} at a current density of 30 mA g^{-1} , corresponding to a high areal capacity of 12.6 mA h cm^{-2} .¹²⁰ Even if not highlighted, the externally applied pressure actually played an important role in some reported excellent electrochemical performance.¹¹⁹

The externally applied pressure helps accommodate the volume change during lithiation, contributing to the good contact among the active materials, SSE, and conductive additives, thus improving electrochemical performance in terms of both capacity output and cycling stability. However, for practical cases, it is difficult to maintain such high external pressure for SSLSBs with soft packages unless smart packaging were to be developed. Other strategies that are helpful for alleviating the effect of volume change in pouch cells shall gain more attention. Balancing the volume change between two cathode materials with opposite volume evolution trends could be an effective strategy. Janek's group successfully combined the LCO and $\text{LiNi}_{0.8}\text{Co}_{0.1}\text{Mn}_{0.1}\text{O}_2$ (NCM-811) with less overall volume fluctuation, where NCM-811 exhibited a negative stress response compared with LCO.²⁰⁷ Alternatively, sacrificing partial discharge capacity by controlling a shallow depth of discharge (setting a higher discharge cutoff voltage) can reduce the volume change. Ohno *et al.* demonstrated that SSLSBs with a higher discharge cutoff voltage of 0.4 V (vs. In/Li-In) was beneficial for alleviating the effect of volume expansion. Despite the 20% reduced capacity compared with the SSLSBs with a deep discharge voltage of 0 V, a shallow discharge led to a reversible capacity of 800 mA h g^{-1} over 50 cycles with a capacity retention of ~100%, which showed much better performance than cells that underwent deep charge/discharge (450 mA h g^{-1} with capacity retention of 45% after 50 cycles).²¹⁰ Moreover, as discussed in Section 2.2.1.3, confinement of the

active materials in a porous matrix can reserve space for volume expansion. Alternative cathode materials such as LiPSs or metal/non-metal sulfides with a low volume expansion could be a promising option.

2.2.2 Structural design for the electrolyte/anode interface. In Section 2.2.1, we summarized several strategies to solve the electrolyte/cathode interface. In this section, we will introduce approaches to solve the problem of the electrolyte/anode interface. The interfacial problems between the SSE and anode mainly include poor contact and side reactions. The poor contact between SSEs and anode typically results in large interfacial resistance and Li dendrite growth along the grain boundaries. Side reactions at the SSE/anode interface lead to degradation of the SSE and Li metal and increasing polarization during cycling. The Li dendrite problem will be discussed in detail in Section 2.3.4. In this section, we will focus on introducing the strategies for solving the side reactions occurring at the SSE/anode interface.

In most cases, side reactions involve reduction of high-valence elements (such as Ti^{4+} , Ge^{4+} and Sn^{4+} in LATP, LGP, $\text{Li}_{10}\text{SnP}_2\text{S}_{12}$ (LSPS), LGPS, *etc.*^{50,131,211–213}) in the SSE at low potentials. The rational design of the electrolyte/anode interface is of significance. A straightforward strategy is to prevent direct contact between the SSEs and the anode. ALD and MLD are unique deposition methods that can achieve excellent coverage with precise control of film thickness at the atomic level benefitting from their self-limiting nature.^{214,215} Recently, our group has demonstrated that a 15 nm thick layer of Al_2O_3 coated on the surface of LATP by the ALD technique (abbreviated as ALD@LATP, shown in Fig. 11B) can significantly prevent the side reactions between Li metal and LATP. The Li|ALD@LATP|Li symmetric cell exhibited cycling stability for 600 h at a current density of 0.01 mA cm^{-2} and no increase in polarization.

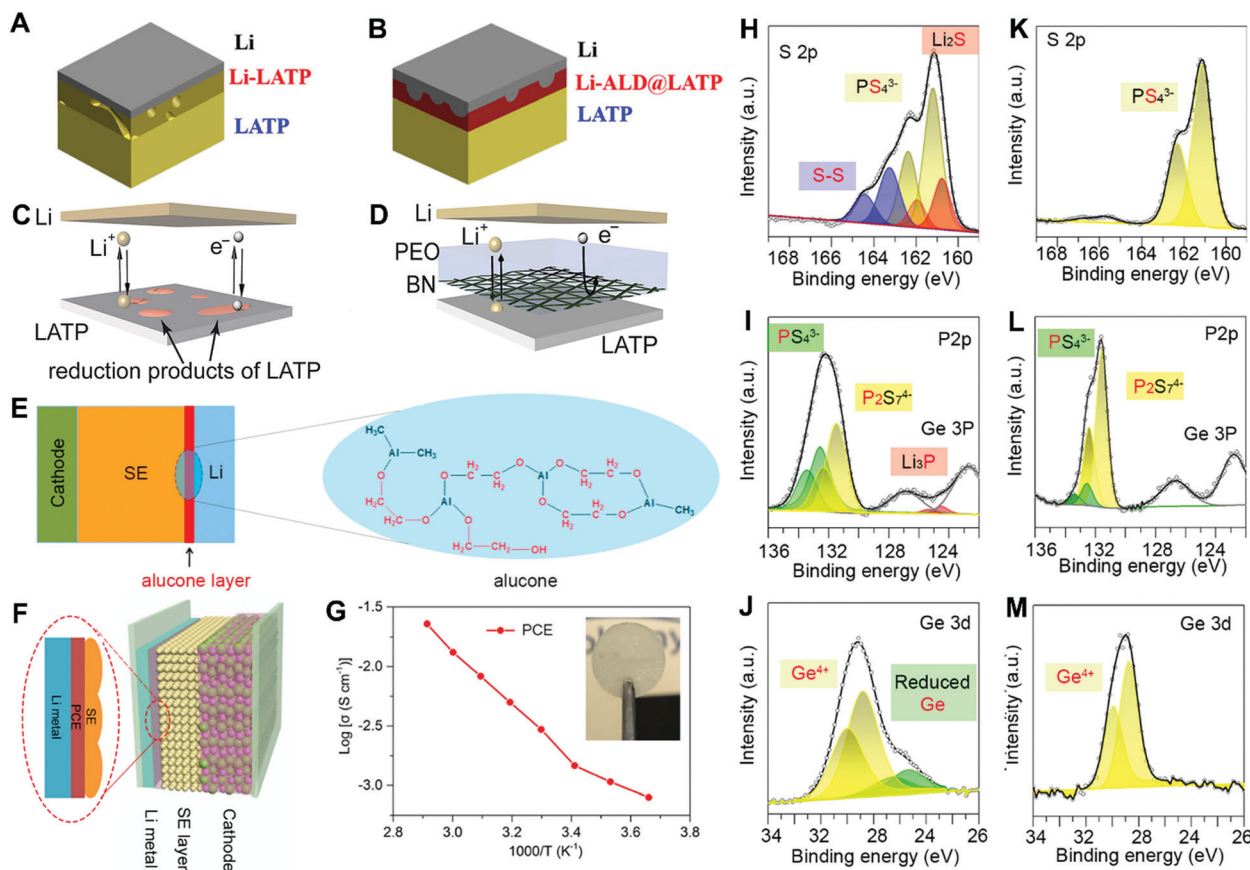


Fig. 11 (A and B) Schematic diagram of Li-LATP (A) and Li-ALD@LATP with an ALD Al_2O_3 coating modified interface (B). Reprinted with permission from ref. 131. Copyright 2018, American Chemical Society. (C and D) Schematic diagram of Li-LATP (C) and Li-LATP with an artificial BN film modified interface (D). Reprinted with permission from ref. 220. Copyright 2019, Cell Press. (E) Schematic diagram of an SSLB with an alucone stabilized Li- $\text{Li}_{10}\text{SnP}_2\text{S}_{12}$ (LSPS) interface. Reprinted with permission from ref. 213. Copyright 2018, Elsevier Ltd. (F–M) Schematic diagram of an SSLB with a PCE protection interlayer (F). The optical image and ionic conductive of the PCE (G). XPS patterns of the LGPS on the Li surface after cycling (H–J) and the LGPS with the PCE interface after cycling (K–M). Reprinted with permission from ref. 221. Copyright 2019, Wiley-VCH.

In contrast, the overpotential increased sharply from 0.1 V to 3.5 V for the Li–Li symmetric cell using unprotected LATP (Fig. 11A). The improved electrochemical performance of the Li–Li symmetric cell with the Al_2O_3 modified SSE/anode interface can be attributed to the reduced side reactions of Ti^{4+} to Ti^{3+} according to the electron energy loss spectroscopy (EELS) results.¹³¹ However, as Al_2O_3 is not a conductor of Li^+ or electrons, a long lithiation process was required in the first few cycles and the operating current density was limited. Li^+ conductors such as SPES are promising protection layers to prevent the side reactions. Zhou *et al.* sandwiched the LATP SSE between two pieces of SPES to inhibit the direct contact between Li and LATP and achieved excellent electrochemical performance.²¹⁶ In another study, Hou *et al.* developed a LiF - and Li_3N -enriched artificial SEI protective layer on the surface of the Li anode to suppress the degradation of LAGP. The assembled Li–Li symmetric cells with LiF - Li_3N -enriched SEI-protected Li anodes and LAGP–PEO hybrid SSEs as electrolytes demonstrated stable cycling performance for nearly 400 h with small polarization at 0.05 mA cm^{-2} at 50°C .²¹⁷

Recently, boron nitride (BN) was reported as an interfacial protection layer to stabilize the Li/LATP interface. Moreover, a

PEO polymer electrolyte with a thickness of 1–2 μm was applied to reduce the interfacial resistance between Li and BN (Fig. 11D). The assembled Li–Li symmetric cell showed stable cycling performance for over 500 h at 0.3 mA cm^{-2} . In contrast, the same configuration with bare LATP (Fig. 11C) became inactive after 81 h. Moreover, with LFP as the cathode material, the assembled Li/LFP SSLBs with the BN protection layer exhibited a high capacity retention of 96.6% after 500 cycles. Besides oxide-based SSEs, some sulfide-based SSEs such as LSPS and LGPS show similar instability against the Li anode. An inorganic–organic interlayer, alucone by MLD, was coated on the surface of the Li anode to stabilize the interface between Li metal and LSPS (Fig. 11E). The alucone coating layer avoided direct contact between Li metal and LSPS and the reduction of Sn^{4+} in LSPS at the Li/LSPS interface was greatly suppressed (confirmed by XPS). Compared with pristine Li, the assembled LCO-based SSLBs with 30 cycles of alucone protected Li exhibited smaller polarization, higher CEs, higher capacity, and longer cycle life. In another study, Zhang *et al.* *in situ* fabricated a LiH_2PO_4 protective layer on the surface of the Li anode by spin-coating 80 wt% H_3PO_4 solution to stabilize the Li/LGPS

interface. With the help of the LiH_2PO_4 protective layer, the Li–Li symmetrical cell demonstrated stable cycling for 950 h at 0.1 mA cm^{-2} with a low polarization voltage of $\pm 0.05 \text{ V}$.²¹⁸ Recently, Wang and co-workers proposed a novel Li/LGPS interface protection method by electrochemically decomposing a liquid electrolyte on the surface of the Li anode. They found that the optimized liquid electrolyte with 1 M LITFSI dissolved in DOL/DME (1:1, v/v) helped to form a salt-based organic–inorganic nanocomposite, consisting of organic elastomeric salts ($\text{LiO}-(\text{CH}_2\text{O})_n\text{-Li}$) and inorganic nanoparticle salts (LiF , $-\text{NSO}_2\text{-Li}$, Li_2O). The organic–inorganic nanocomposite layer showed excellent chemical and electrochemical stability, good affinity with Li and LGPS, and small interfacial resistance, enabling long cycle lives over 3000 h for a Li–Li symmetrical cell (0.1 mA cm^{-2} , 0.1 mA h cm^{-2}) and 200 cycles for a SSLSB with a TiS_2 cathode.²¹⁹

To improve the Li^+ transport capability at the Li/LGPS interface, our group developed solid-state plastic crystal electrolytes (PCEs) as an interlayer between Li and LGPS, as shown in Fig. 11F. The PCE was obtained by infusing succinonitrile (SN) with LITFSI and LiNO_3 into a glass fiber, where the LiNO_3 was used to suppress the side reaction between SN and the Li anode. The PCE delivered a high ionic conductivity of $1.47 \times 10^{-3} \text{ S cm}^{-1}$, enabling fast Li^+ transport through the Li/LGPS interface. More importantly, the PCE interface is beneficial for suppressing the reduction of Ge^{4+} . According to the XPS results shown in Fig. 11H–J, reduction products of Li_2S , Li_3P and reduced Ge were detected at the interlayer-free Li/LGPS interface, indicating the reduction side reaction of LGPS by the Li anode. In contrast, the XPS spectra of S2p, P2p and Ge3d in Fig. 11K–M exhibited the peaks of the same components at the LGPS/PCE interface compared with pristine LGPS, suggesting the strongly suppressed reduction of LGPS. The assembled SSLSBs with a PEC interlayer and PAN-S cathode exhibited stable RT-cycling performance with 800 mA h g^{-1} after 100 cycles at 0.13 mA cm^{-2} . In contrast, the capacity of SSLSBs without PEC protection showed rapid capacity decay to around 100 mA h g^{-1} in a few cycles due to the side reaction at the Li/LGPS interface.²¹³

2.2.3 Characterizations for electrode/electrolyte interfaces.

The interfacial Li^+/e^- transport capability and interfacial stability have great impacts on the electrochemical performance of SSLSBs, presenting in terms of internal resistance, cycling performance, and kinetic response, *etc.*²²² Understanding the interfacial reactions and interfacial kinetics in depth is of significance for guiding the rational design of the electrolyte/electrode interface in SSLSBs. Nevertheless, the buried solid–solid interfaces in the complicated components of SSLSBs are extremely difficult to identify and investigate. The present understanding of the interfacial behaviors is still limited. It is urgent to make smart use of the advanced characterization techniques to gain more insight into the interfacial behaviors for SSLSBs. Time-of-flight secondary ion mass spectrometry (TOF-SIMS), SEM and TEM equipped with energy-dispersive X-ray spectroscopy (EDX) and electron energy loss spectroscopy (EELS) were used to identify the morphology and elemental

composition of the interface materials.^{131,223–225} Morphological and compositional evolution information during cycling could be obtained by characterizing the interface after particular electrochemical conditions or durations. X-ray absorption near-edge spectroscopy (XANES) and XPS have been utilized widely to clarify the interfacial reactions and interfacial stability evaluation.^{130,147,221,226,227} For instance, Meng *et al.*, for the first time, observed the lithium accumulation behavior at the anode/current collector and cathode/electrolyte interfaces with TEM-EELS mapping, which clarified the limited Li^+ transport rate at the interface.²²³ According to Park's TOF-SIMS results, when a mixture of LCO and LLZO was annealed at a high temperature of $700 \text{ }^\circ\text{C}$, a large amount of Al leached out from LLZO and diffused into LCO, resulting in the transformation of the cubic LLZO to the tetragonal phase at the interfaces.²²⁴ Okumura *et al.* developed a depth-resolved XAS (DR-XAS) to directly observe the chemical state and local structure at the LCO–LATP interface. The results exhibited that the introduction of NbO_2 between LATP and LCO can significantly inhibit the large Co–O bond change at the interface during de-lithiation. Thus, decreased activation energy and smoother charge transfer process were achieved due to the relieved interface stress.²²⁷

Based on the space-charge layer (SCL) concept, an ionic conductive buffer layer coating on the cathode surface can help to change the sharp potential drop on the electrolyte/electrode interface. However, it still lacks direct experimental evidence to discern the boundary potential distribution. Liang *et al.* applied atomic force microscopy (AFM) with unique sensitivity and operability to reveal the potential distribution at the cross-section of particles. The results showed that the average potential was decreased by approximately 66 mV by introducing a LATP coating at the cathode surface. The improvement of the interface dynamics was realized by the weakened SCL or a gradient potential formed at the interface, demonstrated by AFM interfacial potential analysis.²²⁸

Recently, nuclear magnetic resonance (NMR), especially lithium-ion exchange NMR, was developed as a powerful tool to study the Li^+ transport at the interface.^{36,229,230} One-dimensional (1D) ^7Li – ^7Li NMR exchange experiment was first applied to probe the Li-ion transport behavior at the interface by using argyrodite $\text{Li}_6\text{PS}_5\text{Cl}$ as the electrolyte and Li_2S as the cathode material. Typically, the $\text{Li}_6\text{PS}_5\text{Cl}$ SSE presented a narrower resonance compared with the Li_2S electrode material, which was a consequence of the Li^+ induced motional narrowing due to the larger mobility of Li^+ in bulk $\text{Li}_6\text{PS}_5\text{Cl}$ SSE. When the $\text{Li}_6\text{PS}_5\text{Cl}$ SSE and Li_2S electrode material were mixed, the Li^+ tended to diffuse from the $\text{Li}_6\text{PS}_5\text{Cl}$ phase toward the Li_2S phase, confirmed by the reduced intensity of the $\text{Li}_6\text{PS}_5\text{Cl}$ NMR signal (Fig. 12A). To quantitatively identify the Li^+ exchange rate, the self-diffusion coefficient was calculated according to Fick's law. It was found that the self-diffusion coefficient for $\text{Li}_6\text{PS}_5\text{Cl}$ – Li_2S exchange was only $1 \times 10^{-11} \text{ cm}^2 \text{ s}^{-1}$, orders of magnitude smaller than the $\text{Li}_6\text{PS}_5\text{Cl}$ bulk diffusion coefficient, proving the limitation of Li^+ transport at the interface.^{36,229} Following up, C. Yu *et al.* developed two-dimensional (2D) ^7Li – ^7Li

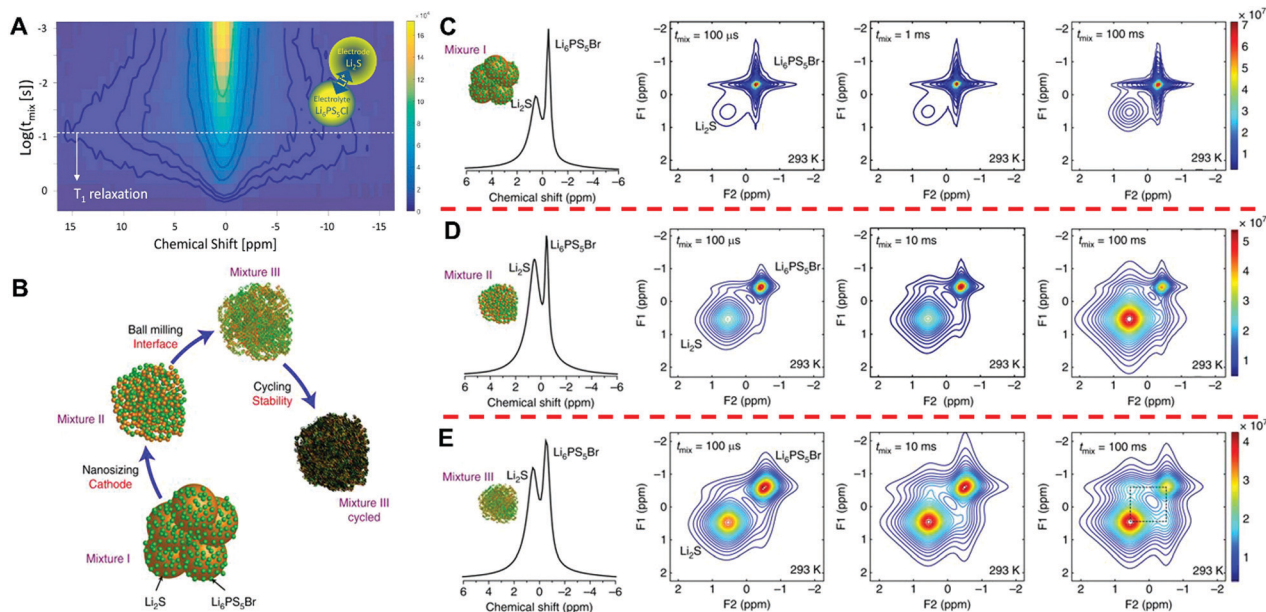


Fig. 12 (A) $1D\ ^7\text{Li}-^7\text{Li}$ NMR exchange experiment probing the Li-ion transport from the electrolyte $\text{Li}_6\text{PS}_5\text{Cl}$ phase to the electrode Li_2S phase. Reprinted with permission from ref. 36. Copyright 2016, American Chemical Society. (B–F) The different stages in cathode preparation with the Li_2S cathode material and $\text{Li}_6\text{PS}_5\text{Br}$ SSE (B). $1D\ ^7\text{Li}$ magic angle spinning (MAS) spectra and $2D\ ^7\text{Li}-^7\text{Li}$ exchange spectra ($2D\text{-EXSY}$) of mixture I (C), mixture II (D) and mixture III (E). Reprinted with permission from ref. 229. Copyright 2017, Nature Publishing Group.

NMR exchange to evaluate the influence of Li^+ transport at the interface for cathodes prepared by different methods. As shown in Fig. 12B, the micro-sized and nano-sized Li_2S mixed with the $\text{Li}_6\text{PS}_5\text{Br}$ SSE were labeled as mixture I and mixture II, respectively. Mixture II after ball milling was named mixture III. The first row of Fig. 12C–E displays the $1D\ ^7\text{Li}$ magic angle spinning (MAS) spectra of mixtures I–III, and relative $2D\ ^7\text{Li}-^7\text{Li}$ exchange spectra ($2D\text{-EXSY}$) with mixing times of $100\ \mu\text{s}$, $10\ \text{ms}$ and $100\ \text{ms}$ (labelled as $t_{\text{mix}} = 100\ \mu\text{s}$, $10\ \text{ms}$ and $100\ \text{ms}$, respectively) are shown in rows 2–4. The results showed that all three mixtures possessed similar $1D\ ^7\text{Li}$ MAS spectra, indicating that Li^+ was maintained well in the bulk materials, either within Li_2S or within $\text{Li}_6\text{PS}_5\text{Br}$. The sharper feature of $\text{Li}_6\text{PS}_5\text{Br}$ was attributed to the large Li^+ mobility in $\text{Li}_6\text{PS}_5\text{Br}$. However, the $2D\text{-EXSY}$ results of the three mixtures were quite different. The off-diagonal intensity is clearly observed at $t_{\text{mix}} = 10\ \text{ms}$ and is strong at $t_{\text{mix}} = 100\ \text{ms}$ for mixture III in Fig. 12E, suggesting that Li^+ diffuses from the $\text{Li}_6\text{PS}_5\text{Br}$ phase to Li_2S phase. In contrast, for both mixture I and mixture II at all t_{mix} ($t_{\text{mix}} = 100\ \mu\text{s}$, $10\ \text{ms}$ and $100\ \text{ms}$), no visible off-diagonal intensity was observed, indicating no obvious Li^+ transport at the $\text{Li}_6\text{PS}_5\text{Br}-\text{Li}_2\text{S}$ interface.²²⁹ The results explained the advantages of ball milling discussed in Section 2.2.1.1 for small interfacial resistance and improved electrochemical performance.

In addition to the *ex situ* characterizations, *in situ* characterizations play a more important role in the understanding of solid–solid interfaces due to their real-time measurements, especially for sensitive materials, such as Li and LiPSs that could change after aging. SSLBs with all solid components are suitable for *in situ* microscopy testing due to the absence of a volatile liquid phase in a high vacuum. TEM and STEM

equipped with EELS are powerful tools to track the structural evolution of the interface during the charging/discharging process.^{231–233} Meng and co-workers further developed *in situ* STEM-EELS equipment with a high spatial resolution based on the *ex situ* equipment to further reveal the Li^+ transport and charge transfer behaviors at the interface of LCO/LiPON (Fig. 13A). An unexpected structurally disordered interfacial layer was discovered without cycling. During cycling, Li tended to accumulate at the interfacial layer and finally evolved to the rock salt CoO along with the formation of $\text{Li}_2\text{O}/\text{Li}_2\text{O}_2$. With the thickness increasing, rapid capacity decay or even cathode degradation occurred. These findings indicated that the increasing interfacial resistance at the LCO/LiPON interface and worsening electrochemical performance mainly attributed to the chemical changes instead of space charge effects.²³² The STEM-EELS technique was also utilized to study the interfacial stability of the Li/LLZO interface. When contacted with Li metal, the LLZO surface was reduced and resulted in the formation of a tetragonal-like LLZO interphase. Interestingly, this interface was very stable and inhibited further interfacial reactions between Li and LLZO. Moreover, the extremely thin interphase of about 5 unit cell thickness exhibited a negligible effect on the ionic conductivity of bulk LLZO. This insight provided a new perspective for designing a stable Li/SSE interface that can directly use a Li metal anode in SSLBs.²³¹

Janek and coworkers used *in situ* XPS to investigate the chemical stability of SSEs (*e.g.* LLTO, LGPS, $\text{Li}_2\text{S}-\text{P}_2\text{S}_5$) against Li metal, by using the internal argon ion gun of the instrument for sputtering a metallic target, as shown in Fig. 13B. During lithiation, reduced Ti species like Ti^{3+} , Ti^{2+} and Ti metal were detected, proving the electrochemical instability of LLTO

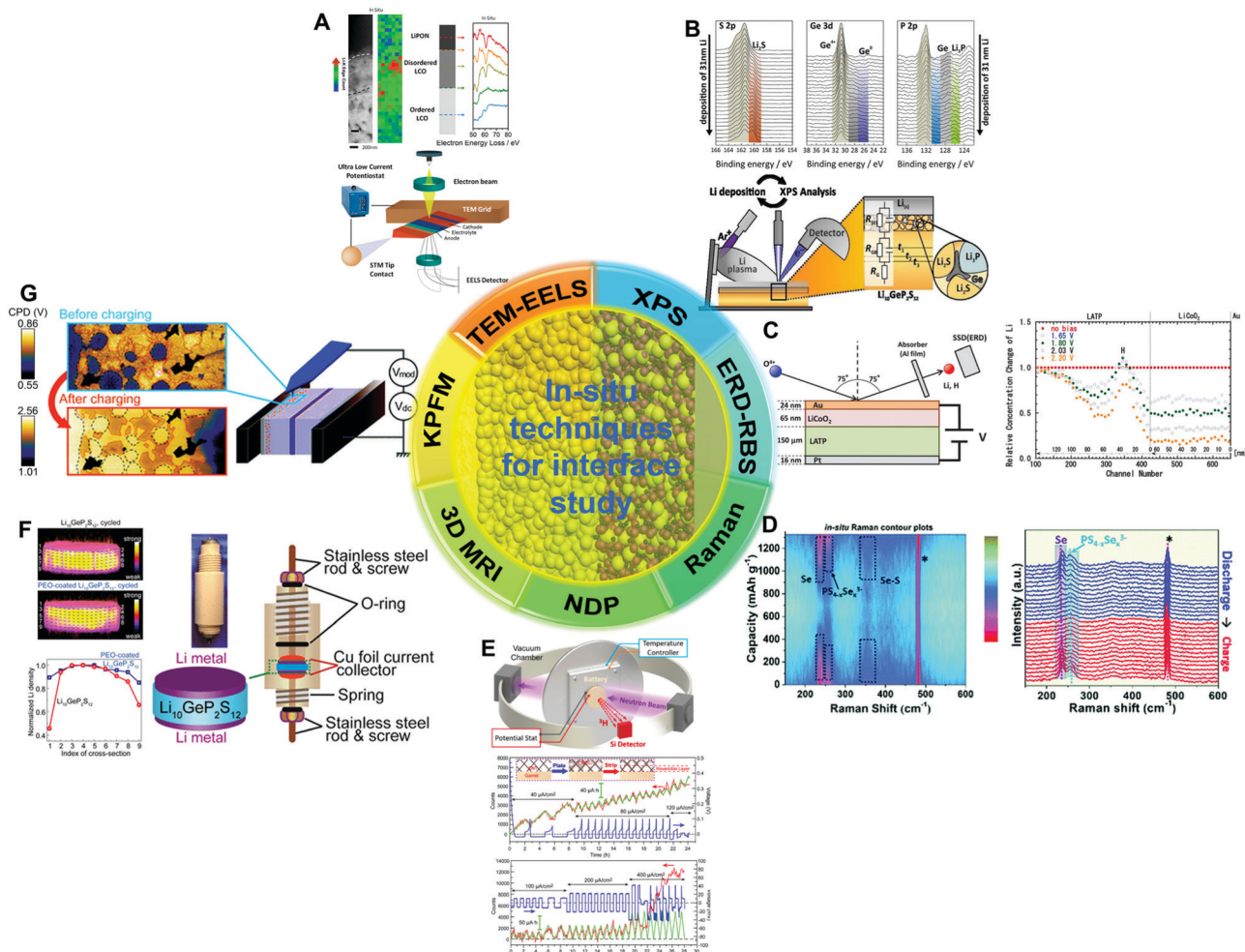


Fig. 13 (A) Schematic of the equipment for STEM-EELS and *in situ* HAADF imaging, elemental mappings and Li K-edge spectroscopy. Reprinted with permission from ref. 232. Copyright 2016, American Chemical Society. (B) Schematic of *in situ* XPS testing and relative XPS recorded during deposition of Li metal on LGPS. Reprinted with permission from ref. 57. Copyright 2016, American Chemical Society. (C) Schematic of *in situ* ERD and RBS analysis of a Pt/LATP/LCO/Au SSLB and relative Li concentration changes at different voltages. Reprinted with permission from ref. 235. Copyright 2019, Wiley-VCH. (D) *In situ* Raman for interfacial reaction studies in solid-state Li-Se batteries. Reprinted with permission from ref. 63. Copyright 2018, Royal Society of Chemistry. (E) Schematic of the NDP system, typical NDP spectra of the Li/garnet/CNT (up) and Li/garnet/Li (down) cells during the plating/stripping process. Reprinted with permission from ref. 239. Copyright 2017, American Chemical Society. (F) Schematic and real cylindrical cell for 3D MRI. ^7Li 3D MRI images and normalized ^7Li densities across horizontal layers at different depths of electrochemically cycled LGPS pellets with and without PEO coating. Reprinted with permission from ref. 240. Copyright 2018, American Chemical Society. (G) Schematic of cross-sectional KPFM and relative CPD images before and after charging. Reprinted with permission from ref. 241 Copyright 2017, Royal Society of Chemistry.

against Li.¹³² Janek's group also investigated the chemical stability of LGPS using the same method. As shown in Fig. 13B, the decomposition products of LGPS such as Li_2S , Ge and Li_3P indicated the instability of LGPS in contact with Li metal.⁵⁷ Similar decomposition products were also detected in the Li_2S - P_2S_5 system by *in situ* XPS. Besides, oxygen contaminations to the Li_2S - P_2S_5 resulted in initial Li_3PO_4 phase segregation and subsequent Li_2O formation. Among these side-products, Li_3PO_4 presented the largest overpotential, indicating significant restriction on Li^+ transport at the Li/Li $_2\text{S}$ - P_2S_5 interface. The formation of side products, especially Li_3PO_4 , leads to irregular Li deposition and deteriorates the battery performance.²³⁴

Very recently, Tsuchiya *et al.* developed *in situ* elastic recoil detection (ERD) and Rutherford backscattering spectrometry (RBS)

to directly analyze the Li distribution near the interface. Fig. 13C presents the schematic cross-sectional and top-view images for the ERD and RBS measurements and the corresponding measured Li distribution at the LCO/LATP and LATP/Pt interface, using a Au/LCO/LATP/Pt SSB configuration. The high-energy O^{4+} probe beam with 9.0 MeV was firstly irradiated at an incident angle of 75° to the SSB surface. With collisions of O^{4+} , recoiled Li^+ and H^+ formed around the Au/LCO/LATP interface and were detected by ERD with a scattering angle of 75° , where the Al film worked as an absorber to eliminate the incident O^{4+} beam and heavier elements so as to detect recoiled Li^+ clearly. At the same time, backscattered O^{4+} by elastic collisions was detected at an angle of 165° to the incident O^{4+} probe beam directions for RBS measurements. Accordingly, the

Li deficient region was formed inside of LAMP around the LCO/LAMP interface and the thickness was determined to be 120 ± 30 nm. The reduction of Li concentration in the LAMP will decrease local Li^+ conductivity around the interface and then increase charge transfer resistance.²³⁵ This work provides another real-time technique for understanding the evolution of the electrode/electrolyte interface.

In situ studies on the cathode/SSE interface are also very informative.^{63,236,237} For instance, Xu *et al.* identified the oxidation of $(\text{Li}_2\text{S})_3\text{-P}_2\text{S}_5$ at the interface with LCO at voltages above 2.1 V (vs. Li_xIn) *via in situ* XPS.²³⁶ Our group used *in situ* Raman to monitor the lithiation/de-lithiation process of solid-state Li-Se batteries. Se was observed to interact with the Li_3PS_4 SSE to form an interfacial species of $\text{PS}_{4-x}\text{Se}_x^{3-}$ during the ball-milling process; the $\text{PS}_{4-x}\text{Se}_x^{3-}$ species were highly reversible during lithiation/de-lithiation that facilitated the kinetics of the solid-state Li-Se batteries (Fig. 13D).⁶³ Coupling XAS with an *in situ* setup revealed the evolution of LGPS during cycling and confirmed the effect of the LiNbO_3 (LNO) protection layer on suppressing the side reactions between LCO and LGPS.²³⁸

In situ neutron depth profiling (NDP), a nondestructive and unique Li-sensitive technique was demonstrated by Wang *et al.* to probe the Li/garnet SSE interfacial behavior during the plating/stripping process. The schematic of the NDP system and relative NDP spectra of Li/garnet/CNT and Li/garnet/Li cells during the plating/stripping process are shown in Fig. 13E. As the plating/stripping proceeded, the counts for Li/garnet/CNT cells increased gradually, suggesting the accumulation of Li in the CNT film, which can be attributed to the formation of “dead lithium” outside of the reversible layer. Short circuits occurred when the current density increased to higher than $120 \mu\text{A cm}^{-2}$. Interestingly, for the Li/garnet/Li symmetric cell, the counts presented no obvious increase during the plating/stripping process in the current density range of $150\text{--}200 \mu\text{A cm}^{-2}$ before the occurrence of a short-circuit at $200 \mu\text{A cm}^{-2}$, indicating higher reversibility. The difference between the two cells was mainly attributed to the conformal contact between Li and garnet SSE. This result further confirmed the importance of the electrode/electrolyte interface to the battery performance.²³⁹ In another study, Wang and co-workers used NDP to clarify the origin of Li dendrite growth at the grain boundary of SSEs such as LLZO and Li_3PS_4 . They found that the high electronic conductivity of SSE is the reason for Li dendrite growth instead of the widely accepted concept of low Li^+ diffusivity at the grain boundary.²⁴²

In 2016, Romanenko and co-workers reported the first quantitative *in situ* ^1H MRI study of operating organic ionic plastic crystal (OIPC)-based SSLBs. Interestingly, they found that the OIPCs could be partially liquefied at the metal interface during discharge within Li^+ transfer into the OIPC matrix. The liquid phase formed at the interface was beneficial for fast Li^+ transport and thus resulted in enhanced battery performance.²⁴³ Very recently, Chien *et al.* employed three-dimensional (3D) ^7Li MRI to evaluate Li distribution homogeneity in LGPS within symmetric Li/LGPS/Li batteries. The schematic and real cylindrical cell is shown in Fig. 13F. The 3D ^7Li MRI images revealed that a large amount of Li was consumed at the electrode–electrolyte

interfaces and thus resulted in heterogeneous Li distribution during cycling. Li deficiency formed at the interface was determined to be the major reason for the continuous increase of interfacial resistance. The situation of significant Li loss at the electrode–electrolyte interfaces could be alleviated *via* convenient interfacial modification with a PEO/LiTFSI SPE.²⁴⁰ This study demonstrated 3D ^7Li MRI as a powerful tool for noninvasively monitoring the Li distribution at the interfaces and in the bulk of SSLBs as well.

In 2017, Masuda *et al.* used *in situ* cross-sectional Kelvin probe force microscopy (KPFM) to directly image the internal electrical potential distribution of SSLBs with a LiCoPO_4 (LCP) cathode, Pd conductive additive, and LAMP SSE. As shown in Fig. 13G, after discharging, all the cathode components exhibited higher contact potential difference (CPD) compared with the state before charging. The CPD values at the active material regions (red dotted line enclosed part) changed from 0.76 V to 2.05 V, which could be attributed to the electrochemical reaction and Li^+ deintercalation from LCP particles. Interestingly, it was found that the CPD values at the LAMP regions (except for the black broken line enclosed part and red dotted line enclosed part) also changed from 0.75 to 2.25 V, indicating depletion of Li^+ in LAMP.²⁴¹ This discovery is very important to understand the evaluation of the distribution of the Li^+ depleted region as well as the analysis of the cause of degradation.

In summary, advanced *ex situ* and *in situ* characterization techniques play very important roles in understanding the structural and chemical evolutions for interfacial stability. These characterization techniques provide a valuable perspective of interface behaviors and could be guidelines for designing more favorable interfaces for SSLBs. Although not all the discussed characterization techniques were demonstrated with the SSLSB system, valuable experience and information can be versatile for SSLBs. Fundamental studies on SSLBs are urgently needed for powerful tools and smart designs. We strongly recommend the wise application of diverse characterization techniques to provide comprehensive evidence and strong support for understanding interfacial behaviors and developing high-performance SSLBs.

2.2.4 DFT studies for electrode/electrolyte interfaces. A deep understanding of the electrode/SSE interfacial properties and interfacial evolution behaviors during the charging/discharging is indispensable to the development of SSLBs. Although valuable interfacial information can be obtained using advanced characterization techniques, the theoretical/intrinsic formation of interfaces, such as the space-charge layer (SCL) and Li^+ transport pathways is very difficult to be identified by experiments at the atomic level. Computational science makes a great contribution toward the elucidation of the interface properties and a deep understanding of the interfacial behaviors in SSLBs.²⁴⁴

Multiple empirical reports showed that the Li_2CO_3 formed on the surface of LLZO is the main reason for the lithiophobic property of LLZO and thus resulted in large Li/LLZO interfacial resistance.^{245–247} This has been widely accepted and many

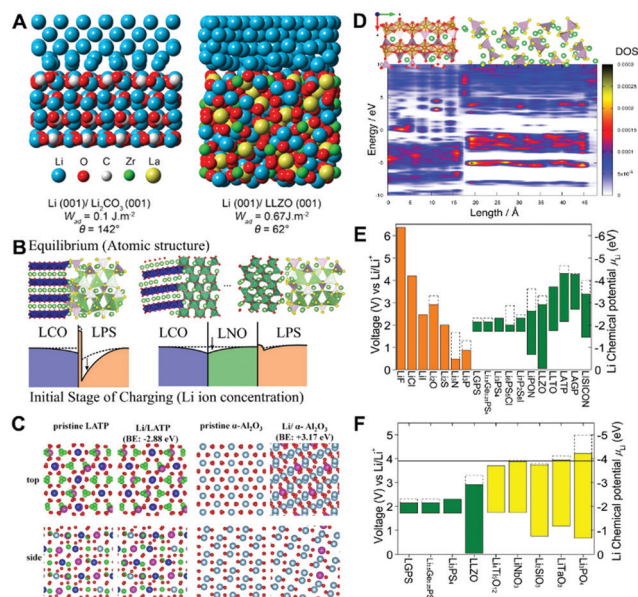


Fig. 14 (A) Calculation of adhesion (W_{ad}), contact angle (θ), and atomic structure for the Li– Li_2CO_3 and Li–LLZO interfaces. Reprinted with permission from ref. 248. Copyright 2017, American Chemical Society. (B) Interface structures of LCO(110)/LPS(010), LCO(110)/LNO(1 $\bar{1}$ 0), and LNO(1 $\bar{1}$ 0)/LPS(010) and relative Li concentration changes at the initial stage of charging for the LCO/LPS interface and LCO/LNO/LPS interfaces. Reprinted with permission from ref. 252. Copyright 2014, American Chemical Society. (C) Top and side views of bulk LATP and α - Al_2O_3 structures with and without extra Li. Calculated binding energy of a single Li into bulk systems is presented by BE. Reprinted with permission from ref. 131. Copyright 2018, American Chemical Society. (D) Contour map of the density of states (DOS) for beta spin electrons of the LFP(010)/ Li_3PS_4 interface for the average structure. Reprinted with permission from ref. 253. Copyright 2016, American Chemical Society. (E and F) Electrochemical stability window of SSE and Li-containing components (E). Electrochemical stability window of commonly used coating layer materials and SSEs (F). Reprinted with permission from ref. 50. Copyright 2015, American Chemical Society.

strategies such as mechanical polishing, high-temperature thermal treatment, and acid treatments are developed to remove the Li_2CO_3 layer to improve Li wettability and get good interface. However, the working mechanism remained unclear until Sharafi *et al.* used DFT calculations to reveal the underlying science. As shown in Fig. 14A, Li exhibited a higher adhesion (W_{ad}) of 0.67 J m^{-2} with LLZO, seven times larger than W_{ad} of Li– Li_2CO_3 (0.10 J m^{-2}), where W_{ad} was determined by the equation of $W_{ad} = E_{\text{int}} - E_{\text{Li-slab}} - E_{\text{LLZO-slab}}$. E_{int} , $E_{\text{Li-slab}}$ and $E_{\text{LLZO-slab}}$ represent the energy of the interface cell, an isolated Li, and LLZO slab, respectively. The larger W_{ad} value can explain why the contact angle decreased considerably after removing the Li_2CO_3 layer on the surface of LLZO (experimental values: 95° vs. 142° , simulation values: 62° vs. 142°). The smaller value predicted between the experimental value and the simulation one was attributed to approximately 15% of carbonate or hydroxide remaining on the surface of LLZO. Generally speaking, the calculation results were consistent with the experiments and clarified the effect of the Li_2CO_3 layer.²⁴⁸

SCL formation has been widely regarded as one of the possible mechanisms that lead to a large interfacial resistance.^{249–251}

Local Li^+ concentration is deficient in the SCL, thus leading to decreased ionic conductivity and limitation of Li^+ transport crossing the interface. It has been suggested by the evidence of potential gradient at the initial stage of charging in the voltage profiles. However, due to the challenges of observation of complicated interfacial Li^+ distribution at the atomic scale, the direct probing of SCL is very difficult. Tateyama and co-workers investigated the SCL and the effect of the buffer layer using the LCO– Li_3PS_4 (LPS) and LCO–LNO– Li_3PS_4 systems (Fig. 14B). At the LCO–LPS interface, the Li-vacancy formation energies (E_v) were in the range from 1.5 to 4.0 eV, which forced Li^+ to escape from the interface into the bulk LPS with a release of the electron to the cathode, thus leading to the enhancement of SCL in the LPS side. With the introduction of the LNO buffer layer, Li^+ at the LP2 site in LPS showed a smaller chemical potential of 0.8 eV than the Li^+ at the LN3 in LNO. Nevertheless, the difference was much smaller compared with LCO/LPS interfaces, thus attributing to the suppression of SCL growth and smooth Li transport paths at the interface.²⁵²

Theoretical computations are also used to understand interfacial reactions. As we discussed in Section 2.2.2, LATP is unstable when in contact with the Li anode due to the reduction of Ti^{4+} in LATP, while a thin Al_2O_3 coating at the interface can significantly suppress the side reactions between LATP and Li metal. The reaction mechanism was here clarified by DFT calculations. As shown in Fig. 14C, upon placing a single Li atom inside of LATP and Al_2O_3 , the behaviors were very different. The absorption energy in LATP was a high negative value of -2.88 eV , confirming the instability of LATP against Li metal. In contrast, the absorption energy in Al_2O_3 was a large positive value of $+3.17 \text{ eV}$, indicating the high stability of Al_2O_3 with Li metal.¹³¹ In another study, Xu *et al.* investigated the effects of LiF and LiI in stabilizing the Li/ $\text{Li}_7\text{P}_3\text{S}_{11}$ interface. The Li/ $\text{Li}_7\text{P}_3\text{S}_{11}$ interface presented a high negative interface energy of $-88.92 \text{ meV \AA}^{-2}$, proving the instability between Li and $\text{Li}_7\text{P}_3\text{S}_{11}$ SSE. In contrast, both the LiF and LiI exhibited positive interface energy towards Li metal, suggesting the enhancement of interfacial stability with the introduction of LiF and LiI layers. Moreover, the interfacial energy of the Li/LiF interface ($73.28 \text{ meV \AA}^{-2}$) was much higher than that of the Li/LiI interface ($36.67 \text{ meV \AA}^{-2}$), which enhanced the Li diffusion along with the Li/LiF interface, promoting a uniform Li deposition resulting in a dendrite-free Li anode.²⁵⁴ A similar result was also obtained by density functional molecular dynamics simulations (DF-MD) of the LFP/ Li_3PS_4 interface in both discharged and charged states. The results showed that both Li^+ and e^- transferred from Li_3PS_4 to LFP during charging, which resulted in the reduction of Fe^{3+} near the interface to localized Fe^{2+} . Simultaneously, the PS_4 anions in the Li_3PS_4 region were oxidized into holes. When 8 Li^+ deliberately migrated to the FePO_4 side, as shown in Fig. 14D, the total energy of the system was reduced by 5.2 eV on the basis of no Li migration system. Subsequently, more localized Fe^{2+} and hole states appeared, respectively, in the bandgap of the FePO_4 and Li_3PS_4 sides. As a result, a Li-depleted layer is formed on the Li_3PS_4 side near the interface. This simulation

result coincided well with the results obtained from the ERD-RBS and KPFM characterization techniques we discussed in Section 2.2.3. This method has also been used in the interfacial research in other SSE/electrode systems such as $\text{Li}_3\text{PO}_4/\text{LFP}$ ²⁵⁵ and LLZO/LCO .²⁵⁶ The DF-MD calculation provides another powerful tool to investigate the interfacial stability between SSEs and electrodes.

Many SSEs, such as LATP and LGPS, show poor stability in contact with the electrodes or exhibit high instability during the charging/discharging process. The identification of suitable interface materials to stabilize the electrode/SSE interface is of significance. Experimental screening through a large number of materials is way too time-consuming and labor-intensive. DFT calculation is also powerful for screening possible interfacial materials with high throughput. According to Mo and co-workers' calculations, most of the sulfide-based SSEs such as LGPS, $\text{Li}_7\text{P}_3\text{S}_{11}$, Li_3PS_4 , $\text{Li}_7\text{P}_2\text{S}_8\text{I}$ and $\text{Li}_6\text{PS}_5\text{Cl}$ will be reduced by Li metal and form Li_2S , Li_3P , Li-Ge alloy, LiCl , LiI , *etc.* The decomposition products showed high stability on the surface of the Li anode and acted as a passivated layer to stabilize the interface. In this regard, Mo *et al.* further calculated the electrochemical stability windows of those decomposition products, as shown in Fig. 14E. All the Li-containing decomposition products exhibited wide stability windows against Li metal. In other words, these materials can be designed as anode/SSE interface materials to stabilize the interface. In addition, the chemical stability of some commonly used cathode coating materials such as LNO, Li_3PO_3 , LiTaO_3 , Li_2SiO_3 and $\text{Li}_4\text{Ta}_5\text{O}_{12}$ was also calculated. The results coincided well with the experimental results that these materials possessed an electrochemical window from the reduction potential of 0.7–1.7 V to the oxidation potential of 3.7–4.2 V (Fig. 14F). Overall, these materials generally have a wide stability window roughly between 2–4 V. Combining the anode/SSE interfacial materials (*e.g.* LiF , LiI , Li_3P) and the cathode/SSE interfacial materials (*e.g.* LNO, Li_3PO_3 , LiTaO_3) can extend the electrochemical stability windows of sulfide-based SSEs from 2–2.3 V to 0–4 V, which is suitable for SSLBs and SSSLBs.

2.3 Recent progress in suppressing Li dendrite

In general, an ideal SSE should possess high ionic conductivity for facilitating Li^+ transport, density and stability to inhibit LiPS shuttling (for solid-liquid dual-phase reaction systems), and good compatibility with the Li metal anode without Li dendrite growth. Unfortunately, the Li dendrite issue in SSSLBs is currently even more serious than in the liquid electrolyte-based batteries. The lower ionic conductivity of SSEs and the absence of LiPS s lead to severe Li dendrite growth in SSSLBs, especially at high current densities and high areal capacities. SPEs and oxide- and sulfide-based SSEs have their own different causes of Li dendrite growth. For the SPEs, low ionic conductivities and poor mechanical properties are the main issues.^{54,66} Under high current densities, the overpotential increased sharply and varied charge distribution and fast Li dendrite growth. Li dendrites easily penetrate the soft SPEs and short circuit the cell. In ceramic-based SSSLB systems, the poor Li^+ diffusion at the grain boundary and high electronic

conductivity of SSEs have been accepted to be the reasons forcing Li dendrite growth along the grain boundary, leading to the occurrence of short-circuit.^{242,257} Additionally, some SSEs such as LATP and LGPS are unstable with respect to Li metal, which leads to continuous decomposition of SSEs and increasing interfacial resistance. In this regard, to pave the way for the practical application of SSSLBs, it is necessary to protect the Li anode to address both Li dendrite growth and interfacial side reactions.²⁵⁸ In this section, we review the strategies of lithium protection against Li dendrite growth. According to the protection mechanisms, these strategies can be classified into four parts: mechanical reinforcement, protection layer, 3D lithium, and interfacial modification.

2.3.1 Mechanical reinforcement. In the SPE systems, poor mechanical strength is the main reason for the short cycling life due to Li dendrite growth. The strategies to enhance the mechanical properties of SPEs have been widely applied to solve the Li dendrite problems. Adding inorganic fillers and crosslinking high strength polymers within the matrix of PEO are popular approaches. Metal/non-metal oxides (*e.g.* SiO_2 , Al_2O_3 , TiO_2) and ceramic SSEs (*e.g.* LATP, LLZO) are used as SPE fillers to enhance the mechanical properties.^{88,93,259–263} For instance, Zhang's group introduced LLZTO having an ultra-high shear modulus of 55 GPa into the PEO-LiTFSI SSE (labeled as PLL composite electrolyte in Fig. 15A). The LLZTO fillers were beneficial for mechanical strength enhancement and uniform Li^+ distribution, thus resulting in a dendrite-free lithium deposition process and enhanced cycling life of the Li-Li symmetric cells (400 h at 0.1 mA cm^{-2}).⁹³ Recent works showed that the capability to suppress Li dendrite with inorganic fillers is related to particle size, concentration, and structure of fillers.^{178,264} Huo's work demonstrated that the large particle size (5 μm) of LLZO exhibited stronger Li dendrite suppression capability compared with the smaller size particles (200 nm). With the same volumetric ratio of 20 vol% (known as the "ceramic in polymer" structure, abbreviated as CIP), the Li-Li symmetric cell assembled with CIP-5 μm can stably cycle for 183 h, while a short circuit occurred in the cell using the CIP-200 nm after 130 h (current density of 0.2 mA cm^{-2} and operating temperature at 55°C). Moreover, the cycle life can be further increased to over 600 h after increasing the 5 μm LLZO ratio to 80 vol%, known as the "polymer in ceramic" structure (labeled as PIC). The improved capability of the PIC structure was also consistent with Chen's work. A long cycling life of 680 h was achieved by the PEO-LLZTO-PEG-60 wt% LiTFSI SSE at a current density of 0.5 mA cm^{-2} , where the LLZO ratio in PEO-LLZTO-PEG was controlled as 85 wt% and the operating temperature was 55°C .²⁶⁴ However, the PIC-5 μm exhibited large interfacial resistance with a Li anode, which should be combined with PIC to modify the interface in practical applications.¹⁷⁸

The construction of integrated 3D scaffolds for polymer electrolyte infusion has been proved to be effective in further improving both the mechanical properties and ionic conductivity compared with particle fillers.^{96,176,262,263} Cui co-workers developed an interconnected SiO_2 aerogel as a strong backbone for strengthening composites and offering large continuous

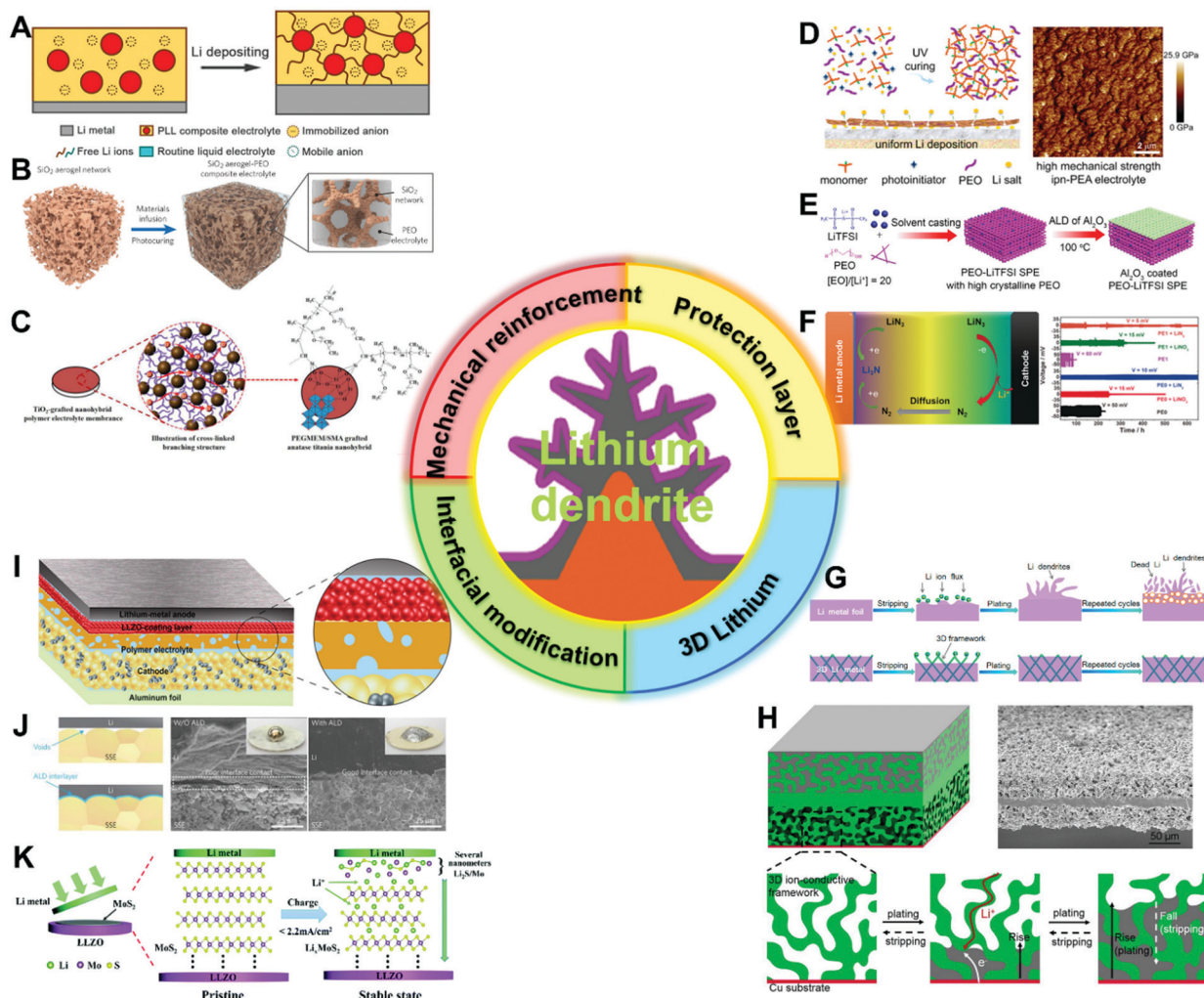


Fig. 15 Strategies for suppressing Li dendrites including mechanical reinforcement, protection layer, 3D lithium and interfacial modification. (A) Schematic of the Li electrochemical deposition with the PEO–LITFSI–LLZO (PLL) SSE. Reprinted with permission from ref. 93. Copyright 2017, National Academy of Sciences. (B) Schematic showing the synthetic procedures of the SiO₂–aerogel–reinforced SPE. Reprinted with permission from ref. 263. Copyright 2018, Wiley–VCH. (C) Schematic of TiO₂–grafted nanohybrid polymer electrolyte with a cross-linked branching structure. Reprinted with permission from ref. 270 Copyright 2016, Elsevier Ltd. (D) Proposed electrochemical deposition behaviour of Li metal with an ipn-PEA electrolyte and Young's modulus mapping of the ipn-PEA electrolyte. Reprinted with permission from ref. 73. Copyright 2016, American Chemical Society. (E) Schematic of the processes for coating Al₂O₃ on the PEO SPE by the ALD method. Reprinted with permission from ref. 278. Copyright 2019, Wiley–VCH. (F) Electrochemical reactions of LiN₃ in SSLBs and relative electrochemical performance of Li–Li symmetric cells, where PE0 is the PEO–LITFSI SSE and PE1 is the PEO–LITFSI SSE. Reprinted with permission from ref. 23. Copyright 2017, Wiley–VCH. (G) Schematic of the plating/stripping process of the 2D Li foil and 3D Li anode, reprinted with permission from ref. 280. Copyright 2019, Elsevier Ltd. (H) Schematic and SEM image of a 3D Li/LLZO anode and the relative stripping/plating process. Reprinted with permission from ref. 282. Copyright 2018, National Academy of Sciences. (I) Schematic of an SSLB with an asymmetric SSE. Reprinted with permission from ref. 286. Copyright 2018, American Chemical Society. (J) Schematic, optical images and SEM images of the Li–garnet interface and wetting behavior with/without an ALD–Al₂O₃ coating layer. Reprinted with permission from ref. 287. Copyright 2017, Nature Publishing Group. (K) Schematic diagram of the morphological and chemical evolution of the MoS₂–coating layer in the polarization process. Reprinted with permission from ref. 288. Copyright 2019, Royal Society of Chemistry.

surfaces for strong anion adsorption (Fig. 15B). The composite electrolyte delivered a high modulus of around 0.43 GPa and a high ionic conductivity of around 0.6 mS cm⁻¹ at 30 °C. As a result, a long cycling life of over 450 h was achieved by the assembled Li–Li symmetric cell at RT with an operating current density of 0.05 mA cm⁻². Moreover, a high areal capacity of up to 2.1 mA h cm⁻² was delivered by the Li–LFP full cell and it could stably run for 13 cycles at 55 °C (operating current density: 0.2 mA cm⁻²).²⁶³ In another study, an electrospinning

technique was applied for 3D LLZO network fabrication, which significantly enhanced the capability in blocking dendrites in Li–Li symmetric cells during repeated lithium stripping/plating at RT, with a current density of 0.2 mA cm⁻² for around 500 h and a current density of 0.5 mA cm⁻² for over 300 h.⁹⁶ To overcome the complicated processing such as electrospinning⁹⁶ aerogel,²⁶³ hydrogel,¹⁷⁶ and template methods⁴³ for large-scale electrolyte preparation, our group take advantage of the commercial glass fiber (GF) as feasible 3D scaffolds. The results demonstrated

excellent cycling stability of the Li–Li symmetric cells for over 1000 h at a current density of 0.42 mA cm^{-2} (areal capacity: 0.4 mAh cm^{-2}) at 60°C . For comparison, the Li–Li symmetric cells assembled with pure PEO electrolyte failed soon after 65 h because of a short-circuit. Additionally, the Li–LFP cell delivered a high areal capacity of $1.52 \text{ mA h cm}^{-2}$ for 50 cycles with a high LFP loading of 10.5 mg cm^{-2} .²⁶²

Fabrication of a 3D network *via* the cross-linking method is another effective strategy to enhance the mechanical properties for GPEs and SPEs.^{167,265–277} Archer's group cross-linked the PEO chains on the surface of nano-SiO₂ and constructed a 3D network. After activation with propylene carbonate (PC)–LiTFSI, the obtained GPE possessed high mechanical strength, high ionic conductivity as well as high flexibility. It has been demonstrated that the as-prepared GPE can tolerate the plating/stripping at 1 mA cm^{-2} for 150 h.²⁶⁶

Similar improvements in suppressing Li dendrite formation was also observed in SPEs *via* a cross-linking strategy. Zhang *et al.* reported an organic/inorganic hybrid polymer electrolyte *via* co-polymerizing poly(ethylene glycol) methyl ether methacrylate (PEGMEM), stearyl methacrylate (SMA) and AIBN and octavinyl octasilsesquioxane (OV-POSS). The electrochemical performance of Li–Li symmetric cells ($0.1\text{--}0.2 \text{ mA cm}^{-2}$, 200 h) demonstrated stability at both RT and 80°C .²⁷⁵ Moreover, the introduction of TiO₂ nanoparticles can further improve the mechanical strength (Fig. 15C). The cycle life can be further improved to 400 h at the 0.1 mA cm^{-2} . In another study, Wang and co-workers cross-linked poly(ϵ -caprolactone) (PCL) and SN on a 3D PAN-based substrate and achieved long RT-cycling performance of Li–Li symmetric cells within 600 h at 0.1 mA cm^{-2} .

2.3.2 Protection layer. Similar to Li protection in liquid systems, constructing a protective layer on the surface of the Li anode is also effective in solid-state systems. As shown in Fig. 15D, Guo and coworkers photopolymerized a branched acrylate onto an ion-conductive PEO matrix (labeled as ipn-PEA), which was applied as a thin coating layer on the surface of the Li anode. The results showed that the coating layer possessed a high modulus of 12 GPa, which is strong enough to suppress Li dendrite formation. The assembled Li–Li symmetric cell presented an excellent cycling performance of 130 h at a current density of 4 mA cm^{-2} (capacity: 1 mA h cm^{-2}).⁷³ A LiF (or LiI) coating layer, very important components of SEI in the liquid electrolyte, was introduced on the surface of the Li anode to inhibit the growth of Li dendrites in SSLBs. When heating the polished Li metal with methoxyperfluorobutane solvent (HFE) or I₂ powder in a sealed reactor at a high temperature of 150°C , a thin layer of LiF(LiI) formed on the surface of Li metal. Some HFE or I₂ also diffused into the Li₇P₃S₁₁ SSE. In addition to the positive effect for stabilizing the Li/Li₇P₃S₁₁ interface mentioned in Section 2.2.4, the LiF (LiI) layer can suppress the Li dendrite at high current densities. At 0.5 mA cm^{-2} , the Li–Li symmetric cells assembled with LiF and LiI protected Li demonstrated stable cycling performance for 200 h and 116 h, respectively, while a short-circuit was observed for the bare Li after 54 h. Besides the effect of the coating layer on inhibiting Li dendrite growth, the remaining HFE and I₂ played important roles in

helping Li dendrite suppression. When the Li dendrite penetrated the LiF (LiI) coating layer and grew into a Li₇P₃S₁₁ SSE through grain boundaries/cracks, reactions with HFE (or I₂) trapped in the SSE again consumed the Li dendrite and extended the cycle lives. The longer cycling life of the LiF coating than that of the LiI coating can be attributed to the high interface energy at Li/LiF, which improves the Li diffusion along with the Li/LiF interface and promotes a uniform Li deposition.²⁵⁴

Besides coating the protective layer on the surface of the Li anode, fabricating a coating layer on the surface of SSEs is another good choice to stabilize the Li/SSE interface. As shown in Fig. 15E, an Al₂O₃ coating on the PEO SPE was developed by Fan *et al.* to improve the poor Li/SSE interface as well as suppress the LiPS shuttle. With the protection layer, the cycling life of the Li–Li symmetric cells doubled compared with the pristine PEO SPE, which can stably run for over 500 h with low overpotentials of 0.05 V at 0.25 mA cm^{-2} . More importantly, the assembled Li–S batteries maintained a high capacity of 1080 mA h g^{-1} and CEs over 96% within 50 cycles, while obvious LiPS shuttle with low CEs was observed for the pristine PEO-based SSLBs.²⁷⁸

Compared with the *ex situ* coating layers, the *in situ* formation of a stable SEI on the surface of the Li anode by introducing electrolyte additives is more convenient and reliable on a large scale. Armand and co-workers introduced LiN₃ as an electrolyte additive to stabilize the Li anode interface. As shown in Fig. 15F, LiN₃ was reduced to N₂ at the cathode side and then diffused to the anode side for *in situ* formation of a Li₃N coating layer on the surface of the Li anode. The Li dendrite suppression capability of the coating layer has been demonstrated by the Li–Li symmetric cells in both PEO–LiTFSI (PE1) and PEO–LiFSI (PE0) SPEs. With the introduction of LiN₃, both PE1 + LiN₃ and PE0 + LiN₃ SPEs exhibited excellent cycling performance of over 650 h at 0.1 mA cm^{-2} , which are big improvements compared with electrolyte additive-free SPEs and a LiNO₃ additive. As a result, the assembled SSLBs presented excellent cycling stabilities. In another study, Archer's group introduced LiNO₃ and lithium bis(oxalato)borate (LiBOB) into the PEO–LiTFSI SPE to form a trinal salt SPE. Such a trinal salt SPE can *in situ* form stable SEIs on both anode and cathode surfaces, thus significantly improving the electrochemical performance of SSLBs.²⁷⁹

2.3.3 3D lithium. In SSLBs, planar lithium foils are widely used as the anode. Due to the inhomogeneous charge distribution on the imperfect surface of Li foil, Li is prone to deposit at defect sites, leading to lithium dendrite growth, even more serious at high current densities. Infusing Li into a 3D skeleton to form a 3D Li anode has been proved to be effective at inhibiting lithium dendrite growth.^{280–282} Chi *et al.* have reported a 3D Ni foam (as shown in Fig. 15G), acting as the 3D current collector to prevent the lithium dendrite growth. For the 2D planar Li foil, due to the non-uniform charge distribution on the surface of Li, Li prefers to grow as Li protuberances. The Li⁺ flux focused on the tips of those Li protuberances, resulting in Li dendrites and dead Li formation. In contrast, in the 3D Li anode, Li nucleation and growth tend to occur at the

surface of the protuberances of the 3D networks, which contributed to the uniform distribution of Li^+ and dendrite-free Li deposition. As a consequence, the 3D Li|SPE-LLZTO-SPE|3D Li symmetric cell delivered excellent cycling stability for over 700 h at 0.2 mA cm^{-2} (operating temperature: 90°C), while the occurrence of a short-circuit was observed after less than 100 h for the symmetric cell assembled with the 2D planar Li foil.²⁸⁰ Cui's group proposed to use rGO as a 3D host and thermally infiltrated a PEG-LITFSI SPE into the 3D Li-rGO structure to modify the surface. Benefitting from the reduced interfacial resistance as well as Li dendrite suppression capability, the assembled Li-Li symmetric cell delivered excellent cycling stability within 900 h with a low overpotential of 125 mV at a high current density of 0.5 mA cm^{-2} . For comparison, the planar Li foil-based symmetric cell exhibited a high average overpotential of 425 mV and failed after around 130 h because of short-circuiting. Additionally, a capacity retention of 93.6% was achieved by the Li-rGO/LFP SSLB after 300 cycles at a current density of 3 mA cm^{-2} .²⁸¹ Both the electrochemical performance of Li-Li symmetric cells and Li-LFP full cells demonstrated the promising application potential of 3D Li in SSLBs.

3D Li anodes are promising for inhibiting Li dendrite growth in oxide-based SSEs as well. Hu and co-workers developed a triple-layer $\text{Li}_7\text{La}_{2.75}\text{Ca}_{0.25}\text{Zr}_{1.75}\text{Nb}_{0.25}\text{O}_{12}$ (LLCZN) SSE with porous upper/bottom layers and a middle dense layer, as shown in Fig. 15H. A thin layer of ZnO coating was deposited by ALD on the upper layer to increase the Li wettability. When putting the SSE into melted Li, the Li filled the upper porous layer, while keeping the bottom layer empty. Benefitting from the unique 3D Li structure as well as high ionic conductivity of intrinsic LLCZN ($3 \times 10^{-4} \text{ S cm}^{-1}$ at RT), the aforementioned structure demonstrated a dendrite-free Li plating/stripping process. At a high current density of 0.5 mA cm^{-2} and a high areal capacity of 1 mA h cm^{-2} , the 3D Li exhibited long cycling life of over 300 h within a low overpotential of around 20 mV.²⁸² A similar triple-layer LLZO structure was created by the 3D printing method for Li infusion. Due to the minimized local current densities during plating/stripping, the assembled Li-Li symmetric cell can be cycled at a current density of 0.33 mA cm^{-2} with a low overpotential of 7.2 mV.²⁸³

2.3.4 Interfacial modification. Interfacial modification not only can suppress unfavorable Li/SSE interfacial reactions (as discussed in Section 2.2.2) but also plays an important role in Li dendrite suppression. In this section, we will discuss the interfacial modification tailored to Li dendrite inhibition, mainly focused on the rigid ceramic/Li interface. It is known that the ceramic SSEs possess a high Young's modulus but poor flexibility, resulting in "point-to-point" contact instead of "plane-to-plane" contact. The incomplete contact leads to inhomogeneous charge distribution and large interfacial resistance, which lead to large overpotentials and Li dendrite growth.^{284,285} Improving the Li/SSE interfacial contact and reducing the interfacial resistance *via* interfacial modification show the promising application in alleviating Li dendrite formation.

Guo's group developed an asymmetric solid electrolyte (ASE) by coating the LLZO particles with PEO as a binder on one side

of a Celgard 2400 separator and *in situ* polymerizing polymer electrolyte solution on the other side (Fig. 15I). Due to the high Young's modulus of LLZO as well as the optimized interface, the assembled Li-Li symmetric cell demonstrated an ultra-long cycling life of over 3200 h at 0.1 mA cm^{-2} at 55°C .²⁸⁶ The Li/SSE interfacial resistance can be further reduced by solidifying molten Li on the surface of SSEs. The construction of a lithiophilic surface is the key. As shown in Fig. 15J, pristine LLCZN exhibited very poor Li wettability and the molten Li presented a large contact angle on the surface of LLCZN. After coating with ALD Al_2O_3 coating and Li-Al alloy coating, the lithiophobic surface of LLCZN changed into lithiophilic, and the Li-LLCZN contact angles were significantly reduced. As a result, lower interfacial resistance and improved Li dendrite suppression capability were obtained.^{140,287} The Li-Li symmetric cell assembled with ALD Al_2O_3 coated LLCZN could stably run for 90 h with a low overpotential of around 25 mV at 0.2 mA cm^{-2} , while serious short-circuiting was observed for pristine LLCZN even at a low current density of 0.1 mA cm^{-2} (operating temperature: 55°C).²⁸⁷ Liu's group proposed to reduce the interfacial resistance and prevent lithium dendrite growth simultaneously through *in situ* formation of interlayers of Li_xMoS_2 by introducing MoS_2 layers on an LLZO pellet, as shown in Fig. 15K. The interfacial resistance was notably reduced from over one hundred to only $14 \Omega \text{ cm}^2$ and the critical current density of cells was improved from 0.7 mA cm^{-2} to 2.2 mA cm^{-2} .²⁸⁸ Recent works suggested that the intrinsic garnet-SSE such as LLZO is actually lithiophilic, which exhibited good Li wettability on its surface. It is the formation of Li_2CO_3 on its surface upon exposure to air (moisture and CO_2) that turns the surface from lithiophilic to lithiophobic.²⁴⁵⁻²⁴⁷ Therefore, several strategies aimed to remove the Li_2CO_3 layer, such as mechanical polishing, high-temperature thermal treatment, and acid treatments, have been developed to improve the Li wettability and reduce the interfacial resistance. For example, our group developed a rapid acid treatment by immersing the LLZO pallet into a 1 M HCl solution for 30 s to completely remove the Li_2CO_3 layer. The interfacial resistance was reduced a lot and the electrochemical performance of Li-Li symmetric cells was improved. The Li-Li symmetric cell assembled with the Li_2CO_3 -free LLZO pallet presented stable RT-plating/stripping for over 700 h at 0.2 mA cm^{-2} with a low overpotential of less than 50 mV. In another study, Ruan *et al.* proposed to transfer the lithiophobic Li_2CO_3 into lithiophilic H_3PO_4 *via* an acid-induced conversion method. The Li-LLZO interface resistance was reduced. RT cycling was demonstrated to be stable over 450 h at a current density of 0.5 mA cm^{-2} and an areal capacity of $0.25 \text{ mA h cm}^{-2}$.²⁸⁹

In brief summary, all aforementioned strategies demonstrated promising Li dendrite suppressing capability. However, it should be noted that most Li-Li symmetric cell performances were evaluated at low current densities ($<0.5 \text{ mA cm}^{-2}$) and low capacities ($<0.5 \text{ mA h cm}^{-2}$), which limited the improvements of C-rate and sulfur loading for SSLBs. Therefore, evaluation of performance under high current densities and high capacities is important.

For the mechanical reinforcement strategy, it is very difficult to enhance the overall Young's modulus of SPEs over lithium by introducing inorganic fillers, 3D scaffolds and cross-linking structures. When operating the cells at relatively high current densities or high areal capacities, Li dendrites can still penetrate the SPEs. Hence, it would be better to combine with interfacial modification or protection layers to promote uniform Li deposition and alleviate Li dendrite problems.

For the *ex situ* protection layer design, the ionic conductivity of the protection layer should be taken into consideration. In a liquid system, the liquid electrolyte can easily wet the protection layers, where the interfacial resistance could be negligible, but solid-state systems are different because the SSEs are not likely to diffuse into the protection layer. In the solid-state systems, the low ionic conductive protection layer will result in large interfacial resistance and large overpotential, thus leading to fast Li dendrite growth and low discharge voltage as well. In this regard, designing a high ionic conductive protection layer on the surface of Li anode is needed for SSLSBs. Additionally, the thickness of the protection layers is another consideration. The thin protective layer is easy to be broken by the Li dendrite or during cell assembly. The thick layer will limit the Li^+ transport between the SSE and Li anode. It should be well balanced for practical applications. Different SSLSB systems may require different optimal thicknesses. The *in situ* formation of protection layers by electrolyte additives is a large-scale reliable process and the protection layers can be re-formed/repared during cycling. However, the continuous consumption of additives could eventually experience a failure due to shortage of the regeneration of favorable SEI or accumulation of too much dead SEI for an overwhelming overpotential. Cycling with high sulfur loading electrodes is particularly problematic because of the large cycling capacity and current densities. Hence, the development of more stable and effective lithium protection methods is still crucial for SSLSBs.

The 3D current collectors can provide a high specific surface for stable Li deposition, thus limiting the Li dendrite growth. Nevertheless, it should be noted that Li deposition can only occur at the Li^+/e^- conductive dual-phase interfaces. It can be easily realized based on flowable liquid electrolytes, but it is a big challenge to build homogeneous Li^+/e^- conductive dual-phase interfaces in the anode of SSLSBs. Additionally, most of the SSEs are not 100% stable against Li metal. The 3D Li anodes have high surface areas for forming interfaces with SSEs, leading to more reactions with SSEs if they are not stable with each other. It would be more serious in a solid-liquid dual-phase SSLSB system where LiPSs will also participate in the reaction with Li metal. For practical applications, both the stability of SSEs to Li metal and LiPSs should be taken into consideration.

3. Guidelines for SSLSB pouch cells

The key issues such as the shuttle effect, interfacial instability, and Li dendrite growth significantly limit the electrochemical

performance and hinder the practical application of SSLSBs. Similar to the liquid Li-S batteries, SSLSBs are condition-dependent devices. Under different testing conditions such as different sulfur loadings, cathode sulfur contents, and options of SSEs, the electrochemical performance can vary a lot. SSLSBs aim to provide power/energy for advanced electric vehicles and portable electronic devices, which put forward high requirements in both gravimetric energy density and volumetric energy density.²⁹⁰ Hence, on the basis of solving the fundamental research limitations, we need to clarify the requirements for the engineering of high energy SSLSBs. It is more reasonable to propose effective strategies to solve the problems for SSLSBs under practical standards. Hence, in the following sections, we will evaluate the SSLSB components in terms of their effects on gravimetric and volumetric energy densities. The engineering requirements for SSLSBs to realize high energy densities of 500 Wh kg^{-1} will be summarized according to our comprehensive evaluations. After statistical analysis of various parameters associated with the energy densities in recent publications, we will identify the factors that fall short for SSLSB development. We hope that these analyses are helpful for guiding rational designs for SSLSB engineering.

3.1 Effects of SSLSB components on gravimetric energy density

Gravimetric energy density, one of the most important parameters, is widely used to estimate the performance of energy storage devices. The simulated components of SSLSBs coupled with various SSEs based on a pouch cell setup are listed in Table 1 to evaluate the practical gravimetric energy density. As for liquid electrolyte-based Li-S batteries, sulfur loading is an important parameter that plays a role in practical gravimetric energy density;^{3,291} this is also applicable for SSLSBs. Here we specifically evaluate the effect of sulfur loading on gravimetric energy density for SSLSBs. Among various components in Table 1, the weight of the current collector is fixed. The other components such as binder, Li anode and carbon additive are scaled according to the sulfur loading. The cathode composition is set as 50 wt% sulfur and 10 wt% binder, 13.3 wt% carbon additive, and 26.7 wt% SSE. The weight ratio of carbon additive and SSE is chosen as 1 : 2 to make sure sufficient e^-/Li^+ transport. In the liquid systems, the E/S ratio is controlled at higher than $3 \mu\text{L mg}^{-1}$ to ensure a high discharge capacity output as well as a relatively long cycling life. In the SSLSBs, the SSE serves not only as the separator but also as a component of the cathode layer to facilitate Li^+ transport. In the cathode layer, an SSE/S ratio of less than 1 is possible according to the recently reported publications.^{32,120} In this context, SSLSBs have the potential to deliver a higher gravimetric energy density compared with liquid systems. However, the Li dendrite problem could be more challenging for SSLSBs than the liquid electrolyte-based cells. In the liquid Li-S batteries, Li dendrites could vanish due to the chemical reactions with the soluble LiPSs and electrochemical reactions with the LiNO_3/FEC additives to form a SEI productive layer.^{3,16,155,292,293} A separator with a thickness of around $25 \mu\text{m}$ (e.g. Celgard 2325) is enough

to prevent a short circuit. In oxide- and sulfide-SSE based SSLSBs, the Li dendrite can easily penetrate the SSE separator to cause a short circuit by growing along the grain boundaries of SSEs. Moreover, the mechanical properties of SSEs with a low thickness of around 20 μm are not as flexible as those of the polypropylene (PP) separators. The oxide and sulfide SSEs are very brittle, especially for the SSEs with large particle sizes. Fabrication of thin SSEs is still challenging. Considering the relatively high density of SSEs, the thickness of SSE separators as another important parameter is evaluated for gravimetric energy density calculation. Practical gravimetric energy density is calculated based on eqn (1).

$$M_{\text{Gravimetric energy density}} = \frac{E \times Q \times \text{Ar}_{(\text{S})} \times m_{\text{S}}}{\text{Ar}_{(\text{Li}_2\text{S})} \times m_{\text{Total}}} \quad (1)$$

where $\text{Ar}_{(\text{S})}$ and $\text{Ar}_{(\text{Li}_2\text{S})}$ are the relative atomic mass of S (32) and Li_2S (46), respectively; E is the average discharge voltage; Q is the specific discharge capacity based on sulfur; m_{S} is the areal sulfur loading; and m_{Total} is the total weight of the SSLSB soft packages listed in Table 1.

Herein, we calculated the gravimetric energy density based on six different SSEs including an SPE, oxide SSE, sulfide SSE and three hybrid SSEs. For the SPE (Fig. 16A), we adopt the widely used PEO composition with an EO/Li^+ ratio of 16/1, where the Li salt is LiTFSI. The density of the PEO SPE is approximately 1.24 g cm^{-3} (considering the density of PEO polymer as 1.21 g cm^{-3} and LiTFSI as 1.33 g cm^{-3}). For the oxide-based SSE (Fig. 16B), LLZO with a density of 5.1 mg cm^{-2} is chosen as the representative because of its high chemical and electrochemical stabilities. For the sulfide SSE (Fig. 16C), considering the serious side reactions between LGPS and the Li anode, here the combination of double layers of LGPS and LPS is considered to make sure both the chemical stability and ionic conductivity. The weight ratio of LGPS to LPS is set as 1 : 1. In this case, the density of sulfide-based SSE is 1.96 g cm^{-3}

(the densities of LGPS and LPS are 2.05 g cm^{-3} and 1.87 g cm^{-3} , respectively). The three hybrid SSEs are chosen as the PEO SPE compositing with LLZO fillers in different weight ratios. The incorporation of inorganic filler has been reported to significantly improve the ionic conductivity and mechanical properties. The weight ratios are set as 15 wt%, 50 wt% and 80 wt%, labeled as Hybrid-15 (Fig. 17A), Hybrid-50 (Fig. 17B) and Hybrid-80 (Fig. 17C) SSEs, respectively. These three compositions cover the range from “ceramics-in-polymer” to “polymer-in-ceramics”. The densities of the Hybrid-15, Hybrid-50 and Hybrid-80 SSEs are 1.40 g cm^{-3} , 2.00 g cm^{-3} and 3.14 g cm^{-3} , respectively. Since the dense structure is beneficial for fast Li^+ transport in SSEs, the porosity of all aforementioned SSEs is neglected for the simulation.

As shown in Fig. 16D–F, with a fixed thickness of SSEs, the gravimetric energy density generally increases with increasing sulfur loading. However, it should be noted that the increase in gravimetric energy density is more significant at relatively low sulfur loadings and levels off towards high sulfur loadings, especially for the SSEs with a thickness of lower than 50 μm . For instance, with an SSE thickness of 30 μm , when the sulfur loading increases from 1 to 6 mg cm^{-2} the gravimetric energy densities are increased from 312, 259 and 150 W h kg^{-1} to 835, 766 and 563 W h kg^{-1} for SPE, sulfide SSE, and oxide SSE based systems. However, a further increase in the sulfur loading to 10 mg cm^{-2} (vs. 6 mg cm^{-2}) leads to relatively small increases of 129, 141 and 159 W h kg^{-1} .

The trend for SSEs with thicknesses above 100 μm is quite different. The relationship between gravimetric energy density and sulfur loading is almost linear, especially for the high-density oxide SSE. For instance, at a SSE thickness of 500 μm and a sulfur loading of 5 mg cm^{-2} , SPE, sulfide- and oxide-SSE based SSLSBs can achieve gravimetric energy densities of 209, 144, and 61 W h kg^{-1} , respectively, which are almost 5 times those of the corresponding SSLSBs with 1 mg cm^{-2} sulfur loading (48, 32 and 13 W h kg^{-1}). With an even higher sulfur loading of 10 mg cm^{-2} , the corresponding gravimetric energy densities are further increased to 359, 259 and 117 W h kg^{-1} for SPE, sulfide- and oxide-SSE based SSLSBs, respectively, doubling the values of SSLSBs with 5 mg cm^{-2} sulfur. It is mainly attributed to the high weight ratio of SSEs with a high thickness and the increased sulfur loading has a negligible effect on the total weight for soft-package SSLSBs. Considering a cell with a sulfur loading of 1 mg cm^{-2} and 500 μm oxide SSE, the total weight of the pouch cell is 275.8 mg cm^{-2} , in which the weight ratios of sulfur and SSE are 3.6 wt% and 92.6 wt%, respectively. When the sulfur loading increases to 5 mg cm^{-2} , the total weight of the pouch cell is 286.9 mg cm^{-2} . The sulfur ratio increases to 17.4 wt%, almost 5-fold that with a loading of 1 mg cm^{-2} . For both thin SSEs and thick SSEs, the sulfur loading has a great impact on the gravimetric energy density of SSLSBs. However, the SSLSBs assembled with thick SSEs (> 200 μm) cannot meet the requirements of practical SSLSBs with 500 W h kg^{-1} (Fig. 16D–F). Therefore, we will focus our discussion on the SSLSBs based on thin SSEs (< 100 μm).

As high sulfur loading is essential for high-energy-density SSLSBs, is there a ceiling sulfur loading? It is noteworthy that

Table 1 Components of SSLSB soft packages for gravimetric energy density simulation

Components	Mass (mg cm^{-2})
Cathode current collector (aluminum foil, 16 μm)	4.32
Sulfur ^a	x
Binder (PVDF) ^b	$0.2x$
Carbon ^c	$0.27x$
SSE ^d	$\rho t + 0.53x$
Anode (lithium metal) ^e	$0.66x$
Others (cathode tap, anode tap, Al laminate film, etc.) ^f	$0.23 + 0.14x + 0.05\rho t$
Total	$4.55 + 2.80x + 1.05\rho t$

^a Areal sulfur loading is $x \text{ mg cm}^{-2}$, where the sulfur content is controlled as 50 wt% based on the whole cathode. ^b There is 10 wt% binder in the cathode. ^c Except for the sulfur and binder in the cathode, the weight ratio of the carbon and SSE is controlled as 1 : 2 in order to maintain the fast e^-/Li^+ transport. ^d Including the SSE as a separator and SSE in the cathode for Li^+ transport. ρ and t are the density and thickness of the SSE as a separator. $0.53x$ is the SSE in the cathode. ^e 50 wt% lithium excess accords to the stoichiometric ratio of sulfur. ^f The mass ratio of other components such as the cathode tap, anode tap, and Al laminate film is 5 wt% of the whole SSLSB soft packages.

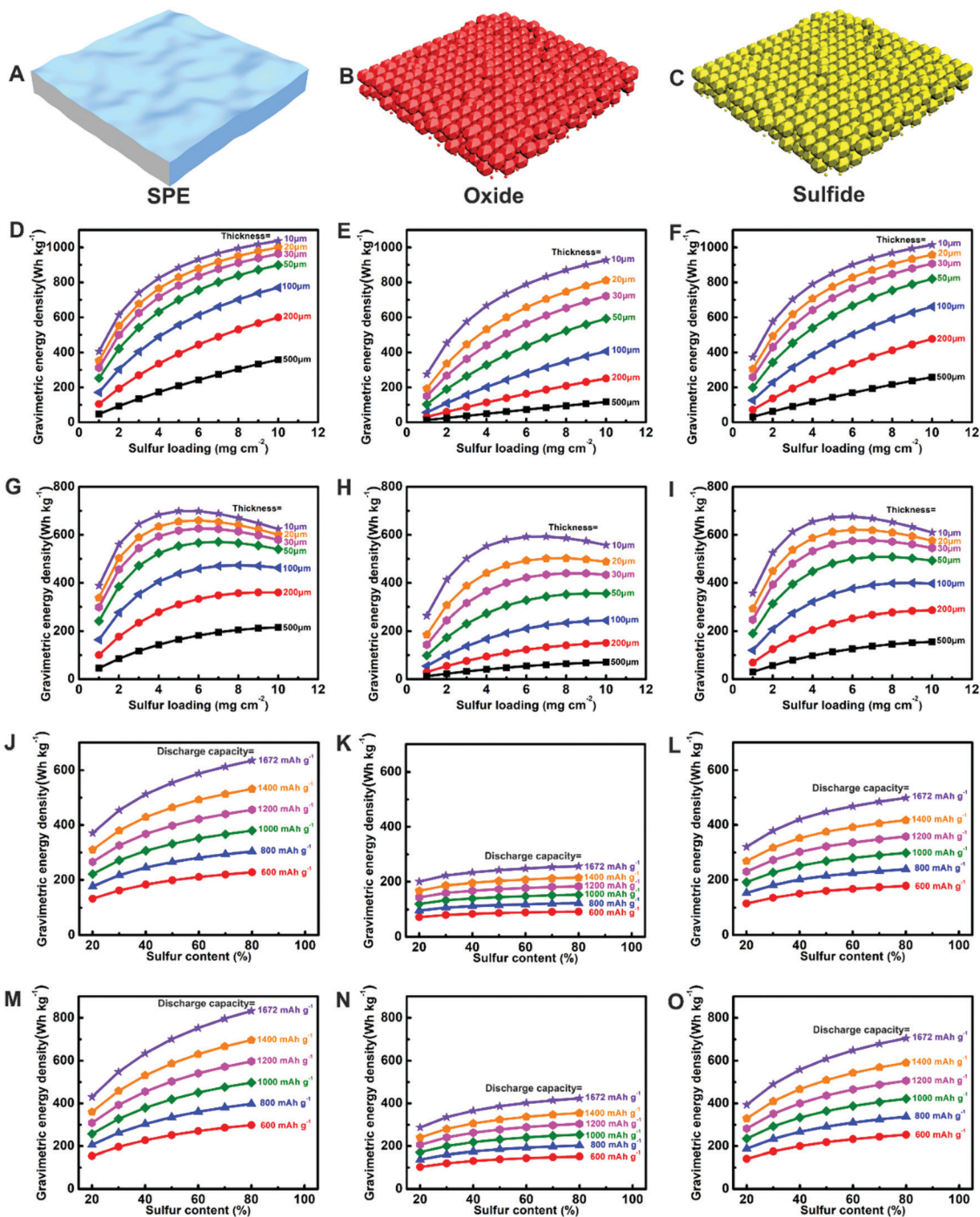


Fig. 16 Estimating the practical gravimetric energy density of SSLSB with (A) SPE, (B) oxide-based and (C) sulfide-based SSEs. (D–F) Gravimetric energy density calculated based on a theoretical discharge capacity of 1672 mA h g^{-1} and an average discharge voltage of 2.1 V as a function of sulfur loading for various thicknesses of SSEs. (G–I) Gravimetric energy density calculated based on various theoretical discharge capacities and average discharge voltages (discharge capacity = $(1672 - 50x) \text{ mA h g}^{-1}$, average discharge voltage = $(2.1 - 0.03x) \text{ V}$, x is the sulfur loading) as a function of sulfur loading for various thicknesses of SSEs. Gravimetric energy density calculated based on an optimized sulfur loading of 5 mg cm^{-2} and thicknesses of (J–L) $100 \text{ }\mu\text{m}$ SSE and (M–O) $50 \text{ }\mu\text{m}$ SSE as a function of sulfur content for various discharge capacities.

the gravimetric energy densities shown in Fig. 16D–F are calculated based on a theoretical discharge capacity of 1672 mA h g^{-1} and an average theoretical voltage of 2.1 V , which is overestimated compared to SSLSBs in practical operation. In particular for SSLSBs assembled with high sulfur

loading cathodes, the increase of sulfur loading is always at the cost of decreased specific capacities and larger overpotential. Moreover, the possible Li dendrite growth and large volumetric fluctuation on both the cathode and anode sides need to be taken into consideration. These factors are omitted

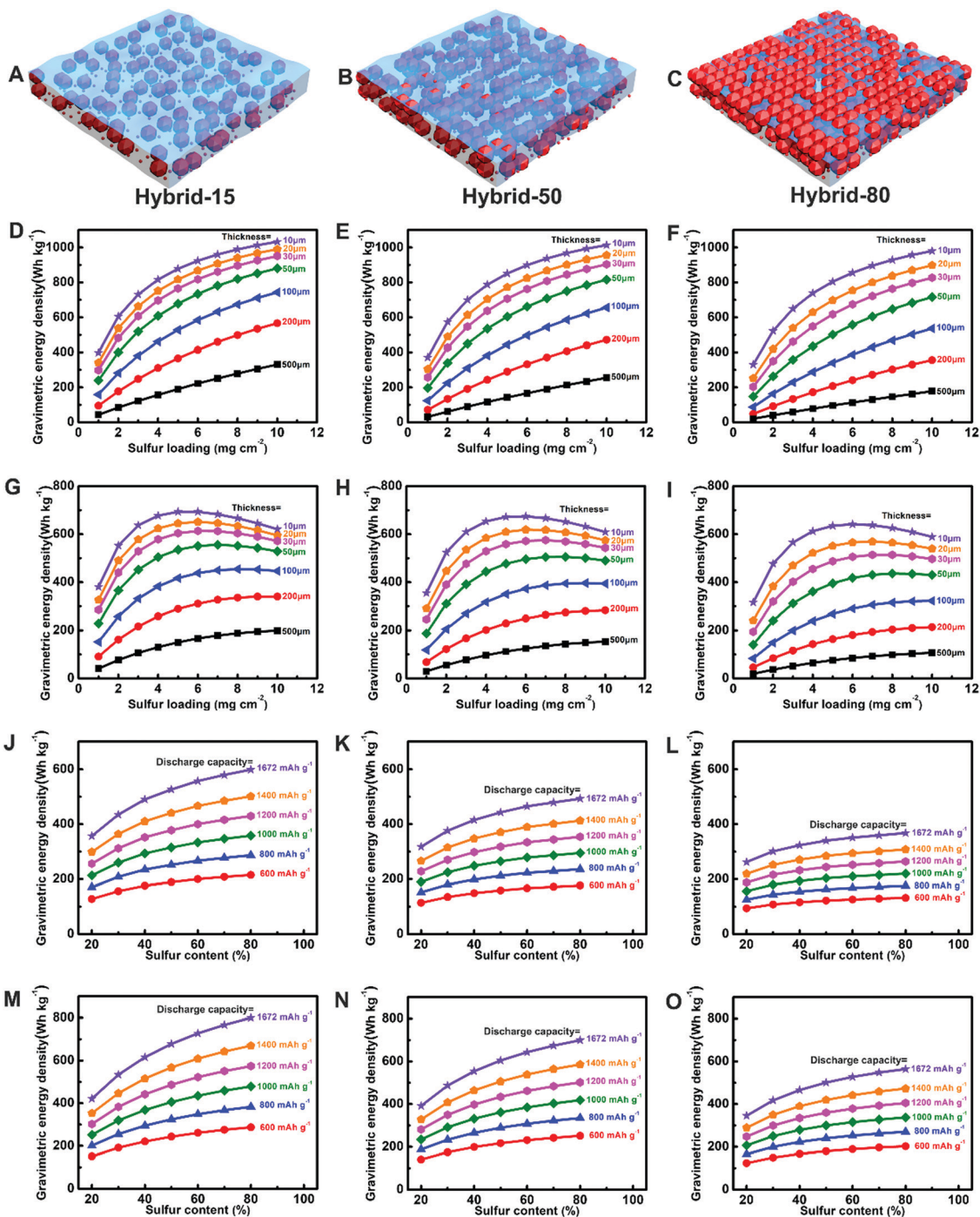


Fig. 17 Estimating the practical gravimetric energy density of SSLSB with (A) Hybrid-15, (B) Hybrid-50 and (C) Hybrid-80 SSEs. (D–F) Gravimetric energy density calculated based on the theoretical discharge capacity of 1672 mA h g^{-1} and average discharge voltage of 2.1 V as a function of sulfur loading for various thicknesses of SSEs. (G–I) Gravimetric energy density calculated based on various theoretical discharge capacities and average discharge voltages (discharge capacity = $(1672 - 50x) \text{ mA h g}^{-1}$, average discharge voltage = $(2.1 - 0.03x) \text{ V}$, x is the sulfur loading) as a function of sulfur loading for various thicknesses of SSEs. Gravimetric energy density calculated based on an optimized sulfur loading of 5 mg cm^{-2} and thicknesses of (J–L) $100 \text{ }\mu\text{m}$ SSE and (M–O) $50 \text{ }\mu\text{m}$ SSE as a function of sulfur content for various discharge capacities.

here but will be discussed in later sections. We now focus only on the cathode utilization and efficiency related to sulfur loading. Let us reasonably assume that every 1 mg cm^{-2} increase in sulfur loading will lead to a 50 mA h g^{-1} loss of discharge capacity and a 30 mV drop of discharge voltage. The

relationships between gravimetric energy density and sulfur loading obviously change based on different SSEs and thicknesses, as shown in Fig. 16G–I. The gravimetric energy densities of SSLSBs increase up to a certain sulfur loading and then decrease gradually upon a further increase in sulfur loading.

In other words, there is an optimal sulfur loading for practical applications. Particularly for thin SSEs with a thickness of less than 50 μm , the optimal sulfur loadings almost range between 4 mg cm^{-2} and 6 mg cm^{-2} .

The thickness of SSEs is another critical parameter that shows a significant influence on the gravimetric energy density of SSLSBs. As shown in Fig. 16D–F, for the theoretical simulation, the gravimetric energy densities dramatically decreased upon an increasing thickness of SSE, due to the decreased sulfur composition in the soft package, especially for the SSLSBs with high sulfur loadings. For SSLSBs with a sulfur loading of 1 mg cm^{-2} in the cathode, the gravimetric energy densities of SSLSBs with 10 μm SPE, sulfide SSE, and oxide SSE are 388, 357 and 264 W h kg^{-1} , respectively, which are 342, 326 and 252 W h kg^{-1} higher than cases with 500 μm (48, 32 and 13 W h kg^{-1} in orders); the differences are further increased to 679, 756, and 810 W h kg^{-1} when the sulfur loading is increased to 10 mg cm^{-2} . Therefore, high-loading cathodes should be coupled with thin SSEs to ensure high gravimetric energy density output for SSLSBs. Nevertheless, limited by fabrication viability and poor mechanical properties of thin SSEs, the recently reported thickness of SSEs is mostly higher than 50 μm for SPEs and higher than 200 μm for oxide- and sulfide-based SSEs.^{39,147,221,262}

Based on our calculations, the energy density of SSLSBs with the reported high thickness cannot reach 300 W h kg^{-1} for oxide- and sulfide-based SSEs and cannot meet the demand for long-range electric vehicles. Hence, in the next research stage, the development of thin oxide- and sulfide-based SSEs is of significance. For SPEs, the thickness is acceptable for achieving a gravimetric energy density of 500 W h kg^{-1} . Whether it can meet the requirement of dendrite-free Li deposition and shuttle resistance even with high-loading cathodes should be further explored. Generally speaking, if we want to achieve a high gravimetric energy density of 500 W h kg^{-1} , the thickness of SSEs should be controlled to below 50 μm for SPEs, 30 μm for sulfide SSEs, and 20 μm for oxide-based SSEs.

In addition to physical parameters of sulfur loading and SSE thickness, other electrochemical performance related parameters such as sulfur content and discharge capacity also have a great influence on the practical gravimetric energy density. The simulation results are calculated based on an optimal sulfur loading of 5 mg cm^{-2} with 100 μm (Fig. 16J–L) and 50 μm (Fig. 16M–O) SSEs that have the potential to be realized in the near future. For the SSLSBs assembled with 100 μm SSEs (Fig. 16J–L), only SPEs with a theoretical discharge capacity of 1672 mA h g^{-1} and a sulfur content of 40 wt% have the potential to achieve 500 W h kg^{-1} , while both oxide- (less than 250 W h kg^{-1}) and sulfide-based SSEs cannot meet the demand under all conditions. Considering the overestimation of full theoretical capacity (1672 mA h g^{-1}) at the condition of 40% sulfur content and sulfur loading of 5 mg cm^{-2} for SPE based SSLSBs, it is impossible to realize a high gravimetric energy density of 500 W h kg^{-1} with an SSE thickness of 100 μm .

Simulation results based on a more demanding thickness of 50 μm for SSEs are exhibited in Fig. 16M–O. The oxide SSE

based SSLSBs cannot achieve 500 W h kg^{-1} under all conditions. This means that an oxide-based SSE with high density is not suitable for high-energy-density SSLSBs unless there is a breakthrough in the development of ultrathin SSE fabrication. The design of thin SSEs is an urgent goal for oxide SSE-based SSLSBs. For SPE and sulfide SSE-based SSLSBs, discharge capacities and sulfur content of 1200 $\text{mA h g}^{-1}/50 \text{ wt}\%$ and 1400 $\text{mA h g}^{-1}/50 \text{ wt}\%$ are essential for realizing 500 W h kg^{-1} . Based on published works, a discharge capacity higher than 1200 mA h g^{-1} was demonstrated to be possible for SSLSBs with relatively low sulfur loadings.^{35,208} However, the situation is quite different for the batteries with high sulfur loading and high sulfur contents due to the poor Li^+/e^- transport and serious volume change during cycling. It should also be noted that rechargeable SSLSBs are aimed to supply power for several thousands of cycles and maintain good performance. Long cycle lives and high performance are still challenging at the current stage. Additionally, a feasible power density requires SSLSBs to charge/discharge at a reasonable rate which is beyond the current level as well. As the sulfur content increases, the ratios of both the electron conductor and Li-ion conductor will decrease, which will worsen the Li^+/e^- transport in the cathode. From the simulation results in Fig. 16M–O, the sulfur content shows a less significant effect on the gravimetric energy density when the sulfur content is higher than 50 wt%. For example, the gravimetric energy densities are 503 and 510 W h kg^{-1} , which are 195 and 181 W h kg^{-1} higher than their counterparts with a sulfur content of 20 wt%, respectively. Further increasing the sulfur content to 80 wt%, only 95 and 80 W h kg^{-1} improved compared with 50 wt% sulfur content. Taking both gravimetric energy density and Li^+/e^- transport into consideration, a sulfur content of 50 wt% is reasonable.

Beyond single-component SSEs, hybrid SSEs that consist of two or more types of SSEs/fillers show a potential balance of the merits and drawbacks of each component. Herein, typical PEO-based hybrid electrolytes with 20 wt%, 50 wt% and 80 wt% LLZO fillers (labeled Hybrid-20, Hybrid-50 and Hybrid-80, respectively) are chosen to investigate the relationships among gravimetric energy density, sulfur loading, sulfur content and discharge capacity output. The simulation results are shown in Fig. 17. In terms of gravimetric energy density, the Hybrid-20 and Hybrid-50 SSEs present densities of 1.40 and 2.00 g cm^{-3} , comparable to the SPE and sulfide-based SSE results. Hence, all the relationships and targets are similar to that of SPEs and sulfide-based SSEs, thus we will focus our discussion on the Hybrid-80 SSE for different possibilities.

As shown in Fig. 17F, based on the theoretical discharge capacity and discharge voltage, 50 μm Hybrid-80 SSE coupled with a cathode of sulfur loading 4 mg cm^{-2} is enough for 500 W h kg^{-1} . If the thickness of the Hybrid-80 SSE is decreased to lower than 30 μm , 2–3 mg cm^{-2} sulfur loading can also achieve the target. Of course, it is still under ideal conditions and is overestimated. Fig. 17I presents the simulation results based on a 50 mA h g^{-1} discharge capacity loss and a 30 mV discharge voltage drop for every 1 mg cm^{-2} increase in sulfur loading.

The optimized sulfur loading range of 4–6 mg cm⁻² is still suitable for the thin Hybrid-80 SSEs with thicknesses of lower than 50 μm. Gravimetric energy densities of roughly 400, 500, 550, and 640 W h kg⁻¹ with SSE thicknesses of 50, 30, 20, and 10 μm, respectively, can be obtained in the optimal sulfur loading range. Therefore, a thin Hybrid-80 SSE of below 30 μm is essential for achieving the target of 500 W h kg⁻¹. Besides, the relationships between gravimetric energy density, sulfur content, and discharge capacity (based on an optimal sulfur loading of 5 mg cm⁻²) are investigated based on Hybrid-80 SSE thicknesses of 100 μm (Fig. 17L) and 50 μm (Fig. 17O). As shown in Fig. 17L, the gravimetric energy densities are all lower than 400 W h kg⁻¹, even under the theoretical discharge capacity/voltage and 10 mg cm⁻² sulfur loading. In other words, the 100 μm Hybrid-80 SSE is too thick to achieve the target. Fig. 17O shows the simulation results based on 50 μm Hybrid-80 SSE. The SSLSBs can reluctantly reach the target of 500 W h kg⁻¹ with a theoretical discharge capacity of 1672 mA h g⁻¹ and a sulfur loading of 5 mg cm⁻². This suggests that 50 μm is still not thin enough. Developing a thinner SSE is the main direction in the next research step for the Hybrid-80 SSE.

In summary, according to the simulation results, SPE, sulfide SSE, Hybrid-20 and Hybrid-50 with low densities show more promising application prospects in terms of high gravimetric energy density. To achieve a high gravimetric energy density of 500 W h kg⁻¹, high sulfur loading, high discharge capacity, low SSE thickness and relatively high sulfur content are the prerequisites. Taking the Li⁺/e⁻ transport and cycling volumetric charge into consideration, the optimized sulfur loading range is 4–6 mg cm⁻². With a discharge capacity of higher than 1200 mA h g⁻¹ by coupling low thicknesses of 50, 30 and 20 μm, respectively, SPE/Hybrid-20, sulfide-based SSE/Hybrid-50, and oxide-based/Hybrid-80 SSEs have the potential to reach the target. Generally, a higher energy density can be obtained by increasing the sulfur content in the cathode. However, due to the worsening Li⁺/e⁻ transport upon decreasing the ratios of Li-ion and electron conductors and the weakened effect on the gravimetric energy density at a relatively high sulfur content (>50 wt%), an optimal sulfur content of 50 wt% is reasonable. Considering the sulfur content is available at the recent research stage, preparation of ultrathin SSEs (typically <50 μm) and development of high-performance high-sulfur-loading cathodes are the main directions for the next-step forward.

3.2 Effects of SSLSB compositions on volumetric energy density

In addition to the practical gravimetric energy density, the volumetric energy density is another important parameter to evaluate the potential of SSLSBs for practical applications. The volumetric energy density is mainly determined by the tap density of the cathode, the sulfur content in the cathode, the sulfur loading in the cathode, and the thickness of the SSE. Considering the total thickness of practical pouch-cell SSLSBs can be on the centimeter scale by stacking multiple electrode/SSE layers, the thickness of the sealing package on the

micrometer scale is neglected for the following simulations. Firstly, we simulated the volumetric energy density and sulfur loading based on different SSE thicknesses (Fig. 18D–I) based on SPE, oxide- and sulfide-SSEs (Fig. 18A–C). Calculations in Fig. 18D–F are based on a theoretical discharge capacity of 1672 mA h g⁻¹ and an average voltage of 2.1 V, while Fig. 18G–I present the simulation results based on a 50 mA h g⁻¹ discharge capacity loss and a 30 mV discharge voltage drop for every 1 mg cm⁻² sulfur loading increase. The volumetric energy density is determined by eqn (2).

$$M_{\text{Volumetric energy density}} = \frac{E \times Q \times \text{Ar}_{(\text{S})} \times m_{\text{S}}}{\text{Ar}_{(\text{Li}_2\text{S})} \times T_{\text{Total}}} \quad (2)$$

where T_{total} is the total thickness of the pouch cell and the other terms are defined to be the same as for the gravimetric energy density simulation (eqn (1)).

The T_{total} simulation process is summarized in Table 2, where t , ρ_{Cathode} , ω_{S} , and x are the thickness of SSE, the tap density of the cathode, the sulfur content in the cathode, and areal sulfur loading, respectively. ρ_{Cathode} is determined by eqn (3).

$$\rho_{\text{Cathode}} = \frac{(1 - \rho_{\text{Cathode}})}{\left(\frac{\omega_{\text{S}}}{\rho_{\text{S}}}\right) + \left(\frac{0.1}{\rho_{\text{Binder}}}\right) + \left(\frac{0.9 - \omega_{\text{S}}}{3\rho_{\text{Carbon}}}\right) + \left(\frac{1.8 - 2\omega_{\text{S}}}{3\rho_{\text{SSE}}}\right)} \quad (3)$$

where ρ_{S} , ρ_{Binder} , ρ_{Carbon} and ρ_{SSE} are the density of sulfur (2.07 g cm⁻³), binder, carbon additive, and SSE, respectively; and P_{Cathode} is the porosity of the cathode. For the simulation, the widely used PVDF and Super P are adopted as the representative binder and carbon additive with corresponding densities of 0.8 and 0.16 g cm⁻³, respectively. In the simulation of Fig. 18D–I, we choose ω_{S} of 50 wt% and P_{Cathode} of 15% considering 80% volumetric expansion during lithiation.

Interestingly, with the same SSE thickness and sulfur loading, the type of SSE shows a negligible effect on the volumetric energy density. This phenomenon can be explained as follows. Firstly, the total energy output is determined by the sulfur loading, discharge voltage, and discharge capacity. For the simulation, all these parameters are set as the same values, resulting in the same energy output. Another important factor is T_{total} . The thickness of SSE is set constant, while the thickness of the Li anode is determined by the sulfur loading. The resultant thicknesses of the anode and SSE are basically the same in spite of the SSE options. The low ratio of SSE (26.7 wt%) in the cathode has a negligible effect on the thickness of the cathode. Overall, the volumetric energy density shows low dependency on the types of SSEs even if they have various densities.

The volumetric energy density is sensitive to the sulfur loading. As shown in Fig. 18D–F, the relationship between the volumetric energy density and sulfur loading is almost linear with a fixed SSE thickness. For instance, at a low sulfur loading of 1 mg cm⁻² and 30 μm SSEs, the volumetric energy densities of SSLSBs based on a SPE and oxide SSE are only 156 and 171 W h L⁻¹, respectively. When the sulfur loading is

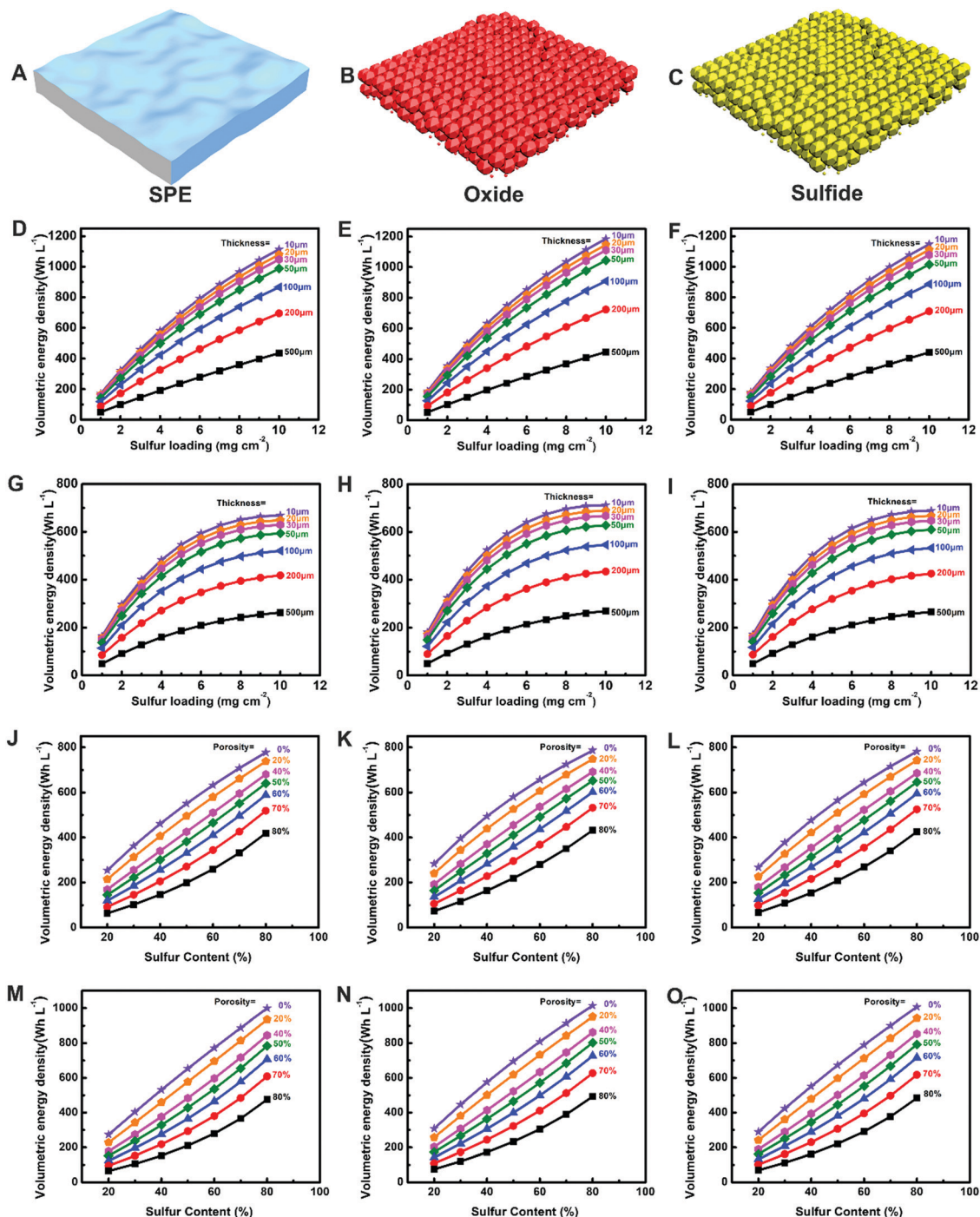


Fig. 18 Estimating the practical volumetric energy density of SSLSB with (A) SPE, (B) oxide-based and (C) sulfide-based SSEs. (D–F) Volumetric energy density calculated based on a theoretical discharge capacity of 1672 mA h g^{-1} and an average discharge voltage of 2.1 V as a function of sulfur loading for various thicknesses of SSEs. (G–I) Volumetric energy density calculated based on various theoretical discharge capacities and average discharge voltages (discharge capacity = $(1672 - 50x) \text{ mA h g}^{-1}$, average discharge voltage = $(2.1 - 0.03x) \text{ V}$, x is the sulfur loading) as a function of sulfur loading for various thicknesses of SSEs. Volumetric energy density calculated based on an optimized sulfur loading of 5 mg cm^{-2} and thicknesses of (J–L) $100 \mu\text{m}$ SSE and (M–O) $50 \mu\text{m}$ SSE as a function of sulfur content for various porosities of cathodes.

increased to 10 mg cm^{-2} , high volumetric energy densities of over 1000 W h L^{-1} (1047 and 1110 W h L^{-1}) can be achieved.

A thin SSE is another important parameter to ensure a high volumetric energy density. For example, all the SSEs with a low thickness of $30 \mu\text{m}$ can achieve a high volumetric energy

density of more than 1000 W h L^{-1} for 10 mg cm^{-2} sulfur loaded SSLSBs. The relative value will be decreased to around 850 W h L^{-1} upon increasing the thickness of SSE to $100 \mu\text{m}$. When the thickness of SSE is further increased to $500 \mu\text{m}$, only a low volumetric energy density of around 440 W h L^{-1} can be expected.

Similar to the simulation results of gravimetric energy density, the high sulfur loading and thin SSEs are equally important to volumetric energy density. Considering that the full theoretical values are overestimated based on current SSLSB performance, simulations are adjusted with more realistic parameters (Fig. 18G–I). Interestingly, rather than a volcanic curve obtained for gravimetric energy density simulation, the plots of volumetric energy density *versus* sulfur loading sharply increases at low sulfur loadings and then levels off instead. Even though a higher sulfur loading generally leads to a higher volumetric energy density, the increase in volumetric energy by sulfur loading is almost stagnant above 6 mg cm^{-2} . For example, the volumetric energy densities can be increased from 149, 156 and 163 W h L^{-1} to 516, 532 and 551 W h L^{-1} based on the increase in sulfur loading from 1 to 6 mg cm^{-2} for the SSLSBs (considering $50 \mu\text{m}$ SSEs), respectively. Further increasing the sulfur loading to 10 mg cm^{-2} leads to small increases of 77, 77 and 76 W h L^{-1} , respectively. Considering the serious Li dendrite problem and large cycling volumetric change at high sulfur loading, it is not a good idea to push the minimal increase in energy density at a high risk of SSLSB failure. Therefore, a sulfur loading around 6 mg cm^{-2} is reasonable. Meanwhile, an SSE thickness below $50 \mu\text{m}$ is necessary for achieving a volumetric energy density above 500 W h L^{-1} . As shown in eqn (3) and Table 2, we take the cathode porosity (P_{cathode}) and cathode sulfur content (ω_{S}) into serious consideration for practical volumetric energy density. The relationships between volumetric energy density and sulfur content based on different porosities of the cathode are shown in Fig. 18J–O. The simulations are based on a sulfur loading of 5 mg cm^{-2} , a theoretical discharge capacity of 1672 mA h g^{-1} , and an average discharge voltage of 2.1 V. Also, the SSE thickness is set as $100 \mu\text{m}$ for the simulations in Fig. 18J–L and $50 \mu\text{m}$ in Fig. 18M–O. Obviously, the volumetric energy density gradually increases with decreasing porosity and increasing sulfur content. At a low sulfur content of 20 wt%, the volumetric energy densities are lower than 300 W h L^{-1} under all conditions. To achieve a volumetric energy density of higher than 500 W h L^{-1} , 50 wt% and 40 wt% higher sulfur content are essential for $100 \mu\text{m}$ and $50 \mu\text{m}$ SSEs, respectively. Even though it is possible to pursue higher volumetric energy densities by increasing the sulfur content to 70 wt% or higher, the worsening Li^+/e^- transport could limit the practical performance. Hence, a sulfur content around 50 wt% is reasonable.

Table 2 Components of SSLSB soft packages for volumetric energy density simulation

Components	Thickness (μm)
Cathode current collector	16
Cathode ^a	$10x/\omega_{\text{S}}\rho_{\text{Cathode}}$
SSE ^b	t
Anode (lithium metal) ^c	$12.29x$
Total	$16 + (12.29 + 10/\omega_{\text{S}}\rho_{\text{Cathode}})x + t$

^a Areal sulfur loading is $x \text{ mg cm}^{-2}$, where the sulfur content is ω_{S} based on the whole cathode. ^b The thickness of SSE is t . ^c 50 wt% lithium excess accords to the stoichiometric ratio of sulfur.

At a sulfur content of 50 wt%, a low porosity of less than 20% is necessary for outputs above 500 W h L^{-1} . Unlike the popular high-performance porous cathodes for liquid-based Li–S batteries, the increased porosity will worsen both Li^+/e^- and volumetric energy density for SSLSBs. What's more, in the SPE-based SSLSBs, additional SSE from the SSE pallets will fill the pores to build Li^+ transport pathways, which will increase the risk of short-circuiting. After all, 15–20% porosity should be retained to alleviate the volumetric expansion during lithiation. It should be mentioned that the plots in Fig. 18J–O are calculated based on theoretical values, so the requirements on sulfur content and porosity should be more stringent for practical Li–S batteries in order to achieve a high volumetric energy density.

Fig. 19 shows the simulation results of volumetric energy densities of SSLSBs based on Hybrid-20, Hybrid-50 and Hybrid-80 SSEs. As previously discussed, the option of SSEs shows a negligible effect on the volumetric energy density. The simulation results based on the hybrid SSEs essentially reach the same conclusion and tendency as the results based on the SPE, sulfide, and oxide SSEs.

In summary, according to the above simulation results, the type of SSE shows a negligible effect on the volumetric energy density, while the volumetric energy density is sensitive to sulfur loading, SSE thickness, cathode sulfur content, and cathode porosity. Taking a comprehensive consideration of Li^+/e^- transport, volume change, and the target of 500 W h L^{-1} , practical requirements are concluded as a sulfur loading of around 6 mg cm^{-2} and a low SSE thickness of less than $50 \mu\text{m}$. Similar to the role of sulfur content played in gravimetric energy density, the reasonable sulfur content is around 50 wt%. High porosity in the cathode is detrimental to the Li^+/e^- transport and volumetric energy density, and has risks regarding safety issues. A porosity of 15–20% is ideal for alleviating the effect of volumetric expansion during lithiation without an obvious influence on volumetric energy density. For future studies, the development of SSLSBs should comprehensively consider an SSE thickness below $50 \mu\text{m}$, and high-performance sulfur cathodes with a sulfur loading of around 6 mg cm^{-2} and low porosity of 15–20% for high-volumetric-energy density SSLSBs. Of course, if the thickness of SSEs can be further decreased to less than $30 \mu\text{m}$, $4\text{--}5 \text{ mg cm}^{-2}$ sulfur loading would be sufficient to achieve the target.

3.3 Target of engineering SSLSB soft package

To achieve the targets of 500 W h kg^{-1} in gravimetric energy densities and 500 W h L^{-1} in volumetric energy densities, the following requirements should be met (Table 3).

3.4 Statistical analysis of the current research on SSLSBs

The gravimetric energy density and volumetric energy density of SSLSBs are greatly dependent on the combination of several key parameters including cathode sulfur loading, electrolyte thickness, discharge capacity output, *etc.* Hence, we summarized the statistical information from 121 publications, including 25 SPE-based SSLSBs, 22 GPE-based SSLSBs, 13 oxide SSE-based SSLSBs and 61 sulfide SSE-based SSLSBs. Considering the

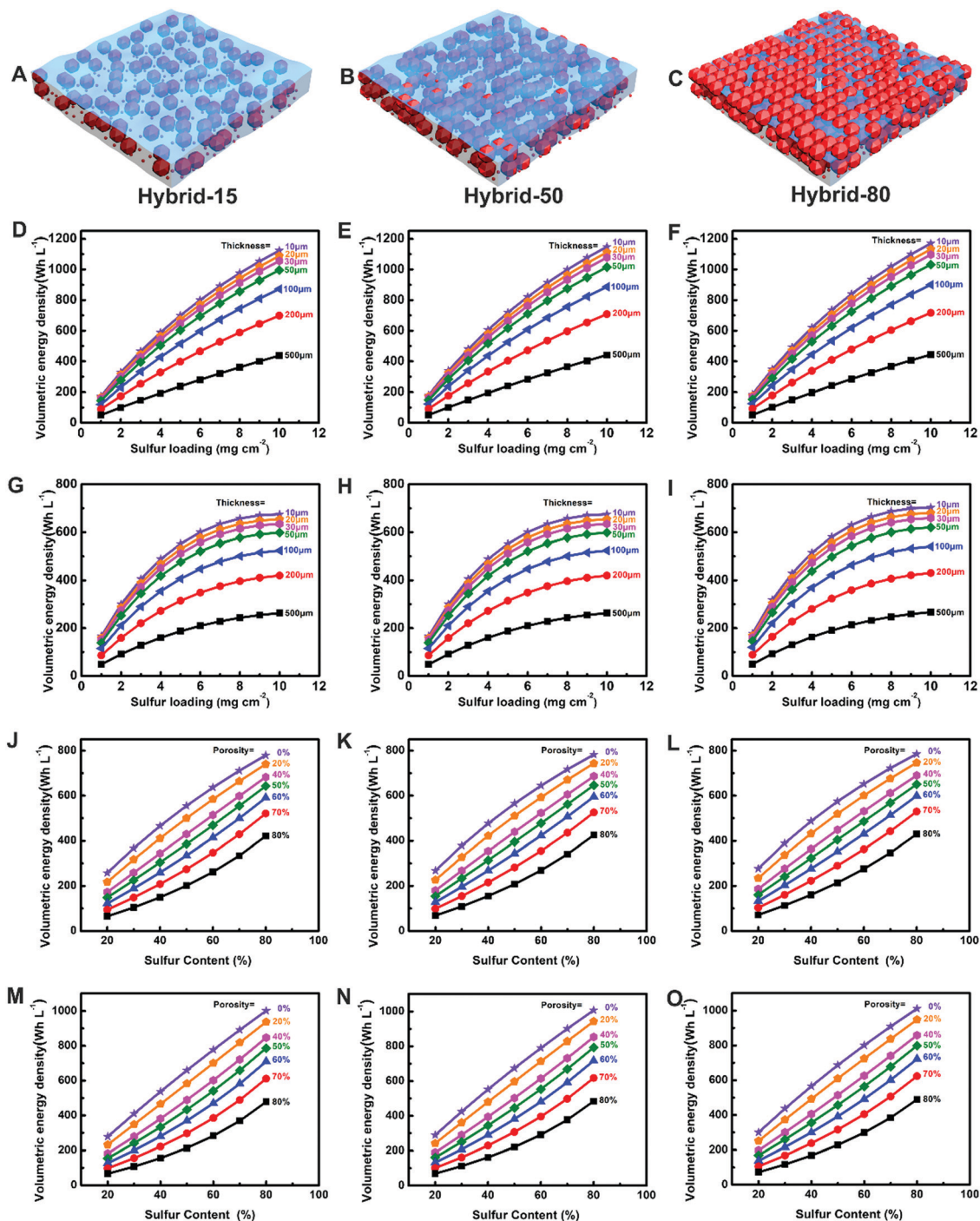


Fig. 19 Estimating the practical volumetric energy density of SSLSB with (A) Hybrid-20, (B) Hybrid-50 and (C) Hybrid-80 SSEs. (D–F) Volumetric energy density calculated based on a theoretical discharge capacity of 1672 mA h g^{-1} and an average discharge voltage of 2.1 V as a function of sulfur loading for various thicknesses of SSEs. (G–I) Volumetric energy density calculated based on various theoretical discharge capacities and average discharge voltages (discharge capacity = $(1672 - 50x) \text{ mA h g}^{-1}$, average discharge voltage = $(2.1 - 0.03x) \text{ V}$, x is the sulfur loading) as a function of sulfur loading for various thicknesses of SSEs. Volumetric energy density calculated based on an optimized sulfur loading of 5 mg cm^{-2} and thicknesses of (J–L) $100 \mu\text{m}$ SSE and (M–O) $50 \mu\text{m}$ SSE as a function of sulfur content for various porosities of cathodes.

different characteristics and different electrochemical reaction processes with different SSEs, the statistical information is separately summarized for polymer SSE (including GPE and SPE) based SSLSBs in Table 4 and Fig. 20, oxide SSE-based SSLSBs in Table 5 and Fig. 21, and sulfide SSE-based SSLSBs in Table 6 and Fig. 22.

As shown in Fig. 20A, 80.0% of the reported polymer SSE based SSLSBs used sulfur loadings less than 2 mg cm^{-2} , while only 10.0% demonstrated cathode sulfur loadings greater than 4 mg cm^{-2} . SSLSBs based on oxide and sulfide SSEs are more likely to aim for high sulfur loadings. As shown in Fig. 21A and 22A, the

Table 3 Target of high energy density SSLSBs

Parameters	Target
Sulfur content (based on the whole cathode)	~ 50 wt%
Specific capacity	≥ 1200 mA h g ⁻¹
Sulfur loading	4–6 mg cm ⁻²
SSE thickness	≤ 50 μm
Average voltage	Around 2.1 V
Cathode porosity	15–20%
% Li excess	≤ 50 wt%
Preparation and fabrication method (for both materials and systems)	Feasible and low-cost

ratios of sulfur loading less than 2 mA cm⁻² are decreased to 66.7% and 47.5%, respectively. Moreover, the ratios of high sulfur loading (> 4 mg cm⁻²) are increased to 25.0% and 20.3%, respectively. High-sulfur-loading cathodes are demonstrated to be possible in SSLSBs and shall be a focus for future studies.

Fig. 20B, 21B and 22B show the statistical information of the sulfur content in different SSE systems. It is found that only 21.5% of the sulfide SSE-based SSLSBs can achieve a relatively high sulfur content of 50 wt%, while the corresponding values are 36.8% and 70 wt% in the polymer-based and oxide SSE systems. Furthermore, it is noteworthy that the ratios of sulfur content of less than 40 wt% in polymer- and oxide SSE-based systems are 26.3% and 0% respectively, but the corresponding value in sulfide SSE-based systems is 66.1%. This can be attributed to the liquid electrolyte introduction into the oxide- and GPE-based SSLSBs (with + label in Tables 4 and 5). The presence of liquid electrolytes facilitates Li⁺ transport in the electrode and ensures wetting of the electrode/electrolyte interface, greatly reducing the ratio of SSEs in the electrodes. On the other hand, for the SPE-based SSLSBs, most of them are operated at a high temperature (*e.g.* 60 °C), where the SPEs become soft and further wet the electrode/electrolyte interface and infuse into the pores of the electrode to build Li⁺ transport pathways, thus requiring less pre-mixed SPE in the cathode. Sulfide SSE-based SSLSBs are a different case; SSEs in the cathode are necessary for Li⁺ transport even if reducing the sulfur content in the cathode. According to the above statistical information, increasing the sulfur content in sulfide SSE-based SSLSBs and reducing liquid electrolyte in GPE- and oxide SSE-based SSLSBs (for safety consideration) will be two directions in the next-step research. In SPE-based systems, the development of a high-tap-density cathode to reduce electrolyte replenishment from SPEs without sacrificing the electrochemical performance of SSLSBs is of significance. The statistical information about electrolyte thickness is shown in Fig. 20C, 21C and 22C. The electrolyte thicknesses in over 79.2% publications on polymer SSE-based SSLSBs are thinner than 100 μm. More importantly, 27.1% of them present a thickness of less than 50 μm, which can meet the requirements of SSLSBs with a high gravimetric/volumetric energy density of 500 W h kg⁻¹/500 W h L⁻¹. Considering the poor mechanical properties of polymer SSEs, whether it can effectively suppress Li dendrites when combined with high sulfur loading cathodes should be further evaluated. In contrast, 69.3% of oxide SSEs and 96.2% sulfide SSEs in SSLSBs are greater than 200 μm, which is

considered to lower the gravimetric/volumetric energy density to values less than 300 W h kg⁻¹/400 W h L⁻¹ according to our simulations. The good news is that 15.3% of oxide SSEs with thicknesses less than 50 μm can be realized by the tape casting technique.^{43,185,186} Besides, the hot-pressing and cold-pressing techniques have demonstrated their potential to press the sulfide SSEs into a substrate or fabricate a free-standing sulfide SSE pallet with thicknesses around or less than 100 μm.^{294,295} Nevertheless, fabricating ultra-thin oxide SSEs and sulfide SSEs is still a big challenge. It is urgent to accelerate the development of ultra-thin electrolyte preparation technologies.

Fig. 20D, 21D and 22D show the statistical information of the observed discharge voltages. Since 89.5% and 78.5% of the publications on polymer and oxide SSE-based SSLSBs present average discharge voltage plateaus over 2.0 V, electrochemical feasibility is demonstrated. However, only 18.2% of the publications about sulfide SSE-based SSLSBs show average discharge voltage plateaus over 2.0 V, while 68.2% of them are lower than 1.5 V. The reasons for such a huge difference in discharge voltage can be attributed to the anode materials applied in SSLSBs. As shown in Fig. 20E, 21E and 22E, the anode materials used in polymer and oxide SSE-based SSLSBs are almost Li metal, while only 1/3 of the sulfide SSE based SSLSBs use a Li metal anode. Alternative anode materials of In and Li–M alloys (*e.g.* Li–Ge, Li–In) usually possess a higher potential (such as 0.6 V *vs.* Li for In and Li–In alloy), resulting in an overall lower discharge voltage in sulfide SSE-based systems. The In and Li–M alloys are sometimes chosen because of higher stability against sulfide SSEs and because they are free of Li dendrites. In order to take advantage of the high-capacity Li metal anode, the development of effective Li protection for both Li dendrite suppression and Li/SSE interfacial reaction protection is of importance and urgency to pave the way for practical sulfide SSE based SSLSBs.

Current density, a parameter related to rate performance and power density, is summarized. Power density is an important indicator to evaluate the SSLSBs for suitable charging time. As shown in Fig. 20F, 21F and 22F, over 50% of the SSLSBs in the publications are operated at current densities of less than 0.2 mA cm⁻², corresponding to a low C-rate of 0.02–0.03C for an optimized sulfur loading of 4–6 mg cm⁻². In other words, each charging process will take 23–35 h based on 70% sulfur utilization (~1200 mA h g⁻¹). This is far below the expectation for practical applications. In practical settings, a C-rate of at least 0.2C (equaling a current density of 1.3–2 mA cm⁻²) is required. According to the statistical information, the ratios of higher than 1 mA cm⁻² in polymer-, oxide-, and sulfide-based SSLSBs are 23.1%, 16.7% and 17.7%, respectively. Optimization of the SSLSB components, enhancement of the Li⁺/e⁻ transport in the electrode, and improvement of the ionic conductivity of SSEs are necessary to further improve the rate performance of SSLSBs.

The discharge capacities, as another critical parameter, are summarized in Fig. 20G and 21G, in which only 17.0% and 21.4% of the polymer- and oxide SSE-based SSLSBs delivered initial discharge capacities greater than 1200 mA h g⁻¹. This is far from that required for high-energy-density SSLSBs.

Table 4 Summary of polymer SSE-based SSLSBs (the values in brackets in the active material content and areal capacity columns are the accurate values in the articles; the average values are used for statistical information analysis. “+” in the electrolyte column means a liquid component is involved. The values in brackets in the thickness column are the SSE weights provided by the articles and the thicknesses are calculated based on the densities of SSE and surface areas of model cells. The values inside/outside brackets in the discharge capacity and areal capacity columns are the capacities after/before cycling. The values and materials in brackets in the current density and voltage plateau discharge columns are the operating temperatures and anode materials. If there is no operating temperature information in the column of current density, the cells are operated at RT or 25 °C)

Cathode	SSE		Performance						
	Active material content (wt%)	Areal loading (mg cm ⁻²)	Thickness (μm)	Discharge capacity (mA h g ⁻¹)	Cycles	Current density (mA cm ⁻²)	Voltage plateau discharge (V)	Areal capacity (mA h cm ⁻²)	Ref.
PAN-S	~20	—	80 (70–90 in article)	815 (380)	40	0.2 (70 °C)	2.0 (Li)	—	149
Li ₂ S-C	35	—	—	600 (600)	27	— (30 mA g ⁻¹ in the article, 70 °C)	2.1 (Li)	—	302
S-C@PANI	43	0.8	60	640 (538)	1000	0.67 (60 °C)	2.1 (Li)	0.51 (0.45)	171
S-KB	35	—	~120	375 (175)	50	— (0.05C in the article, 70 °C)	2.0 (Li)	—	167
S-Super P	30	—	260	1400 (864)	100	—	1.8 (Li)	—	168
S-Super P	30	—	260	1110 (400)	1000	—	1.8 (Li)	—	168
S-CMK-3	46	1.0	150	310 (310)	500	0.84 (60 °C)	1.8 (Li)	0.31 (0.31)	146
S-KB	40	1.05 (1.0–1.1)	60	600 (150)	1380	0.50 (70 °C)	2.1 (Li)	0.63 (0.16)	303
S-C	16	0.3 (0.2–0.4)	65 (50–80)	900 (800)	70	0.17 (70 °C)	2.0 (Li)	0.27 (0.24)	304
S-KB	40	0.95 (0.9–1.0)	50	1050 (900)	30	0.16 (70 °C)	2.0 (Li)	1.00 (0.86)	23
S-KB	40	0.95 (0.9–1.0)	100	600 (500)	50	0.16	2.0 (Li)	0.57 (0.48)	177
S-KB	40	0.8	—	625 (625)	50	0.13	2.1 (Li)	0.5 (0.5)	166
S-KB	12	0.2	16	970 (720)	100	0.04	2.0 (Li)	0.19 (0.14)	24
S-C@PANI	30	0.8	130	1350 (745)	100	0.13	1.8 (Li)	1.08 (0.60)	38
S-N-CNS	70	1.2	25 (20–30)	805 (600)	80	— (37 °C)	2.0 (Li)	0.97 (0.72)	37
S-LLZO-C	64	0.77	48 (20–75)	1040 (900)	200	0.05 (37 °C)	2.0 (Li)	0.80 (0.69)	39
S-Super P	48	1.85 (1.7–2.0)	50	918 (459)	40	0.15	2.1 (Li)	1.70 (0.85)	20
GO-PEG@C/S	42	0.8	60	1457 (793)	50	1.34 (80 °C)	2.0 (Li)	0.56 (0.49)	67
S-C	60	0.7	120	650 (470)	80	4.18	2.0 (Li)	1.63 (1.17)	305
S-CNT	40	2.5 (2.0–3.0)	50	1500 (800)	60	0.17	2.1 (Li)	1.5 (0.8)	25
S-KB	40	1.0 (0.9–1.1)	80	800 (800)	50	0.08 (60 °C)	1.9 (Li)	0.40 (0.40)	306
S-MgAl ₂ O ₄ -graphene	56	0.5	—	—	—	—	—	—	—
S-AB	40	0.5	70	1016 (1000)	40	0.08 (60 °C)	2.0 (Li)	0.51 (0.50)	69
S-KB	40	0.95 (0.8–1.1)	50	900 (800)	30	0.16 (70 °C)	2.1 (Li)	0.86 (0.76)	70
S-CNF	—	1.27	15	390 (415)	50	0.084	2.1 (Li)	0.50 (0.53)	307
PAN@C-S	30	0.37	90	1306 (680)	200	0.12	2.0 (Li)	0.48 (0.25)	278
PAN@C-S	30	1.2	90	925 (1261)	10	0.2	2.0 (Li)	1.1 (1.5)	278
S-CMK-3	60	1.65 (1.5–1.8)	30	988 (792)	500	0.83	2.1 (Li)	1.63 (1.31)	22
S-C	70	0.85	25	1519 (928)	150	2.84	2.0 (Li)	1.29 (0.79)	163
S-PPy	34	1.0	20	1174 (523)	300	1.00	2.0 (Li)	1.17 (0.52)	145
S-Super P	60	1.35 (1.2–1.5)	—	647 (530)	400	1.13	1.9 (Li)	0.87 (0.72)	21
S-rGO	82	1.7	20	1100 (847)	500	2.84	2.1 (Li)	1.87 (1.44)	159
S-rGO	82	5.2	20	879 (809)	60	2.84	2.1 (Li)	4.57 (4.21)	159
S-BP2000	49	1.15 (1–1.3)	100	1215 (869)	200	0.19	2.1 (Li)	1.40 (1.00)	157
S-CNT	2.8	2.8	~400	1050 (800)	50	0.5	2.0 (Li)	2.94 (2.24)	308
S-CNT	67.5	4.9	~400	850 (700)	50	0.5	2.0 (Li)	4.17 (2.80)	308
S-graphene-CNT	51	2.65	—	1033 (833)	200	0.44	2.1 (Li)	2.74 (2.21)	26
S-C	21	—	60	1467 (1267)	25	0.3	1.8 (Li)	—	148
Li ₂ S-C	35	—	80	1200 (900)	33	0.11	2.0 (Sn-C)	—	309
S-KB	53	2.65	80	750 (600)	40	0.34	2.0 (Li)	1.99 (1.59)	197
S-KB	64	1.15	80	700 (582)	50	0.11	2.1 (Li)	0.81 (0.67)	162
S-CNF	61	—	—	1150 (820)	100	—	—	—	158

Table 4 (continued)

Cathode	SSE		Performance						
	Active material content (wt%)	Areal loading (mg cm^{-2})	Thickness (μm)	Discharge capacity (mA h g^{-1})	Cycles	Current density (mA cm^{-2})	Voltage plateau discharge (V)	Areal capacity (mA h cm^{-2})	Ref.
S-C	75	1.2		1050 (670)	250	— (0.1C in the article)	2.0 (Li)	1.26 (0.80)	310
S-C	75	4.1		1020 (800)	100	0.20	2.0 (Li)	4.18 (3.28)	310
S@graphene	49	1.0 (0.8-1.2)	MH-Qes (+)	1383 (981)	200	0.68	2.1 (Li)	1.38 (0.98)	311
S@C	54	1.15 (1.0-1.3)	PVDF-Mg-MOF-74 GPE (+)	904 (714)	100	0.17	2.0 (Li)	1.04 (0.82)	312
S@Super P	48	1.2	PA-LATP + PAN-PEO-LATP GPE (+)	601 (405)	300	0.19	— (Li)	0.72 (0.49)	313
S@Super P	48	5.0	PVDF-HFP/PETT-ester GPE (+)	720 (350)	200	1.67	— (Li)	3.60 (1.75)	313
S@CNT	48	1.15 (1-1.3)	PVDF-HFP/PETT-ester GPE (+)	995 (600)	200	1.92	2.1 (Li)	1.14 (0.69)	314
S@CNT	54	2.5	C@PMMA GPE (+)	720 (715)	100	2.09	2.0 (Li)	1.80 (1.79)	315
S@TiO ₂	33	—	PEGDA-PEI GPE (+)	1160 (313)	66	— (0.15C in the article)	1.8 (Li)	—	316
S@C	36	0.5	TEGDME-ETPTA-Al ₂ O ₃ GPE (+)	1100 (680)	200	0.25	2.0 (Li)	0.55 (0.34)	317
S@rGO@CNT	65	4.41	PEGDA-P(BA-co-[EVIm]TFSI) QPE-IL (+)	1179 (850)	200	3.69	2.1 (Li)	5.20 (3.75)	318

The shuttle-free sulfide SSE based SSLSBs generally demonstrating a better performance with 36.4% can achieve a high discharge capacity of over 1200 mA h g^{-1} , as shown in Fig. 22G. Notably, 9.1% of them delivered capacities beyond the theoretical value of 1672 mA h g^{-1} . According to recent publications, the excess capacities are contributed by the reduction of SSEs.^{129,130,296-300} Technically, reversible interfacial behaviors should be distinguished from the irreversible decomposition of SSEs. Nevertheless, the statistical information shows that the shuttle-free sulfide SSE-based SSLSBs are advantageous in terms of capacity and sulfur utilization.

For SSLSBs aiming to supply power/energy to portable electronic devices and electric vehicles, long cycle lives affording thousands of stable charge/discharge are required. Fig. 20I, 21I and 22I summarize the cycle lives for polymer-, oxide- and sulfide-based SSLSBs, but only 32.2%, 21.4% and 24.2% of them demonstrated long cycle lives of over 200 cycles. After cycling, only 3.4% of the polymer-based SSLSBs and 7.1% of the oxide SSE based SSLSBs maintained discharge capacities of over 1200 mA h g^{-1} . The poor cycling stability often resulted from the presence of LiPs (Fig. 20H and 21H). In the shuttle-free sulfide SSE systems, the relative value is 16.6%, which is much better than those of the polymer- and oxide SSE-based SSLSBs (Fig. 22H), further highlighting the merits of shuttle-free SSLSBs. Moreover, some reported shuttle-free sulfide SSE-based SSLSBs show amazing electrochemical performance. For instance, with a S-activated carbon (AC) cathode and Li_{1.5}PS_{3.3} SSE, the SSLSBs with a sulfur loading of 1.5 mg cm^{-2} showed excellent cycling stability with a high discharge capacity of 1800 mA h g^{-1} over 1000 cycles. Further increasing the sulfur loading to 6.1 mg cm^{-2} and 9.3 mg cm^{-2} , the SSLSBs can also deliver high discharge capacities of 1620 mA h g^{-1} and 1400 mA h g^{-1} for 500 cycles and 200 cycles, respectively.³⁰¹ Overall, the cycle life and discharge capacity should be further improved, especially for the LiPS involved polymer and oxide SSE-based SSLSBs.

Areal capacity can be a more comprehensive indicator that accounts for both discharge capacity and sulfur loading. According to the target of $500 \text{ W h kg}^{-1}/500 \text{ W h L}^{-1}$ for SSLSBs discussed in Section 3.3, a high discharge capacity of 1200 mA h g^{-1} and an optimized sulfur loading of $4-6 \text{ mg cm}^{-2}$ are essential to achieve the target gravimetric/volumetric energy densities. Therefore, a high areal capacity of $4.8-7.2 \text{ mA h cm}^{-2}$ is required. Here we choose a median value of 6 mA h cm^{-2} for the following discussion. As shown in Fig. 20J, 21J and 22J, 0%, 8.3%, and 10.2% of polymer-, oxide- and sulfide SSE-based SSLSBs can achieve a high areal capacity of over 6 mA h cm^{-2} . After cycling, the corresponding fractions are further decreased to 0%, 0% and 8.5%, respectively (Fig. 20K, 21K and 22K). Similar to the statistical information of discharge capacity, shuttle-free sulfide SSE-based SSLSBs exhibit better results compared with polymer and oxide SSEs. However, it is still a long way for the practical application of SSLSBs.

Considering all the discussed statistics, the spider plots in Fig. 20L, 21L and 22L outline the contribution of each factor. As a brief conclusion, the sulfur loading and cycle life are the

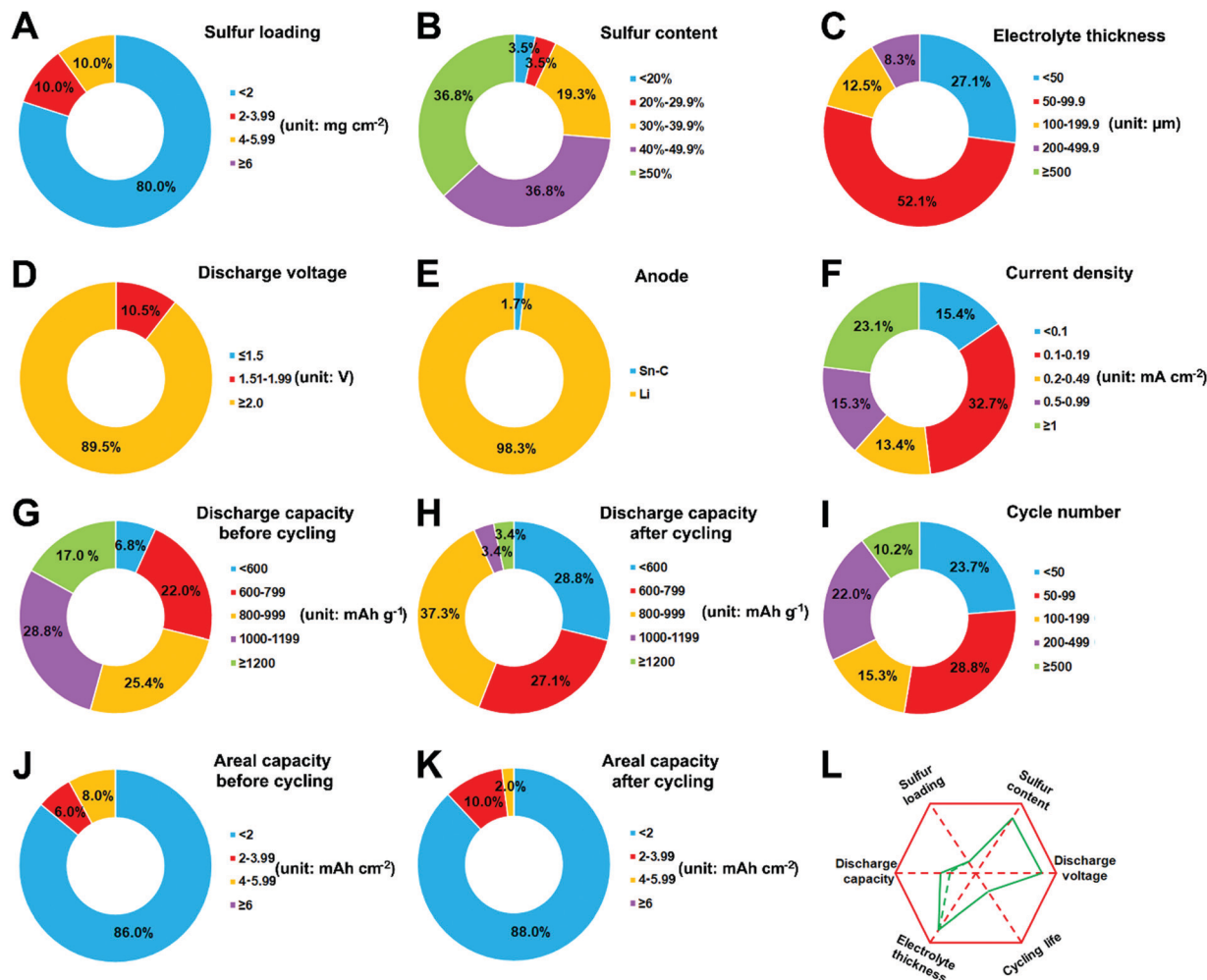


Fig. 20 Statistical analysis of polymer SSE-based SSLSBs. (A) Sulfur loading, (B) sulfur content, (C) electrolyte thickness, (D) discharge voltage, (E) anode, (F) current density, (G) discharge capacity before cycling, (H) discharge capacity after cycling, (I) cycle number, (J) areal capacity before cycling, and (K) areal capacity after cycling. Spider chart (L) displaying the state of polymer SSE-based SSLSBs.

drawbacks of all three types of SSLSB. Benefitting from the shuttle-free property, the sulfide SSE-based SSLSBs present higher discharge capacity and capacity retention compared with polymer and oxide SSE-based SSLSBs. The polymer and oxide SSE based SSLSBs exhibit higher sulfur contents and discharge voltages due to the high flowability and wettability of SPE/liquid electrolytes and wide use of Li metal anodes. Further increasing the sulfur content in the cathode and improving Li metal anode viability are the two important directions for sulfide SSE based SSLSBs. The electrolyte thickness of polymer SSEs can generally meet the demand of high-energy-density SSLSBs, while ultra-thin SSE fabrication technologies should be urgently developed in ceramic SSE-based SSLSBs.

4. Conclusions and perspectives

The pursuit of high safety and high energy density urges the development of SSLSBs for energy storage, especially for applications in portable electronic devices and electric vehicles.

However, the practical application of SSLSBs is still hindered by major challenges such as LiPS shuttling, interfacial issues, Li dendrite growth as well as mismatched parameters between fundamental research and practical application. As shown in Fig. 23, an ideal high-energy-density SSLSB should feature a dendrite-free Li anode, good interfacial contact, shuttle-free electrochemical process, as well as the fulfillment of engineering requirements. According to our simulations for engineering pouch cells, the realization of SSLSBs with high gravimetric/volumetric energy densities of $500 \text{ W h kg}^{-1}/500 \text{ W h L}^{-1}$ should meet several requirements including high areal sulfur loadings ($4\text{--}6 \text{ mg cm}^{-2}$), high sulfur content ($\sim 50 \text{ wt}\%$ based on the whole cathode layer), low electrolyte thickness ($< 50 \mu\text{m}$), high specific capacities ($> 1200 \text{ mA h g}^{-1}$), high average discharge voltage ($\sim 2.1 \text{ V}$), low electrode porosity ($15\text{--}20\%$), and low Li excess ($\leq 50 \text{ wt}\%$). In addition to the often unregulated Li excess and electrode porosity in research, the statistical information collected from 121 publications related to SSLSBs showed that the sulfur loading and cycling life are the main shortcomings for SSLSBs no matter based on

Table 5 Summary of oxide SSE-based SSLSBs (the values in brackets in the active material content and areal capacity columns are the accurate values in the articles; the average values are used for statistical information analysis. "+" in the electrolyte column means a liquid component is involved. The values in brackets in the thickness column are the SSE weights provided by the articles and the thicknesses are calculated based on the densities of SSE and surface areas of model cells. The values inside/outside brackets in the discharge capacity and areal capacity columns are the capacities after/before cycling. The values and materials in brackets in the current density and voltage plateau discharge columns are the operating temperatures and anode materials. If there is no operating temperature information in the column of current density, the cells are operated at RT or 25 °C)

Cathode		SSE		Performance						
Active material	Active material content (wt%)	Areal loading (mg cm ⁻²)	SSE	Thickness (μm)	Discharge capacity (mA h g ⁻¹)	Cycles	Current density (mA cm ⁻²)	Voltage plateau discharge (V)	Areal capacity (mA h cm ⁻²)	Ref.
S-KB	48	—	LATP (+)	650	1400 (720)	40	— (0.2C)	2.1 (Li)	—	181
S-C	59	1.78	LATP (+)	150	900 (900)	15	0.15	2.1 (Li)	1.60 (1.60)	44
Li ₂ S ₆ -CNF-AC	54	4.0	LATP (+)	350	1000 (450)	300	2.2	1.8 (Li)	4.00 (1.80)	182
Li ₂ S ₆	—	—	LATP (+)	300	978 (720)	50	— (0.1C in the article)	2.0 (Li)	—	184
Li ₂ S ₆ -CNF	50	2.0	LYZP (+)	150	1000 (900)	150	0.67	2.0 (Li)	2.00 (1.80)	41
S-CNT	—	7.5	LLCZN-bilayers (+)	35	645 (500)	32	0.2	2 (Li)	4.84 (3.75)	43
S-KB	48	1	LAMP (+)	—	915 (668)	1200	1.67	1.9 (Li)	0.92 (0.67)	183
S-CNT	68	0.04	LAMP (+)	800	1510 (1400)	30	0	2.1 (Li)	0.06 (0.06)	40
Li ₂ S ₈ -carbon sponge	—	1.2	LLZGN (+)	200	1050 (1050)	60	0.1	2.1 (Li)	1.26 (1.26)	42
S-KB	52	0.8 (0.6-1.0)	PEO-LATP-PEO	500	1035 (823)	100	0.13 (60 °C)	2.0 (Li)	0.83 (0.66)	147
S-C	80	0.6	LLZTO (+)	300	570 (480)	50	0.02	1.9 (Li)	0.34 (0.29)	319
S-C	80	1.6	LLZTO (+)	300	381 (320)	15	0.12	2.0 (Li)	0.61 (0.51)	319
S-CNT	—	5.4	LLZTO-trilayers (+)	15	1200 (1100)	50	0.27	2.1 (Li)	6.48 (5.94)	185
S@AB	48	1.4	LAMP-PP (+)	200	1050 (819)	200	0.47	2.0 (Li)	1.47 (1.15)	320

oxide, sulfide, or polymer SSEs. More specifically, the limited sulfur content and low discharge voltage, and thick SSEs also limit the practical application of sulfide SSE-based SSLSBs; the practical application of polymer- and oxide SSE-based SSLSBs is hindered by the low capacity output and capacity retention because of LiPS dissolution in the liquid or polymer phase. Solving these problems or minimizing their effect is critical to paving the way for large-scale SSLSB engineering. Suggestions to solve the above challenges and propel the development of high-energy-density SSLSBs are listed below.

(1) Cathode

To achieve high gravimetric and volumetric energy densities, designing cathodes with high loading, high sulfur content, high capacity output, low porosity, and long cycling life is of significance. High-sulfur-loading cathodes can be easily realized by increasing the thickness of the cathode. However, thick electrodes are often accompanied by low specific capacities. It is known that electrochemical reactions occur at the tri-phase interfaces of active materials, Li⁺ conductors, and electronic conductors. Electronic conduction in cathodes (from current collector to active materials) can be facilitated by encapsulating sulfur into a nanoporous host.^{341,342} Novel conductive hosts need to be designed with high electronic conductivity and Li⁺ conducting channels for SSEs. The introduction of a small amount of high electronic conductive elements (*e.g.* Se and Te) into the cathode is a promising option to enhance electronic transport without significantly lowering the energy density.

Compared to the construction of electron pathways, rational designs with continuous Li⁺ transporting channels in the cathode and connection to the tri-phase interface still fall short at the current stage of research. An ideal structure can be a thin coating of highly ionic conductive SSE integrated with S/C composites. This can be achieved by either coating a thin layer on the surface of the S/C cathode or infusing an SSE solution or precursors into the cathode pores followed by retrieval of the SSE property. Either approach puts forward high requirements for the solubility and phase formation temperature. Developing high solubility SSEs with low phase formation temperatures may be a promising direction. Meanwhile, optimization of the cathode structure is nonetheless beneficial for increasing the sulfur content and overall capacity output.

The LiPS shuttling effect occurring in the polymer and liquid electrolyte phases is another main reason for the limited capacity output and low sulfur utilization. The introduction of functional additives and development of single-ion conductors are proved helpful for suppressing the LiPS shuttles and demonstrated to be effective for improving the cycling life of SSLSBs. Nevertheless, LiPSs still participate in the electrochemical process of these systems and pose a risk of shuttle effects. Therefore, the exploration of a LiPS-insoluble SPE system for individual use or interfacial modification of the oxide SSE/cathode interface is an interesting direction.

Externally applied pressure showed a positive effect on improving cycling performance by alleviating the negative influence of volume change of electrodes during cycling. However, it should be noted that the external pressures applied to

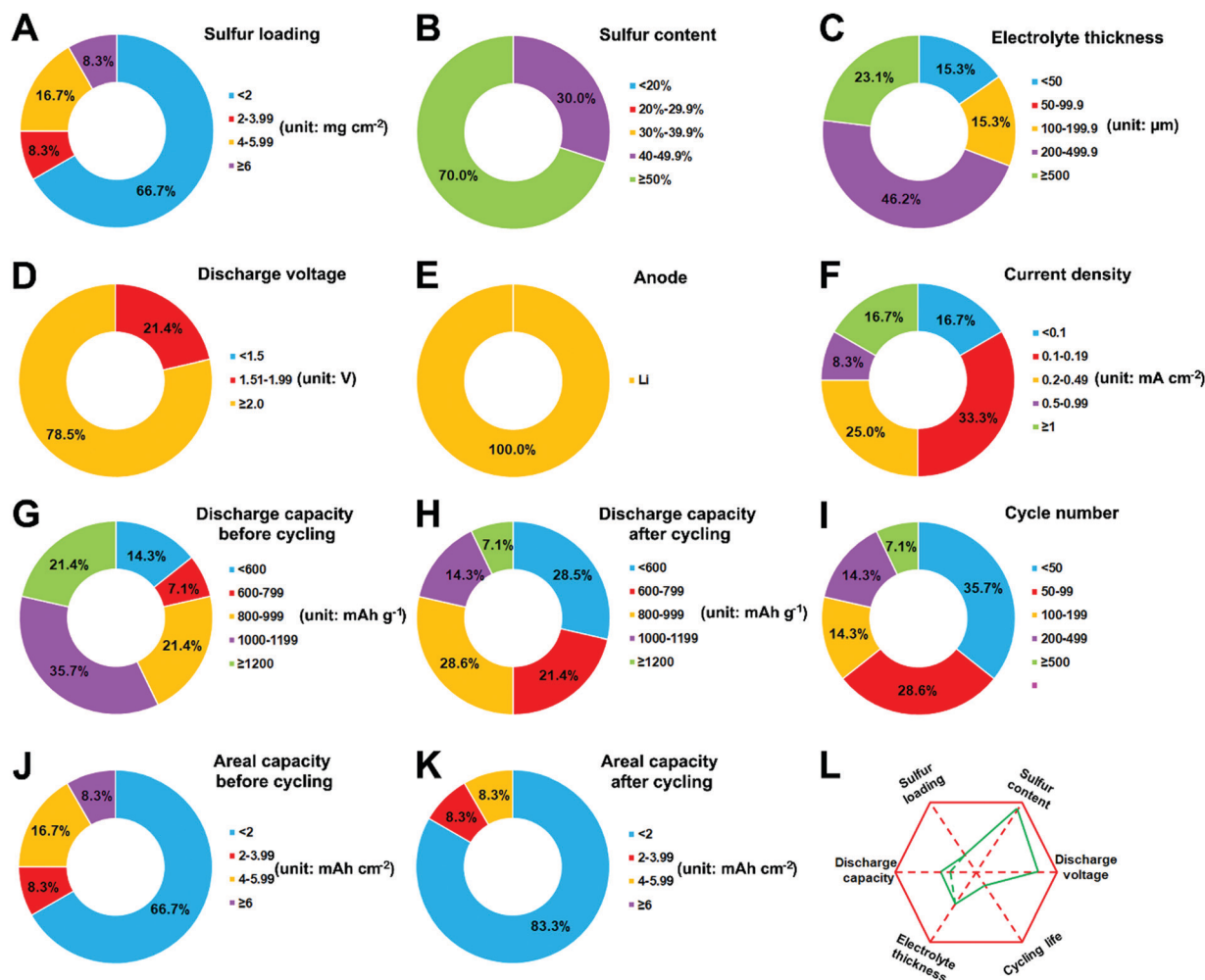


Fig. 21 Statistical analysis of oxide SSE-based SSLSBs. (A) Sulfur loading, (B) sulfur content, (C) electrolyte thickness, (D) discharge voltage, (E) anode, (F) current density, (G) discharge capacity before cycling, (H) discharge capacity after cycling, (I) cycle number, (J) areal capacity before cycling, and (K) areal capacity after cycling. Spider chart (L) displaying the state of oxide SSE-based SSLSBs.

the model cells are over several tons. It is very difficult to exert such high pressures on the SSLSB pouch cells. Taking both electrode volume change and volumetric energy density into consideration, it is reasonable to maintain a low porosity of 15–20% in the cathode for cathode design. Smart package designs with a feasible pressure on the pouch cell would be helpful.

(2) Electrolyte

In SSLSBs, the SSE acts as a separator as well as a Li⁺ conductor. An ideal SSE should meet the requirements of (1) high ionic conductivity over a wide temperature range to realize all-climate SSLSBs, (2) high chemical stability against both cathode materials and anode materials, (3) high stability in air and moisture (can be fabricated in a dry room), (4) enough mechanical strength to suppress the Li dendrites, (5) high flexibility and processability, and (6) resistance to LiPS shuttling in the solid–liquid dual-phase reaction SSLSB systems.

SPEs based on PEO and PAN exhibit high flexibility, high air/moisture-stability, high chemical and electrochemical stabilities in the required voltage window, and ease of processing

for a thin film of less than 100 μm. However, the low ionic conductivity (typically less than 10⁻⁶ S cm⁻¹ at RT), LiPS shuttling issue, and the low mechanical strength at the operating temperatures (*e.g.* 60 °C) are the main drawbacks to be tackled. To improve the ionic conductivity, exploring SPEs with high Li⁺ transference numbers is one direction. The incorporation of small molecular additives, such as SN, to improve the ionic conductivity is another choice. Fabrication of SPEs using low molecular polymers with high stability and subsequent infusion into a porous substrate (*e.g.* commercial PP/PE membranes) can be explored in the future. Additionally, a LiPS-insoluble SPE system may be an ideal strategy to solve the shuttle effect. As for enhancement of mechanical strength, cross-linking and introduction of inorganic fillers are the two main reported approaches. However, it is very hard to have an SPE with high enough Young's modulus to mechanically suppress Li dendrites. It would be more reasonable to regulate the Li⁺ distribution for a dendrite-free plating/stripping process.

For oxide- and sulfide-based SSEs, the ionic conductivity can reach as high as over 10⁻³ S cm⁻¹, which is sufficient for SSLSB operation at RT. However, due to the rigid property of oxide

Table 6 Summary of sulfide SSE-based SSLSBs (the values in brackets in the active material content and areal capacity columns are the accurate values in the articles; the average values are used for statistical information analysis. "+" in the electrolyte column means a liquid component is involved. The values in brackets in the thickness column are the SSE weights provided by the articles and the thicknesses are calculated based on the densities of SSE and surface areas of model cells. The values inside/outside brackets in the discharge capacity and areal capacity columns are the capacities after/before cycling. The values and materials in brackets in the current density and voltage plateau discharge columns are the operating temperatures and anode materials. If there is no operating temperature information in the column of current density, the cells are operated at RT or 25 °C)

Cathode	SSE		Performance						
	Active material content (wt%)	Areal loading (mg cm ⁻²)	Thickness (μm)	Discharge capacity (mA h g ⁻¹)	Cycles	Current density (mA cm ⁻²)	Voltage plateau discharge (V)	Areal capacity (mA h cm ⁻²)	Ref.
S-Cu	15	1.91	545 (80 mg)	650 (650)	20	0.064	1.5 (Li-In)	1.24 (1.24)	33
S-Cu	27	—	—	980 (980)	5	0.064	1.4 (Li-Ge)	—	62
Li ₂ S-Cu	29	3.6	545 (80 mg)	500 (350)	20	0.064	1.5 (In)	1.8 (1.26)	321
S-C	25	—	—	1200 (853)	200	1.3	1.5 (Li-In)	—	61
S-C	35	~1.3	—	1400 (1000)	20	0.064	2.0 (Li)	1.82 (1.3)	322
Li ₂ S-C	25	3.2	545 (80 mg)	700 (700)	10	0.064	1.5 (In)	2.24 (2.24)	64
Li ₃ PS ₄ coated Li ₂ S	65	0.35 (0.2-0.5)	681 (100 mg)	1000 (500)	100	0.02 (60 °C)	2.0 (Li)	0.35 (0.18)	58
Li ₃ PS ₄	60	0.43 (0.25-0.60)	500	1200 (600)	300	0.015	2.0 (Li)	0.52 (0.26)	60
S-C	50	2	—	1087 (1050)	50	0.064	1.5 (Li-In)	2.17 (2.10)	193
S-CMK-3	15	0.96	435 (70 mg)	3239 (1000)	30	0.13	1.5 (Li-Al)	3.11 (0.96)	201
FeS + S	31	~1.2	806 (200 mg)	1762 (900)	225	0.11 (60 °C)	1.9 (Li)	2.11 (1.08)	323
S-C	30 (20-40)	2.26	300	1355 (1100)	50	0.28	1.2 (Li-In)	3.52 (2.49)	324
S-VGCF	30	4.3	—	1320 (1200)	50	0.1	1.5 (Li ₄ Si)	5.68 (5.16)	188
S-KB	50	3.75	477 (70 mg)	1320 (1200)	50	1.3	1.4 (Li-In)	4.95 (4.50)	191
S-C	60	3.78	435 (70 mg)	1280 (1217)	10	1.6	1.4 (Li-In)	4.84 (4.60)	325
a-TiS ₂ /TiS ₂	73	9.3	477 (70 mg)	312 (240)	75	0.51 (50 °C)	1.5 (In)	2.90 (2.23)	326
S-CNF	30	0.75	403 (100 mg)	1600 (1400)	10	0.063	2.0 (Li)	1.20 (1.05)	59
a-MoO ₃	40	5.1	545 (80 mg)	760 (670)	60	0.064	1.5 (Li-In)	3.88 (3.42)	122
Li ₂ S-Li-VGCF	40	2.3 (2.0-2.5)	409 (60 mg)	930 (930)	50	0.13	1.5 (Li-In)	2.14 (2.14)	327
Li ₂ S-AB	25	3.2	545 (80 mg)	620 (620)	10	0.064	1.5 (Li-In)	1.98 (1.98)	29
Li ₂ S-Li ₆ PS ₅ Cl-C	36	3.6	605 (150 mg)	648 (830)	60	0.14	1.2 (Li-In)	2.33 (2.99)	32
TiS ₂	30	3.82	621 (100 mg)	200 (170)	40	0.88	1.5 (Li-In)	0.76 (0.48)	328
S-AC	50	1.5	—	1860 (1800)	1000	1.3	1.3 (Li-In)	2.79 (2.70)	301
S-AC	50	6.1	—	1620 (1620)	500	1.3	1.3 (Li-In)	9.88 (9.88)	301
S-AC	50	9.3	—	1520 (1400)	200	1.3	1.3 (Li-In)	14.14 (13.02)	301
Co ₉ S ₈ -Li ₇ P ₃ S ₁₁	35	~1.2	1000	500 (421)	1000	1.27	1.5 (Li)	0.60 (0.51)	119
Li ₂ S-C	40	6.1	600 (88 mg)	634 (300)	37	0.064	1.3 (In)	3.87 (1.83)	36
S-C	20	3.1	600 (88 mg)	1459 (389)	20	0.064	1.4 (Li-In)	4.52 (1.21)	189
S-AB	25	1.59	435 (70 mg)	1200 (800)	40	0.13	1.5 (Li-In)	1.91 (1.27)	28
Li ₂ S	30	1.33	800	811 (464)	9	0.044	1.4 (Li-In)	1.08 (0.62)	329
S-KB-P ₂ S ₅	50	1.91	—	1288 (1288)	1	0.64	1.1 (Li-In)	2.46 (2.46)	34
S/rgO	36	0.6	—	969 (827)	60	0.05	1.8 (Li)	0.58 (0.50)	85
S	45	—	—	792 (800)	60	— (0.05C in the article)	1.8 (Li)	—	187
S-AB	30	—	360	1020 (500)	30	— (0.05C in the article)	1.8 (Li)	—	53
rgO@S	12	0.45 (0.4-0.5)	1000	930 (830)	750	0.75 (60 °C)	1.8 (Li)	0.42 (0.37)	31
S-AB	25	26.0	430	790 (560)	6	0.13	1.6 (Li ₄ Si)	20.54 (14.56)	30
Li ₂ S-VGCF	29	2.2	401 (150 mg)	469 (600)	20	0.05	1.4 (Li-In)	1.03 (1.32)	27
Li ₂ S-VGCF	30	—	—	429 (454)	20	0.064	1.3 (In)	—	330
Fe-S-VGCF (Fe/S = 1/3)	50	3.2	545 (80 mg)	520 (458)	200	0.64	1.4 (Li-In)	1.74 (1.47)	121
S-AB	25	0.6	435 (70 mg)	1150 (600)	30	0.13	1.4 (Li-In)	1.84 (0.96)	192
S-CR	9	0.6	435 (70 mg)	2100 (1500)	50	0.50	1.0 (Li-In)	1.26 (0.90)	208
S-CNT	24	1.1	615 (130 mg)	1850 (1393)	50	0.17	1.5 (Li-In)	2.04 (1.53)	35

Table 6 (continued)

Cathode	SSE		Performance						
	Active material content (wt%)	Areal loading (mg cm ⁻²)	Thickness (μm)	Discharge capacity (mA h g ⁻¹)	Cycles	Current density (mA cm ⁻²)	Voltage plateau discharge (V)	Areal capacity (mA h cm ⁻²)	Ref.
S-CNT	25	1.1	—	1400 (1180)	500	0.17	1.3 (Li-In)	1.54 (1.30)	196
Se _{0.05} S _{0.95} @pPAN	~20	1.0	621 (100 mg)	840 (650)	150	0.17	1.3 (Li-In)	0.84 (0.65)	209
Li ₂ S@C	31	2.3	401 (150 mg)	600 (730)	25	0.05	1.5 (Li-In)	1.38 (1.68)	52
S-VGCF	40	1.0 (0.5-1.5)	600	1054 (1035)	100	0.05	2.1 (Li)	1.05 (1.03)	331
S@BP2000	30	0.6	817 (120 mg)	1000 (985)	1200	3.0	1.1 (Li-In)	0.60 (0.59)	203
rGO@S	37.5	1.2	Li ₇ P ₃ S ₁₁	680 (306)	120	0.19	1.5 (Li)	0.82 (0.37)	332
SeS ₂ -AB	40	1.6	LGPS + Li ₃ PS ₄	585 (90 mg)	50	0.08	2.0 (Li)	1.42 (1.25)	120
SeS ₂ -AB	40	15.3	LGPS + Li ₃ PS ₄	823 (823)	10	0.46 (60 °C)	2.0 (Li)	12.6 (11.8)	120
S-C	33	4.3	Li ₆ PS ₃ Cl	600 (800)	50	0.57	1.3 (Li-In)	2.58 (3.44)	210
S@Chovel	40	2.6	Li ₃ PS ₄	1420 (1100)	400	5.2	1.2 (Li-In)	3.69 (2.86)	200
Li ₂ S-KB	25	0.66 (0.57-0.75)	LPS/(MeCN) ₂ -LiTFSI:TTE interlayer (+)	990 (760)	100	0.11	1.2 (Li-In)	0.65 (0.50)	333
S@KB	20	1.28	466 (75 mg)	1017 (840)	50	0.11	2.1 (Li)	1.30 (1.08)	334
PAN-S	20	2.55	400	1682 (775)	100	0.13	2.0 (Li)	4.29 (1.98)	221
Li ₂ S-Li-VGCF	60	3.82	LGPS-PCE interlayer	940 (750)	20	0.32	1.9 (Li)	3.59 (2.86)	335
Li ₂ S-Li-VGCF	60	7.64	75Li ₂ S:25P ₂ S ₅ in Kevlar fiber	912 (450)	20	0.64	1.9 (Li)	6.97 (3.44)	335
Li ₂ S@C	38	1.75	681 (100 mg)	700 (644)	700	2.0 (60 °C)	1.2 (Li-In)	1.23 (1.13)	202
Li ₂ S@C	38	7	681 (100 mg)	950 (1073)	30	0.2 (60 °C)	1.5 (Li-In)	6.65 (7.51)	202
S-C	20	1.6 (1.4-1.8)	Li ₆ PS ₃ Br	1523 (1360)	3	0.13	1.5 (Li-In)	2.44 (2.18)	190
rGO-MoS ₃	—	—	953 (135-145 mg)	673 (414)	500	— (1 A g ⁻¹ in the article)	2.0 (Li)	—	124
rGO-VS ₄	81	2.84	1000	1420 (333)	500	2.37	2.0 (Li)	4.03 (0.95)	336
CNTs@S	13	0.45 (0.4-0.5)	LGPS + 75Li ₂ S-24P ₂ S ₅ -P ₂ O ₅	800 (660)	400	0.75 (60 °C)	2.1 (Li)	0.36 (0.30)	337
S@graphene	25	—	3 wt% BN doped-Li ₇ P ₃ S ₁₁	800 (185)	50	—	1.8 (Li)	—	338
Sulfurized alcohol composite (SAC) rather than S)	38 (SAC ratio rather than S)	5	Li ₃ PS ₄	550 (450)	50	0.15	1.0 (Li-In)	2.75 (2.25)	339
S-C	25	2.55	681 (100 mg)	1602 (1180)	50	0.10	1.5 (Li-In)	4.09 (3.01)	340

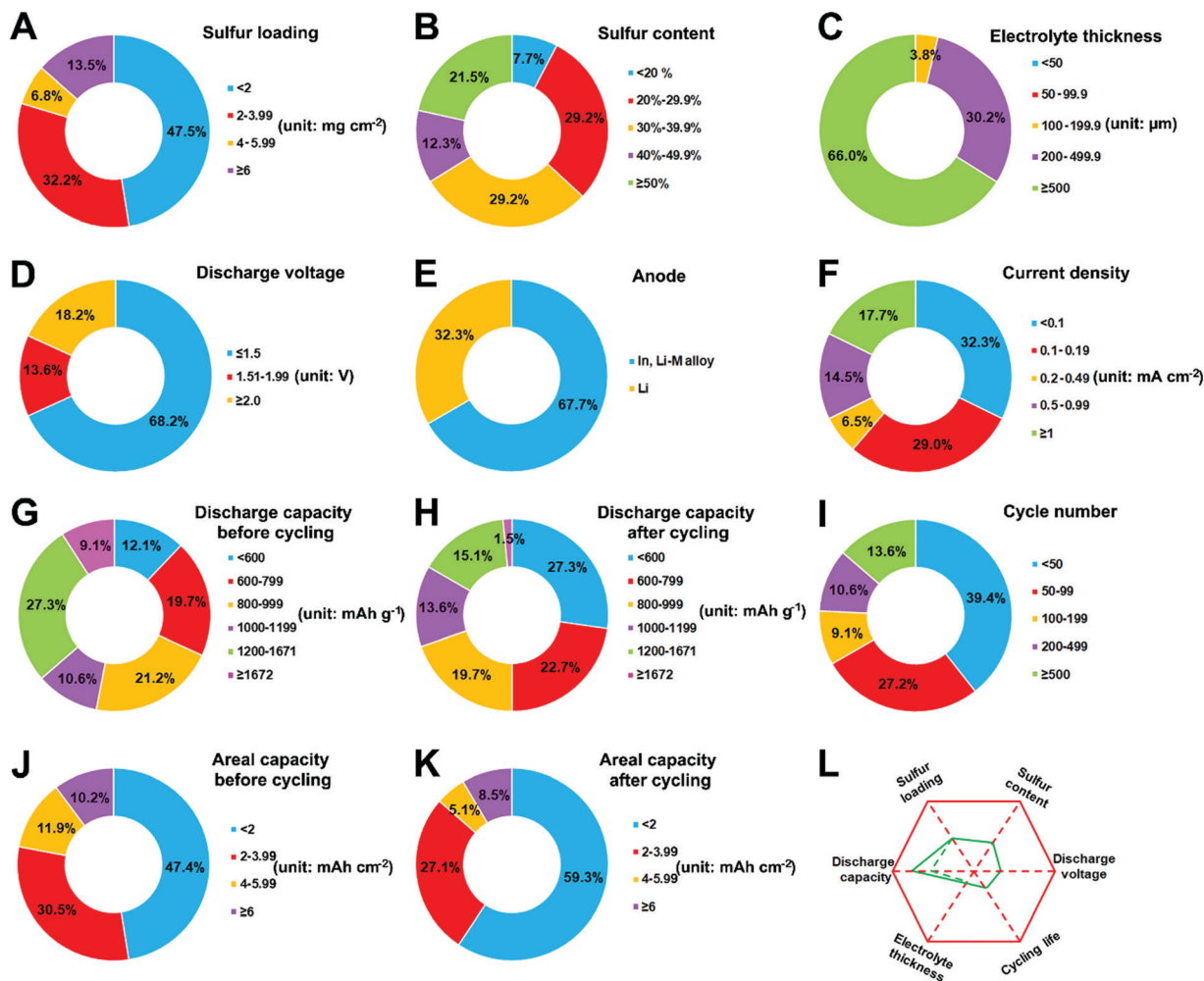


Fig. 22 Statistical analysis of sulfide SSE-based SSLSBs. (A) Sulfur loading, (B) sulfur content, (C) electrolyte thickness, (D) discharge voltage, (E) anode, (F) current density, (G) discharge capacity before cycling, (H) discharge capacity after cycling, (I) cycle number, (J) areal capacity before cycling, and (K) areal capacity after cycling. Spider chart (L) displaying the state of sulfide SSE-based SSLSBs.

SSEs, the large electrode/electrolyte interfacial resistance limits their direct practical application. In most cases, liquid electrolytes are introduced to wet the electrolyte/electrode interface and reduce the interfacial resistance but they result in LiPS formation and LiPSs shuttle as drawbacks. More importantly, the introduction of liquid electrolytes will induce safety issues due to the presence of flammable sulfur, carbon additives, liquid electrolytes as well as highly active metallic Li. In this regard, the amount of liquid electrolyte added should be controlled within a safe range. An ideal strategy should totally replace the liquid electrolytes with a LiPS-insoluble SPE in order to avoid LiPS shuttling. Compared with LAGP and LATP, LLZO shows higher stability against Li metal and LiPSs, which is a promising oxide candidate. However, Li dendrite growth along with grain boundaries and Li₂CO₃ formation on the surface upon exposure to air (H₂O and CO₂) are two issues. On solving the former problem, exploration of advanced pressing and calcination techniques to further increase the tap density and reduce grain boundaries is one direction; the introduction of passivating materials to block the grain boundaries

may be another approach. When the grain boundaries are Li⁺ conductive but electronically insulating, Li deposition along grain boundaries shall be hindered.²⁴² For the latter problem, it is important to develop controllable, facile, and fast Li₂CO₃ removal methods (such as fast acid treatment) to quickly obtain a Li₂CO₃-free pallet.²⁴⁵ Introduction of a lithiophilic coating layer on the fresh surface of LLZO is another method.

Sulfide SSEs possess the highest ionic conductivities among all reported SSEs. Due to the shuttle-free electrochemical process, the sulfide SSE-based SSLSBs exhibit the highest capacity output and capacity retention. However, the poor chemical/electrochemical stabilities are critical challenges for wide practical applications. Most sulfide SSEs are sensitive to air and moisture. They will react with O₂ and H₂O and produce toxic H₂S, which casts safety concerns for SSLSB assembly in a dry room. Hence, developing air- and moisture-stable sulfide SSEs is an urgent and meaningful direction. As summarized in Section 3.4, over 2/3 of sulfide SSE-based SSLSBs use In and Li-M alloy as the anode materials, which significantly limits the energy density due to a higher average potential of 0.6 V vs. Li



Fig. 23 Summary of the requirements for high-energy-density SSLSBs.

metal anodes. The instability of sulfide SSEs against Li metal and poor Li dendrite suppression capability may be the main reasons that limit the usage of Li metal anodes. Therefore, one important future direction is to develop Li metal-compatible sulfide SSEs. Introducing elements such as F, I, and N that can *in situ* form favorable Li-containing SEI (e.g. LiF, LiI and Li₃N) may be a good approach. Last but not least, the development of scalable ultrathin SSE fabrication techniques such as tape-casting, cold/hot-pressing, screen printing and vapor/aerosol deposition to achieve ceramic SSEs with low thicknesses of less than 50 μm is urgent and necessary for high-energy-density SSLSBs.³⁴³

Most reported hybrid electrolytes consist of polymer and oxide SSEs. Depending on the relative contents of oxide SSEs and SPEs, it can be classified into PICs and CIPs. The high-ceramic-content PICs exhibit higher mechanical strength and better Li dendrite suppression capability, while the SPE intensive CIPs show higher flexibility and lower interfacial resistance with electrodes. The rational combination of the merits of the two SSEs is beneficial for simultaneously solving the Li dendrite and interfacial issues.¹⁷⁸ Additionally, the infusion of SPE into a 3D oxide SSE scaffold is another choice to achieve high ionic conductivity as well as mechanical strength. Moreover, the size and concentration of oxide SSE fillers have a huge effect on the ionic conductivity, mechanical strength, interface building and energy density of the SSLSBs, which should be carefully balanced during practical application.

In addition, the exploration of new SSEs should never be neglected. The recently developed SSEs such as halide Li₃YBr₆ and hybrid Li₂(BH₄)(NH₂)·0.7Li(CB₉H₁₀)·0.3Li(CB₁₁H₁₂) with high ionic conductivities (over 10⁻³ S cm⁻¹) and air-/thermal stability should be further explored for their potential for SSLSBs.^{103–106}

Cost plays a crucial role in commercialization. At the current development stage, both oxide- and sulfide-based SSEs are in the early research state for SSLSBs and still far from large-scale commercialization. The price of SSEs is far higher than that of the rest of the components such as the sulfur cathode, binder, carbon additive, lithium metal, *etc.* Therefore, engineering efforts for low-cost SSEs and exploration facile SSE fabrication methods to push the commercialization of SSEs are of significance to decrease the cost of SSLSBs. For polymer electrolytes, the LiTFSI salt is more expensive compared to the PEO polymer. Ways to maintain the ionic conductivity of SPEs with a lower Li salt ratio or search for a more cost-effective Li salt substitute shall be considered. For oxide- and sulfide-based SSEs, replacement of high-cost elements of La and Ge with other low-price elements may be possible. Exploring the solution-based fabrication process to replace the ball-milling method is favorable for large-scale fabrication. Moreover, decreasing the SSEs ratio in the SSLSBs by developing ultrathin SSEs is required.

(3) Anode

Despite the high discharge capacity of metallic Li, the Li dendrite growth and side reactions between the Li metal anode

and SSEs are critical bottlenecks for the development of SSLSBs. Replacing the Li anode with In and Li–M alloys has been demonstrated viable for prolonging the cycling life of SSLSBs due to Li-dendrite free and reduced side reactions. Nevertheless, the higher potential vs. Li/Li⁺ (by ~0.6 V) leads to a low discharge voltage that limits their energy density for pouch cells. The application of a thin In or Li–M alloy coating layer on the surface of the Li anode without obvious reduction in the voltage is worth investigation.

The development of Li protection methods is urgent and necessary for enabling the use of Li metal anodes in SSLSBs. Despite the tremendous efforts and innovations in solving the Li dendrite formation problem (Section 2.3), critical challenges remain. Firstly, it is very difficult to enhance the mechanical strength of SPEs with Young's modulus greater than that of Li metal. Secondly, stable coatings with high ionic conductivities are still challenging. Thirdly, homogeneous Li⁺/e⁻ conductive dual-phase interfaces in a 3D Li anode are scarce. Moreover, for SSLSB pouch cell engineering, the Li excess should be controlled as less than 50 wt%, which urges high Li efficiency.

(4) Characterization techniques and theoretical calculations

Advanced characterization techniques and theoretical calculations are essential for understanding the underlying reaction processes and mechanisms in SSLSBs. Compared with *ex situ* characterization techniques, *in situ* characterization techniques are more informative because of their real-time feature. We strongly recommend the exploration of more *in situ* characterization techniques and wider cooperation between diverse characterization techniques to provide more comprehensive evidence and stronger support to clarify the interfacial behavior. Moreover, theoretical models close to testing conditions (introducing temperature, pressure, voltage, etc) should be set up to achieve more accurate simulation results.

Conflicts of interest

The authors declare no conflicts of interest.

Acknowledgements

This work was partly supported by the Natural Sciences and Engineering Research Council of Canada (NSERC), Canada Research Chair Program (CRC), Canada Foundation for Innovation (CFI), Ontario Research Fund, China Automotive Battery Research Institute Co., Ltd, Glabat Solid-State Battery Inc. and the University of Western Ontario.

References

- 1 A. Manthiram, Y. Fu, S. H. Chung, C. Zu and Y. S. Su, *Chem. Rev.*, 2014, **114**, 11751–11787.
- 2 Z. W. Seh, Y. Sun, Q. Zhang and Y. Cui, *Chem. Soc. Rev.*, 2016, **45**, 5605–5634.
- 3 X. Yang, X. Li, K. Adair, H. Zhang and X. Sun, *Electrochem. Energy Rev.*, 2018, **1**, 239–293.
- 4 S. Zhang, K. Ueno, K. Dokko and M. Watanabe, *Adv. Energy Mater.*, 2015, **5**, 1500117.
- 5 C. Ye, Y. Jiao, H. Jin, A. D. Slattery, K. Davey, H. Wang and S.-Z. Qiao, *Angew. Chem., Int. Ed.*, 2018, **57**, 16703–16707.
- 6 X. Ji, K. T. Lee and L. F. Nazar, *Nat. Mater.*, 2009, **8**, 500–506.
- 7 Z. Wei Seh, W. Li, J. J. Cha, G. Zheng, Y. Yang, M. T. McDowell, P. C. Hsu and Y. Cui, *Nat. Commun.*, 2013, **4**, 1331.
- 8 X. Yang, Y. Yu, X. Lin, J. Liang, K. Adair, Y. Zhao, C. Wang, X. Li, Q. Sun, H. Zhang, X. Li, R. Li, H. Zhang and X. Sun, *J. Mater. Chem. A*, 2018, **6**, 22958–22965.
- 9 J. Gou, H. Zhang, X. Yang, Y. Chen, Y. Yu, X. Li and H. Zhang, *Adv. Funct. Mater.*, 2018, **28**, 1707272.
- 10 X. Yang, N. Yan, W. Zhou, H. Zhang, X. Li and H. Zhang, *J. Mater. Chem. A*, 2015, **3**, 15314–15323.
- 11 C. Ye, L. Zhang, C. Guo, D. Li, A. Vasileff, H. Wang and S.-Z. Qiao, *Adv. Funct. Mater.*, 2017, **27**, 1702524.
- 12 C. Tang, B.-Q. Li, Q. Zhang, L. Zhu, H.-F. Wang, J.-L. Shi and F. Wei, *Adv. Funct. Mater.*, 2016, **26**, 577–585.
- 13 Q. Pang and L. F. Nazar, *ACS Nano*, 2016, **10**, 4111–4118.
- 14 S. Lu, Y. Cheng, X. Wu and J. Liu, *Nano Lett.*, 2013, **13**, 2485–2489.
- 15 S. Moon, Y. H. Jung, W. K. Jung, D. S. Jung, J. W. Choi and D. K. Kim, *Adv. Mater.*, 2013, **25**, 6547–6553.
- 16 S. H. Chung, C. H. Chang and A. Manthiram, *ACS Nano*, 2016, **10**, 10462–10470.
- 17 X. Yang, H. Zhang, Y. Chen, Y. Yu, X. Li and H. Zhang, *Nano Energy*, 2017, **39**, 418–428.
- 18 A. Manthiram, X. Yu and S. Wang, *Nat. Rev. Mater.*, 2017, **2**, 16103.
- 19 H. Wang, X. Cao, W. Liu and X. Sun, *Front. Energy Res.*, 2019, **7**, DOI: 10.3389/fenrg.2019.00112.
- 20 Y. Xia, X. Wang, X. Xia, R. Xu, S. Zhang, J. Wu, Y. Liang, C. Gu and J. Tu, *Chemistry*, 2017, **23**, 15203–15209.
- 21 M. Liu, D. Zhou, Y.-B. He, Y. Fu, X. Qin, C. Miao, H. Du, B. Li, Q.-H. Yang, Z. Lin, T. S. Zhao and F. Kang, *Nano Energy*, 2016, **22**, 278–289.
- 22 M. Liu, H. R. Jiang, Y. X. Ren, D. Zhou, F. Y. Kang and T. S. Zhao, *Electrochim. Acta*, 2016, **213**, 871–878.
- 23 G. G. Eshetu, X. Judez, C. Li, O. Bondarchuk, L. M. Rodriguez-Martinez, H. Zhang and M. Armand, *Angew. Chem., Int. Ed.*, 2017, **56**, 15368–15372.
- 24 J. Lee, J. Song, H. Lee, H. Noh, Y.-J. Kim, S. H. Kwon, S. G. Lee and H.-T. Kim, *ACS Energy Lett.*, 2017, **2**, 1232–1239.
- 25 G. G. Eshetu, X. Judez, C. Li, M. Martinez-Ibanez, I. Gracia, O. Bondarchuk, J. Carrasco, L. M. Rodriguez-Martinez, H. Zhang and M. Armand, *J. Am. Chem. Soc.*, 2018, **140**, 9921–9933.
- 26 L. Sun, H. Li, M. Zhao and G. Wang, *Chem. Eng. J.*, 2018, **332**, 8–15.
- 27 M. Eom, S. Son, C. Park, S. Noh, W. T. Nichols and D. Shin, *Electrochim. Acta*, 2017, **230**, 279–284.
- 28 K. Suzuki, D. Kato, K. Hara, T.-a. Yano, M. Hirayama, M. Hara and R. Kanno, *Electrochim. Acta*, 2017, **258**, 110–115.

- 29 M. Nagao, A. Hayashi, M. Tatsumisago, T. Ichinose, T. Ozaki, Y. Togawa and S. Mori, *J. Power Sources*, 2015, **274**, 471–476.
- 30 H. U. Choi, J. S. Jin, J.-Y. Park and H.-T. Lim, *J. Alloys Compd.*, 2017, **723**, 787–794.
- 31 X. Yao, N. Huang, F. Han, Q. Zhang, H. Wan, J. P. Mwizerwa, C. Wang and X. Xu, *Adv. Energy Mater.*, 2017, **7**, 1602923.
- 32 F. Han, J. Yue, X. Fan, T. Gao, C. Luo, Z. Ma, L. Suo and C. Wang, *Nano Lett.*, 2016, **16**, 4521–4527.
- 33 A. Hayashi, T. Ohtomo, F. Mizuno, K. Tadanaga and M. Tatsumisago, *Electrochem. Commun.*, 2003, **5**, 701–705.
- 34 N. Tanibata, H. Tsukasaki, M. Deguchi, S. Mori, A. Hayashi and M. Tatsumisago, *J. Mater. Chem. A*, 2017, **5**, 11224–11228.
- 35 S. Wang, Y. Zhang, X. Zhang, T. Liu, Y. H. Lin, Y. Shen, L. Li and C. W. Nan, *ACS Appl. Mater. Interfaces*, 2018, **10**, 42279–42285.
- 36 C. Yu, S. Ganapathy, N. J. de Klerk, I. Roslon, E. R. van Eck, A. P. Kentgens and M. Wagemaker, *J. Am. Chem. Soc.*, 2016, **138**, 11192–11201.
- 37 O. Sheng, C. Jin, J. Luo, H. Yuan, C. Fang, H. Huang, Y. Gan, J. Zhang, Y. Xia, C. Liang, W. Zhang and X. Tao, *J. Mater. Chem. A*, 2017, **5**, 12934–12942.
- 38 Y. Lin, X. Wang, J. Liu and J. D. Miller, *Nano Energy*, 2017, **31**, 478–485.
- 39 X. Tao, Y. Liu, W. Liu, G. Zhou, J. Zhao, D. Lin, C. Zu, O. Sheng, W. Zhang, H. W. Lee and Y. Cui, *Nano Lett.*, 2017, **17**, 2967–2972.
- 40 Y. Hao, S. Wang, F. Xu, Y. Liu, N. Feng, P. He and H. Zhou, *ACS Appl. Mater. Interfaces*, 2017, **9**, 33735–33739.
- 41 X. Yu, Z. Bi, F. Zhao and A. Manthiram, *Adv. Energy Mater.*, 2016, **6**, 1601392.
- 42 K. K. Fu, Y. Gong, S. Xu, Y. Zhu, Y. Li, J. Dai, C. Wang, B. Liu, G. Pastel, H. Xie, Y. Yao, Y. Mo, E. Wachsman and L. Hu, *Chem. Mater.*, 2017, **29**, 8037–8041.
- 43 K. K. Fu, Y. Gong, G. T. Hitz, D. W. McOwen, Y. Li, S. Xu, Y. Wen, L. Zhang, C. Wang, G. Pastel, J. Dai, B. Liu, H. Xie, Y. Yao, E. D. Wachsman and L. Hu, *Energy Environ. Sci.*, 2017, **10**, 1568–1575.
- 44 L. Wang, Y. Wang and Y. Xia, *Energy Environ. Sci.*, 2015, **8**, 1551–1558.
- 45 J. Yue, M. Yan, Y.-X. Yin and Y.-G. Guo, *Adv. Funct. Mater.*, 2018, **28**, 1707533.
- 46 X. Yu and A. Manthiram, *Acc. Chem. Res.*, 2017, **50**, 2653–2660.
- 47 Y.-Z. Sun, J.-Q. Huang, C.-Z. Zhao and Q. Zhang, *Sci. China: Chem.*, 2017, **60**, 1508–1526.
- 48 E. Umeshbabu, B. Zheng and Y. Yang, *Electrochem. Energy Rev.*, 2019, **2**, 199–230.
- 49 D. Lei, K. Shi, H. Ye, Z. Wan, Y. Wang, L. Shen, B. Li, Q.-H. Yang, F. Kang and Y.-B. He, *Adv. Funct. Mater.*, 2018, **28**, 1707570.
- 50 Y. Zhu, X. He and Y. Mo, *ACS Appl. Mater. Interfaces*, 2015, **7**, 23685–23693.
- 51 S. P. Ong, Y. Mo, W. D. Richards, L. Miara, H. S. Lee and G. Ceder, *Energy Environ. Sci.*, 2013, **6**, 148–156.
- 52 S. Choi, I. Yoon, W. T. Nichols and D. Shin, *Ceram. Int.*, 2018, **44**, 7450–7453.
- 53 R.-c. Xu, X.-h. Xia, X.-l. Wang, Y. Xia and J.-p. Tu, *J. Mater. Chem. A*, 2017, **5**, 2829–2834.
- 54 J. Liang, J. Luo, Q. Sun, X. Yang, R. Li and X. Sun, *Energy Storage Mater.*, 2019, **21**, 308–334.
- 55 X. Judez, M. Martinez-Ibañez, A. Santiago, M. Armand, H. Zhang and C. Li, *J. Power Sources*, 2019, **438**, 226985.
- 56 X. B. Cheng, R. Zhang, C. Z. Zhao and Q. Zhang, *Chem. Rev.*, 2017, **117**, 10403–10473.
- 57 S. Wenzel, S. Randau, T. Leichtweiß, D. A. Weber, J. Sann, W. G. Zeier and J. R. Janek, *Chem. Mater.*, 2016, **28**, 2400–2407.
- 58 Z. Lin, Z. Liu, N. J. Dudney and C. Liang, *ACS Nano*, 2013, **7**, 2829–2833.
- 59 T. Yamada, S. Ito, R. Omoda, T. Watanabe, Y. Aihara, M. Agostini, U. Ulissi, J. Hassoun and A. B. Scrosati, *J. Electrochem. Soc.*, 2015, **162**, A646–A651.
- 60 Z. Lin, Z. Liu, W. Fu, N. J. Dudney and C. Liang, *Angew. Chem., Int. Ed.*, 2013, **52**, 7460–7463.
- 61 M. Nagao, A. Hayashi and M. Tatsumisago, *Electrochim. Acta*, 2011, **56**, 6055–6059.
- 62 N. Machida, K. Kobayashi, Y. Nishikawa and T. Shigematsu, *Solid State Ionics*, 2004, **175**, 247–250.
- 63 X. Li, J. Liang, X. Li, C. Wang, J. Luo, R. Li and X. Sun, *Energy Environ. Sci.*, 2018, **11**, 2828–2832.
- 64 M. Nagao, A. Hayashi and M. Tatsumisago, *J. Mater. Chem.*, 2012, **22**, 10015–10020.
- 65 Y. Jiang, X. Yan, Z. Ma, P. Mei, W. Xiao, Q. You and Y. Zhang, *Polymers*, 2018, **10**, 1237.
- 66 X. Yang, Q. Sun, C. Zhao, X. Gao, K. Adair, Y. Zhao, J. Luo, X. Lin, J. Liang, H. Huang, L. Zhang, S. Lu, R. Li and X. Sun, *Energy Storage Mater.*, 2019, **22**, 194–199.
- 67 C. Zhang, Y. Lin, Y. Zhu, Z. Zhang and J. Liu, *RSC Adv.*, 2017, **7**, 19231–19236.
- 68 Y. Zhu, J. Li and J. Liu, *J. Power Sources*, 2017, **351**, 17–25.
- 69 X. Li, D. Wang, H. Wang, H. Yan, Z. Gong and Y. Yang, *ACS Appl. Mater. Interfaces*, 2019, **11**, 22745–22753.
- 70 H. Zhang, X. Judez, A. Santiago, M. Martinez-Ibañez, M. Á. Muñoz-Márquez, J. Carrasco, C. Li, G. G. Eshetu and M. Armand, *Adv. Energy Mater.*, 2019, **9**, 1900763.
- 71 Z. Wan, D. Lei, W. Yang, C. Liu, K. Shi, X. Hao, L. Shen, W. Lv, B. Li, Q.-H. Yang, F. Kang and Y.-B. He, *Adv. Funct. Mater.*, 2018, **29**, 1805301.
- 72 C. Wang, Y. Yang, X. Liu, H. Zhong, H. Xu, Z. Xu, H. Shao and F. Ding, *ACS Appl. Mater. Interfaces*, 2017, **9**, 13694–13702.
- 73 X. X. Zeng, Y. X. Yin, N. W. Li, W. C. Du, Y. G. Guo and L. J. Wan, *J. Am. Chem. Soc.*, 2016, **138**, 15825–15828.
- 74 H. Morimoto, H. Awano, J. Terashima, Y. Shindo, S. Nakanishi, N. Ito, K. Ishikawa and S.-I. Tobishima, *J. Power Sources*, 2013, **240**, 636–643.
- 75 D. Safanama, N. Sharma, R. P. Rao, H. E. Brand and S. Adams, *J. Mater. Chem. A*, 2016, **4**, 7718–7726.
- 76 R. Murugan, V. Thangadurai and W. Weppner, *Angew. Chem., Int. Ed.*, 2007, **46**, 7778–7781.
- 77 D. Rettenwander, C. A. Geiger, M. Tribus, P. Tropper, R. Wagner, G. Tippelt, W. Lottermoser and G. Amthauer, *J. Solid State Chem.*, 2015, **230**, 266–271.

- 78 W. J. Kwon, H. Kim, K.-N. Jung, W. Cho, S. H. Kim, J.-W. Lee and M.-S. Park, *J. Mater. Chem. A*, 2017, **5**, 6257–6262.
- 79 A. Hayashi, S. Hama, H. Morimoto, M. Tatsumisago and T. Minami, *J. Am. Ceram. Soc.*, 2001, **84**, 477–479.
- 80 S. Kondo, K. Takada and Y. Yamamura, *Solid State Ionics*, 1992, **53**, 1183–1186.
- 81 Y. Seino, T. Ota, K. Takada, A. Hayashi and M. Tatsumisago, *Energy Environ. Sci.*, 2014, **7**, 627–631.
- 82 N. Kamaya, K. Homma, Y. Yamakawa, M. Hirayama, R. Kanno, M. Yonemura, T. Kamiyama, Y. Kato, S. Hama, K. Kawamoto and A. Mitsui, *Nat. Mater.*, 2011, **10**, 682–686.
- 83 Y. Kato, S. Hori, T. Saito, K. Suzuki, M. Hirayama, A. Mitsui, M. Yonemura, H. Iba and R. Kanno, *Nat. Energy*, 2016, **1**, 16030.
- 84 A. Kuhn, O. Gerbig, C. Zhu, F. Falkenberg, J. Maier and B. V. Lotsch, *Phys. Chem. Chem. Phys.*, 2014, **16**, 14669–14674.
- 85 R. Xu, Z. Wu, S. Zhang, X. Wang, Y. Xia, X. Xia, X. Huang and J. Tu, *Chemistry*, 2017, **23**, 13950–13956.
- 86 P. Bron, S. Johansson, K. Zick, J. Schmedt auf der Gunne, S. Dehnen and B. Roling, *J. Am. Chem. Soc.*, 2013, **135**, 15694–15697.
- 87 J. E. Weston and B. C. H. Steele, *Solid State Ionics*, 1982, **7**, 75–79.
- 88 F. Croce, L. Persi, F. Ronci and B. Scrosati, *Solid State Ionics*, 2000, **135**, 47–52.
- 89 C. W. Lin, C. L. Hung, M. Venkateswarlu and B. J. Hwang, *J. Power Sources*, 2005, **146**, 397–401.
- 90 S. Jayanthi, K. Kulasekarapandian, A. Arulsankar, K. Sankaranarayanan and B. Sundaresan, *J. Compos. Mater.*, 2014, **49**, 1035–1045.
- 91 W. Liu, D. Lin, J. Sun, G. Zhou and Y. Cui, *ACS Nano*, 2016, **10**, 11407–11413.
- 92 J. L. Schaefer, D. A. Yanga and L. A. Archer, *Chem. Mater.*, 2013, **25**, 834–839.
- 93 C. Z. Zhao, X. Q. Zhang, X. B. Cheng, R. Zhang, R. Xu, P. Y. Chen, H. J. Peng, J. Q. Huang and Q. Zhang, *Proc. Natl. Acad. Sci. U. S. A.*, 2017, **114**, 11069–11074.
- 94 A. M. Stephan, T. P. Kumar, M. A. Kulandainathan and N. A. Laksh, *J. Phys. Chem. B*, 2009, **113**, 1963–1971.
- 95 W. Wang, E. Yi, A. J. Fici, R. M. Laine and J. Kieffe, *J. Phys. Chem. C*, 2017, **121**, 2563–2573.
- 96 K. K. Fu, Y. Gong, J. Dai, A. Gong, X. Han, Y. Yao, C. Wang, Y. Wang, Y. Chen, C. Yan, Y. Li, E. D. Wachsman and L. Hu, *Proc. Natl. Acad. Sci. U. S. A.*, 2016, **113**, 7094–7099.
- 97 T. Yang, J. Zheng, Q. Cheng, Y. Y. Hu and C. K. Chan, *ACS Appl. Mater. Interfaces*, 2017, **9**, 21773–21780.
- 98 Y. Zhao, C. Wu, G. Peng, X. Chen, X. Yao, Y. Bai, F. Wu, S. Chen and X. Xu, *J. Power Sources*, 2016, **301**, 47–53.
- 99 Z. Zhang, Y. Zhao, S. Chen, D. Xie, X. Yao, P. Cui and X. Xu, *J. Mater. Chem. A*, 2017, **5**, 16984–16993.
- 100 R. Schlem, S. Muy, N. Prinz, A. Banik, Y. Shao-Horn, M. Zobel and W. G. Zeier, *Adv. Energy Mater.*, 2019, 1903719.
- 101 X. Li, J. Liang, J. Luo, M. Norouzi Banis, C. Wang, W. Li, S. Deng, C. Yu, F. Zhao, Y. Hu, T.-K. Sham, L. Zhang, S. Zhao, S. Lu, H. Huang, R. Li, K. R. Adair and X. Sun, *Energy Environ. Sci.*, 2019, **12**, 2665–2671.
- 102 X. Li, J. Liang, N. Chen, J. Luo, K. R. Adair, C. Wang, M. N. Banis, T. K. Sham, L. Zhang, S. Zhao, S. Lu, H. Huang, R. Li and X. Sun, *Angew. Chem., Int. Ed.*, 2019, **58**, 16427–16432.
- 103 S. Wang, Q. Bai, A. M. Nolan, Y. Liu, S. Gong, Q. Sun and Y. Mo, *Angew. Chem., Int. Ed.*, 2019, **58**, 8039–8043.
- 104 T. Asano, A. Sakai, S. Ouchi, M. Sakaida, A. Miyazaki and S. Hasegawa, *Adv. Mater.*, 2018, **30**, 1803075.
- 105 S. Kim, H. Oguchi, N. Toyama, T. Sato, S. Takagi, T. Otomo, D. Arunkumar, N. Kuwata, J. Kawamura and S. I. Orimo, *Nat. Commun.*, 2019, **10**, 1081.
- 106 M. Matsuo, A. Remhof, P. Martelli, R. Caputo, M. Ernst, Y. Miura, T. Sato, H. Oguchi, H. Maekawa, H. Takamura, A. Borgschulte, A. Zuttel and S. Orimo, *J. Am. Chem. Soc.*, 2009, **131**, 16389–16391.
- 107 X. Yang, Y. Yu, N. Yan, H. Zhang, X. Li and H. Zhang, *J. Mater. Chem. A*, 2016, **4**, 5965–5972.
- 108 W. Ai, W. Zhou, Z. Du, Y. Chen, Z. Sun, C. Wu, C. Zou, C. Li, W. Huang and T. Yu, *Energy Storage Mater.*, 2017, **6**, 112–118.
- 109 Z. Guo, B. Zhang, D. Li, T. Zhao, P. R. Coxon, C. J. Harris, R. Hao, Y. Liu, K. Xi and X. Li, *Electrochim. Acta*, 2017, **230**, 181–188.
- 110 D. S. Jung, T. H. Hwang, J. H. Lee, H. Y. Koo, R. A. Shakoor, R. Kahraman, Y. N. Jo, M. S. Park and J. W. Choi, *Nano Lett.*, 2014, **14**, 4418–4425.
- 111 X. Gao, X. Yang, Q. Sun, J. Luo, J. Liang, W. Li, J. Wang, S. Wang, M. Li, R. Li, T.-K. Sham and X. Sun, *Energy Storage Mater.*, 2020, (24), 682–688.
- 112 X. Gao, Q. Sun, X. Yang, J. Liang, A. Koo, W. Li, J. Liang, J. Wang, R. Li, F. B. Holness, A. D. Price, S. Yang, T.-K. Sham and X. Sun, *Nano Energy*, 2019, **56**, 595–603.
- 113 J. Wang, J. Yang, J. Xie and N. Xu, *Adv. Mater.*, 2002, **14**, 963–965.
- 114 J. Fanous, M. Wegner, J. Grimminger, Å. Andresen and M. R. Buchmeiser, *Chem. Mater.*, 2011, **23**, 5024–5028.
- 115 G. Hu, Z. Sun, C. Shi, R. Fang, J. Chen, P. Hou, C. Liu, H. M. Cheng and F. Li, *Adv. Mater.*, 2017, **29**, 201603835.
- 116 W. J. Chung, J. J. Griebel, E. T. Kim, H. Yoon, A. G. Simmonds, H. J. Ji, P. T. Dirlam, R. S. Glass, J. J. Wie, N. A. Nguyen, B. W. Guralnick, J. Park, A. Somogyi, P. Theato, M. E. Mackay, Y. E. Sung, K. Char and J. Pyun, *Nat. Chem.*, 2013, **5**, 518–524.
- 117 H. Kim, J. Lee, H. Ahn, O. Kim and M. J. Park, *Nat. Commun.*, 2015, **6**, 7278.
- 118 S. Zeng, L. Li, L. Xie, D. Zhao, N. Zhou, N. Wang and S. Chen, *Carbon*, 2017, **122**, 106–113.
- 119 X. Yao, D. Liu, C. Wang, P. Long, G. Peng, Y. S. Hu, H. Li, L. Chen and X. Xu, *Nano Lett.*, 2016, **16**, 7148–7154.
- 120 X. Li, J. Liang, J. Luo, C. Wang, X. Li, Q. Sun, R. Li, L. Zhang, R. Yang, S. Lu, H. Huang and X. Sun, *Adv. Mater.*, 2019, **31**, 1808100.
- 121 M. Pan, T. Hakari, A. Sakuda, A. Hayashi, Y. Suginata, S. Mori and M. Tatsumisago, *Electrochemistry*, 2018, **86**, 175–178.

- 122 T. Matsuyama, A. Hayashi, T. Ozaki, S. Morib and M. Tatsumisago, *J. Mater. Chem. A*, 2015, **3**, 14142–14147.
- 123 T. Matsuyama, M. Deguchi, A. Hayashi, M. Tatsumisago, T. Ozaki, Y. Togawa and S. Mori, *Electrochemistry*, 2015, **83**, 889–893.
- 124 Q. Zhang, Z. Ding, G. Liu, H. Wan, J. P. Mwizerwa, J. Wu and X. Yao, *Energy Storage Mater.*, 2019, **13**, 168–180.
- 125 X. Yang, Y. Chen, M. Wang, H. Zhang, X. Li and H. Zhang, *Adv. Funct. Mater.*, 2016, **26**, 8427–8434.
- 126 X. Gao, X. Yang, M. Li, Q. Sun, J. Liang, J. Luo, J. Wang, W. Li, J. Liang, Y. Liu, S. Wang, Y. Hu, Q. Xiao, R. Li, T.-K. Sham and X. Sun, *Adv. Funct. Mater.*, 2019, **29**, 1806724.
- 127 A. Jozwiuk, B. B. Berkes, T. Weiß, H. Sommer, J. Janek and T. Brezesinski, *Energy Environ. Sci.*, 2016, **9**, 2603–2608.
- 128 H. M. Chen, C. Maohua and S. Adams, *Phys. Chem. Chem. Phys.*, 2015, **17**, 16494–16506.
- 129 F. Han, T. Gao, Y. Zhu, K. J. Gaskell and C. Wang, *Adv. Mater.*, 2015, **27**, 3473–3483.
- 130 T. Hakari, M. Deguchi, K. Mitsuhara, T. Ohta, K. Saito, Y. Orikasa, Y. Uchimoto, Y. Kowada, A. Hayashi and M. Tatsumisago, *Chem. Mater.*, 2017, **29**, 4768–4774.
- 131 Y. Liu, Q. Sun, Y. Zhao, B. Wang, P. Kaghazchi, K. R. Adair, R. Li, C. Zhang, J. Liu, L. Y. Kuo, Y. Hu, T. K. Sham, L. Zhang, R. Yang, S. Lu, X. Song and X. Sun, *ACS Appl. Mater. Interfaces*, 2018, **10**, 31240–31248.
- 132 S. Wenzel, T. Leichtweiss, D. Krüger, J. Sann and J. Janek, *Solid State Ionics*, 2015, **278**, 98–105.
- 133 D.-W. Wang, Q. Zeng, G. Zhou, L. Yin, F. Li, H.-M. Cheng, I. R. Gentle and G. Q. M. Lu, *J. Mater. Chem. A*, 2013, **1**, 9382–9394.
- 134 M. Helen, M. A. Reddy, T. Diemant, U. Golla-Schindler, R. J. Behm, U. Kaiser and M. Fichtner, *Sci. Rep.*, 2015, **5**, 12146.
- 135 K. Zhang, Q. Zhao, Z. Tao and J. Chen, *Nano Res.*, 2012, **6**, 38–46.
- 136 H. Li, D. Chao, B. Chen, X. Chen, C. Chuah, Y. Tang, Y. Jiao, M. Jaroniec and S. Z. Qiao, *J. Am. Chem. Soc.*, 2020, **142**, 2012–2022.
- 137 X. Gao, X. Yang, K. Adair, X. Li, J. Liang, Q. Sun, Y. Zhao, R. Li, T. K. Sham and X. Sun, *Adv. Energy Mater.*, 2020, 1903753.
- 138 S. Liu, N. Imanishi, T. Zhang, A. Hirano, Y. Takeda, O. Yamamoto and J. Yang, *J. Electrochem. Soc.*, 2010, **157**, A1092–A1098.
- 139 F. Shen, M. B. Dixit, X. Xiao and K. B. Hatzell, *ACS Energy Lett.*, 2018, **3**, 1056–1061.
- 140 K. K. Fu, Y. Gong, B. Liu, Y. Zhu, S. Xu, Y. Yao, W. Luo, C. Wang, S. D. Lacey, J. Dai, Y. Chen, Y. Mo, E. Wachsman and L. Hu, *Sci. Adv.*, 2017, **3**, e1601659.
- 141 Y. X. Yin, S. Xin, Y. G. Guo and L. J. Wan, *Angew. Chem., Int. Ed.*, 2013, **52**, 13186–13200.
- 142 W. Zhou, Y. Yu, H. Chen, F. J. DiSalvo and H. D. Abruna, *J. Am. Chem. Soc.*, 2013, **135**, 16736–16743.
- 143 X. B. Cheng, T. Z. Hou, R. Zhang, H. J. Peng, C. Z. Zhao, J. Q. Huang and Q. Zhang, *Adv. Mater.*, 2016, **28**, 2888–2895.
- 144 L. Xu, S. Tang, Y. Cheng, K. Wang, J. Liang, C. Liu, Y.-C. Cao, F. Wei and L. Mai, *Joule*, 2018, **2**, 1991–2015.
- 145 W. Yang, W. Yang, J. Feng, Z. Ma and G. Shao, *Electrochim. Acta*, 2016, **210**, 71–78.
- 146 Q. Ma, X. Qi, B. Tong, Y. Zheng, W. Feng, J. Nie, Y. S. Hu, H. Li, X. Huang, L. Chen and Z. Zhou, *ACS Appl. Mater. Interfaces*, 2016, **8**, 29705–29712.
- 147 J. Liang, Q. Sun, Y. Zhao, Y. Sun, C. Wang, W. Li, M. Li, D. Wang, X. Li, Y. Liu, K. Adair, R. Li, L. Zhang, R. Yang, S. Lu, H. Huang and X. Sun, *J. Mater. Chem. A*, 2018, **6**, 23712–23719.
- 148 J. L. Wang, J. Yang, J. Y. Xie, N. X. Xu and Y. Li, *Electrochem. Commun.*, 2002, **4**, 499–502.
- 149 X. Yu, J. Xie, J. Yang and K. Wang, *J. Power Sources*, 2004, **132**, 181–186.
- 150 Q. Pang, X. Liang, C. Y. Kwok and L. F. Nazar, *Nat. Energy*, 2016, **1**, 16132.
- 151 S. Xin, L. Gu, N. H. Zhao, Y. X. Yin, L. J. Zhou, Y. G. Guo and L. J. Wan, *J. Am. Chem. Soc.*, 2012, **134**, 18510–18513.
- 152 S. Z. Niu, W. Lv, C. Zhang, Y. T. Shi, J. F. Zhao, B. H. Li, Q. H. Yang and F. Y. Kang, *J. Power Sources*, 2015, **295**, 182–189.
- 153 C. Luo, Y. Zhu, Y. Wen, J. Wang and C. Wang, *Adv. Funct. Mater.*, 2014, **24**, 4082–4089.
- 154 X. Li, A. Lushington, Q. Sun, W. Xiao, J. Liu, B. Wang, Y. Ye, K. Nie, Y. Hu, Q. Xiao, R. Li, J. Guo, T. K. Sham and X. Sun, *Nano Lett.*, 2016, **16**, 3545–3549.
- 155 X. Li, M. Banis, A. Lushington, X. Yang, Q. Sun, Y. Zhao, C. Liu, Q. Li, B. Wang, W. Xiao, C. Wang, M. Li, J. Liang, R. Li, Y. Hu, L. Goncharova, H. Zhang, T. K. Sham and X. Sun, *Nat. Commun.*, 2018, **9**, 4509.
- 156 Z. W. Seh, Q. Zhang, W. Li, G. Zheng, H. Yao and Y. Cui, *Chem. Sci.*, 2013, **4**, 3673–3677.
- 157 D.-D. Han, S. Liu, Y.-T. Liu, Z. Zhang, G.-R. Li and X.-P. Gao, *J. Mater. Chem. A*, 2018, **6**, 18627–18634.
- 158 M. Rao, X. Li, Y. Liao, X. Li and W. Li, *Ionics*, 2015, **21**, 1937–1943.
- 159 S. Gao, K. Wang, R. Wang, M. Jiang, J. Han, T. Gu, S. Cheng and K. Jiang, *J. Mater. Chem. A*, 2017, **5**, 17889–17895.
- 160 J. Hu, J. Tian and C. Li, *ACS Appl. Mater. Interfaces*, 2017, **9**, 11615–11625.
- 161 Z. Jin, K. Xie, X. Hong, Z. Hu and X. Liu, *J. Power Sources*, 2012, **218**, 163–167.
- 162 L. Li, Y. Chen, X. Guo and B. Zhong, *Polym. Chem.*, 2015, **6**, 1619–1626.
- 163 Y. Sun, G. Li, Y. Lai, D. Zeng and H. Cheng, *Sci. Rep.*, 2016, **6**, 22048.
- 164 H. Marceau, C.-S. Kim, A. Paoletta, S. Ladouceur, M. Lagacé, M. Chaker, A. Vijh, A. Guerfi, C. M. Julien, A. Mauger, M. Armand, P. Hovington and K. Zaghib, *J. Power Sources*, 2016, **319**, 247–254.
- 165 Y.-X. Song, Y. Shi, J. Wan, S.-Y. Lang, X.-C. Hu, H.-J. Yan, B. Liu, Y.-G. Guo, R. Wen and L.-J. Wan, *Energy Environ. Sci.*, 2019, **12**, 2496–2506.
- 166 X. Judez, H. Zhang, C. Li, J. A. Gonzalez-Marcos, Z. Zhou, M. Armand and L. M. Rodriguez-Martinez, *J. Phys. Chem. Lett.*, 2017, **8**, 1956–1960.

- 167 H. Ben youcef, O. Garcia-Calvo, N. Lago, S. Devaraj and M. Armand, *Electrochim. Acta*, 2016, **220**, 587–594.
- 168 Y. Lin, J. Li, K. Liu, Y. Liu, J. Liu and X. Wang, *Green Chem.*, 2016, **18**, 3796–3803.
- 169 K. Zhu, Y. Liu and J. Liu, *RSC Adv.*, 2014, **4**, 42278–42284.
- 170 Z. Wang, S. Wang, A. Wang, X. Liu, J. Chen, Q. Zeng, L. Zhang, W. Liu and L. Zhang, *J. Mater. Chem. A*, 2018, **6**, 17227–17234.
- 171 C. Zhang, Y. Lin and J. Liu, *J. Mater. Chem. A*, 2015, **3**, 10760–10766.
- 172 Y. Li, W. Zhang, Q. Dou, K. W. Wong and K. M. Ng, *J. Mater. Chem. A*, 2019, **7**, 3391–3398.
- 173 W. Liu, N. Liu, J. Sun, P. C. Hsu, Y. Li, H. W. Lee and Y. Cui, *Nano Lett.*, 2015, **15**, 2740–2745.
- 174 W. Liu, S. W. Lee, D. Lin, F. Shi, S. Wang, A. D. Sendek and Y. Cui, *Nat. Energy*, 2017, **2**, 17035.
- 175 H. Zhai, P. Xu, M. Ning, Q. Cheng, J. Mandal and Y. Yang, *Nano Lett.*, 2017, **17**, 3182–3187.
- 176 J. Bae, Y. Li, J. Zhang, X. Zhou, F. Zhao, Y. Shi, J. B. Goodenough and G. Yu, *Angew. Chem., Int. Ed.*, 2018, **57**, 2096–2100.
- 177 X. Judez, H. Zhang, C. Li, G. G. Eshetu, Y. Zhang, J. A. Gonzalez-Marcos, M. Armand and L. M. Rodriguez-Martinez, *J. Phys. Chem. Lett.*, 2017, **8**, 3473–3477.
- 178 H. Huo, Y. Chen, J. Luo, X. Yang, X. Guo and X. Sun, *Adv. Energy Mater.*, 2019, **9**, 1804004.
- 179 J. Wu, Z. Rao, Z. Cheng, L. Yuan, Z. Li and Y. Huang, *Adv. Energy Mater.*, 2019, **9**, 1902767.
- 180 J. Wan, J. Xie, X. Kong, Z. Liu, K. Liu, F. Shi, A. Pei, H. Chen, W. Chen, J. Chen, X. Zhang, L. Zong, J. Wang, L. Q. Chen, J. Qin and Y. Cui, *Nat. Nanotechnol.*, 2019, **14**, 705–711.
- 181 Q. Wang, J. Jin, X. Wu, G. Ma, J. Yang and Z. Wen, *Phys. Chem. Chem. Phys.*, 2014, **16**, 21225–21229.
- 182 X. Yu, Z. Bi, F. Zhao and A. Manthiram, *ACS Appl. Mater. Interfaces*, 2015, **7**, 16625–16631.
- 183 S. Gu, X. Huang, Q. Wang, J. Jin, Q. Wang, Z. Wen and R. Qian, *J. Mater. Chem. A*, 2017, **5**, 13971–13975.
- 184 S. Wang, Y. Ding, G. Zhou, G. Yu and A. Manthiram, *ACS Energy Lett.*, 2016, **1**, 1080–1085.
- 185 S. Xu, D. W. McOwen, L. Zhang, G. T. Hitz, C. Wang, Z. Ma, C. Chen, W. Luo, J. Dai, Y. Kuang, E. M. Hitz, K. Fu, Y. Gong, E. D. Wachsman and L. Hu, *Energy Storage Mater.*, 2018, **15**, 458–464.
- 186 Z. Jiang, S. Wang, X. Chen, W. Yang, X. Yao, X. Hu, Q. Han and H. Wang, *Adv. Mater.*, 2019, 1906221.
- 187 R.-c. Xu, X.-h. Xia, S.-h. Li, S.-z. Zhang, X.-l. Wang and J.-p. Tu, *J. Mater. Chem. A*, 2017, **5**, 6310–6317.
- 188 S. Kinoshita, K. Okuda, N. Machida, M. Naito and T. Sigematsu, *Solid State Ionics*, 2014, **256**, 97–102.
- 189 C. Yu, L. van Eijck, S. Ganapathy and M. Wagemaker, *Electrochim. Acta*, 2016, **215**, 93–99.
- 190 C. Yu, J. Hageman, S. Ganapathy, L. van Eijck, L. Zhang, K. R. Adair, X. Sun and M. Wagemaker, *J. Mater. Chem. A*, 2019, **7**, 10412–10421.
- 191 H. Nagata and Y. Chikusa, *J. Power Sources*, 2014, **263**, 141–144.
- 192 K. Suzuki, D. Kato, K. Hara, T.-A. Yano, M. Hirayama, M. Hara and R. Kanno, *Electrochemistry*, 2018, **86**, 1–5.
- 193 M. Nagao, A. Hayashi and M. Tatsumisago, *Energy Technol.*, 2013, **1**, 186–192.
- 194 Y. Wang, D. Lu, M. Bowden, P. Z. El Khoury, K. S. Han, Z. D. Deng, J. Xiao, J.-G. Zhang and J. Liu, *Chem. Mater.*, 2018, **30**, 990–997.
- 195 H.-R. Yao, Y.-X. Yin and Y.-G. Guo, *Chin. Phys. B*, 2016, **25**, 018203.
- 196 Y. Zhang, T. Liu, Q. Zhang, X. Zhang, S. Wang, X. Wang, L. Li, L.-Z. Fan, C.-W. Nan and Y. Shen, *J. Mater. Chem. A*, 2018, **6**, 23345–23356.
- 197 Y. Zhao, Y. Zhang, Z. Bakenov and P. Chen, *Solid State Ionics*, 2013, **234**, 40–45.
- 198 A. Fu, C. Wang, F. Pei, J. Cui, X. Fang and N. Zheng, *Small*, 2019, **15**, 1804786.
- 199 J. Liang, Z.-H. Sun, F. Li and H.-M. Cheng, *Energy Storage Mater.*, 2016, **2**, 76–106.
- 200 A. Sakuda, Y. Sato, A. Hayashi and M. Tatsumisago, *Energy Technol.*, 2019, **7**, 1900077.
- 201 M. Nagao, Y. Imade, H. Narisawa, T. Kobayashi, R. Watanabe, T. Yokoi, T. Tatsumi and R. Kanno, *J. Power Sources*, 2013, **222**, 237–242.
- 202 H. Yan, H. Wang, D. Wang, X. Li, Z. Gong and Y. Yang, *Nano Lett.*, 2019, **19**, 3280–3287.
- 203 Q. Han, X. Li, X. Shi, H. Zhang, D. Song, F. Ding and L. Zhang, *J. Mater. Chem. A*, 2019, **7**, 3895–3902.
- 204 T. A. Yersak, S.-B. Son, J. S. Cho, S.-S. Suh, Y.-U. Kim, J.-T. Moon, K. H. Oh and S.-H. Lee, *J. Electrochem. Soc.*, 2013, **160**, A1497–A1501.
- 205 W. Zhang, D. Schröder, T. Arlt, I. Manke, R. Koerver, R. Pinedo, D. A. Weber, J. Sann, W. G. Zeier and J. Janek, *J. Mater. Chem. A*, 2017, **5**, 9929–9936.
- 206 W. Zhang, D. A. Weber, H. Weigand, T. Arlt, I. Manke, D. Schroder, R. Koerver, T. Leichtweiss, P. Hartmann, W. G. Zeier and J. Janek, *ACS Appl. Mater. Interfaces*, 2017, **9**, 17835–17845.
- 207 R. Koerver, W. Zhang, L. de Biasi, S. Schweidler, A. O. Kondrakov, S. Kolling, T. Brezesinski, P. Hartmann, W. G. Zeier and J. Janek, *Energy Environ. Sci.*, 2018, **11**, 2142–2158.
- 208 K. Suzuki, N. Mashimo, Y. Ikeda, T. Yokoi, M. Hirayama and R. Kanno, *ACS Appl. Energy Mater.*, 2018, **1**, 2373–2377.
- 209 Y. Zhang, Y. Sun, L. Peng, J. Yang, H. Jia, Z. Zhang, B. Shan and J. Xie, *Energy Storage Mater.*, 2018, **21**, 287–296.
- 210 S. Ohno, R. Koerver, G. Dewald, C. Rosenbach, P. Titscher, D. Steckermeier, A. Kwade, J. Janek and W. G. Zeier, *Chem. Mater.*, 2019, **31**, 2930–2940.
- 211 H. Chung and B. Kang, *Chem. Mater.*, 2017, **29**, 8611–8619.
- 212 J. Lau, R. H. DeBlock, D. M. Butts, D. S. Ashby, C. S. Choi and B. S. Dunn, *Adv. Energy Mater.*, 2018, **8**, 1800933.
- 213 C. Wang, Y. Zhao, Q. Sun, X. Li, Y. Liu, J. Liang, X. Li, X. Lin, R. Li, K. R. Adair, L. Zhang, R. Yang, S. Lu and X. Sun, *Nano Energy*, 2018, **53**, 168–174.
- 214 B. Wang, J. Liu, Q. Sun, R. Li, T. K. Sham and X. Sun, *Nanotechnology*, 2014, **25**, 504007.

- 215 Y. Zhao, K. Zheng and X. Sun, *Joule*, 2018, **2**, 2583–2604.
- 216 W. Zhou, S. Wang, Y. Li, S. Xin, A. Manthiram and J. B. Goodenough, *J. Am. Chem. Soc.*, 2016, **138**, 9385–9388.
- 217 G. Hou, X. Ma, Q. Sun, Q. Ai, X. Xu, L. Chen, D. Li, J. Chen, H. Zhong, Y. Li, Z. Xu, P. Si, J. Feng, L. Zhang, F. Ding and L. Ci, *ACS Appl. Mater. Interfaces*, 2018, **10**, 18610–18618.
- 218 Z. Zhang, S. Chen, J. Yang, J. Wang, L. Yao, X. Yao, P. Cui and X. Xu, *ACS Appl. Mater. Interfaces*, 2018, **10**, 2556–2565.
- 219 Y. Gao, D. Wang, Y. C. Li, Z. Yu, T. E. Mallouk and D. Wang, *Angew. Chem., Int. Ed.*, 2018, **57**, 13608–13612.
- 220 Q. Cheng, A. Li, N. Li, S. Li, A. Zangiabadi, T.-D. Li, W. Huang, A. C. Li, T. Jin, Q. Song, W. Xu, N. Ni, H. Zhai, M. Dontigny, K. Zaghbi, X. Chuan, D. Su, K. Yan and Y. Yang, *Joule*, 2019, **3**, 1510–1522.
- 221 C. Wang, K. R. Adair, J. Liang, X. Li, Y. Sun, X. Li, J. Wang, Q. Sun, F. Zhao, X. Lin, R. Li, H. Huang, L. Zhang, R. Yang, S. Lu and X. Sun, *Adv. Funct. Mater.*, 2019, **29**, 1900392.
- 222 K. Nie, Y. Hong, J. Qiu, Q. Li, X. Yu, H. Li and L. Chen, *Front. Chem.*, 2018, **6**, 616.
- 223 D. Santhanagopalan, D. Qian, T. McGilvray, Z. Wang, F. Wang, F. Camino, J. Graetz, N. Dudney and Y. S. Meng, *J. Phys. Chem. Lett.*, 2014, **5**, 298–303.
- 224 K. Park, B.-C. Yu, J.-W. Jung, Y. Li, W. Zhou, H. Gao, S. Son and J. B. Goodenough, *Chem. Mater.*, 2016, **28**, 8051–8059.
- 225 F. Walther, R. Koerver, T. Fuchs, S. Ohno, J. Sann, M. Rohnke, W. G. Zeier and J. Janek, *Chem. Mater.*, 2019, **31**, 3745–3755.
- 226 B. Wu, S. Wang, J. Lochala, D. Desrochers, B. Liu, W. Zhang, J. Yang and J. Xiao, *Energy Environ. Sci.*, 2018, **11**, 1803–1810.
- 227 T. Okumura, T. Nakatsutsumi, T. Ina, Y. Orikasa, H. Arai, T. Fukutsuka, Y. Iriyama, T. Uruga, H. Tanida, Y. Uchimoto and Z. Ogumi, *J. Mater. Chem.*, 2011, **21**, 10051–10060.
- 228 J. Y. Liang, X. X. Zeng, X. D. Zhang, P. F. Wang, J. Y. Ma, Y. X. Yin, X. W. Wu, Y. G. Guo and L. J. Wan, *J. Am. Chem. Soc.*, 2018, **140**, 6767–6770.
- 229 C. Yu, S. Ganapathy, E. Eck, H. Wang, S. Basak, Z. Li and M. Wagemaker, *Nat. Commun.*, 2017, **8**, 1086.
- 230 S. Ganapathy, C. Yu, E. R. H. van Eck and M. Wagemaker, *ACS Energy Lett.*, 2019, **4**, 1092–1097.
- 231 C. Ma, Y. Cheng, K. Yin, J. Luo, A. Sharafi, J. Sakamoto, J. Li, K. L. More, N. J. Dudney and M. Chi, *Nano Lett.*, 2016, **16**, 7030–7036.
- 232 Z. Wang, D. Santhanagopalan, W. Zhang, F. Wang, H. L. Xin, K. He, J. Li, N. Dudney and Y. S. Meng, *Nano Lett.*, 2016, **16**, 3760–3767.
- 233 Y. Gong, J. Zhang, L. Jiang, J. A. Shi, Q. Zhang, Z. Yang, D. Zou, J. Wang, X. Yu, R. Xiao, Y. S. Hu, L. Gu, H. Li and L. Chen, *J. Am. Chem. Soc.*, 2017, **139**, 4274–4277.
- 234 K. N. Wood, K. X. Steirer, S. E. Hafner, C. Ban, S. Santhanagopalan, S.-H. Lee and G. Teeter, *Nat. Commun.*, 2018, **9**, 2490.
- 235 B. Tsuchiya, J. Ohnishi, Y. Sasaki, T. Yamamoto, Y. Yamamoto, M. Motoyama, Y. Iriyama and K. Morita, *Adv. Mater. Interfaces*, 2019, **6**, 1900100.
- 236 X. Wu, C. Villevieille, P. Novák and M. E. Kazzi, *Phys. Chem. Chem. Phys.*, 2018, **20**, 11123–11129.
- 237 Z. Liu, G. Li, A. Borodin, X. Liu, Y. Li and F. Endres, *J. Solid State Electrochem.*, 2019, **23**, 2107–2117.
- 238 C. Wang, X. Li, Y. Zhao, M. N. Banis, J. Liang, X. Li, Y. Sun, K. R. Adair, Q. Sun, Y. Liu, F. Zhao, S. Deng, X. Lin, R. Li, Y. Hu, T. K. Sham, H. Huang, L. Zhang, R. Yang, S. Lu and X. Sun, *Small Methods*, 2019, **3**, 1900261.
- 239 C. Wang, Y. Gong, J. Dai, L. Zhang, H. Xie, G. Pastel, B. Liu, E. Wachsman, H. Wang and L. Hu, *J. Am. Chem. Soc.*, 2017, **139**, 14257–14264.
- 240 P. H. Chien, X. Feng, M. Tang, J. T. Rosenberg, S. O'Neill, J. Zheng, S. C. Grant and Y. Y. Hu, *J. Phys. Chem. Lett.*, 2018, **9**, 1990–1998.
- 241 H. Masuda, N. Ishida, Y. Ogata, D. Ito and D. Fujita, *Nanoscale*, 2017, **9**, 893–898.
- 242 F. Han, A. S. Westover, J. Yue, X. Fan, F. Wang, M. Chi, D. N. Leonard, N. J. Dudney, H. Wang and C. Wang, *Nat. Energy*, 2019, **4**, 187–196.
- 243 K. Romanenko, L. Jin, P. Howlett and M. Forsyth, *Chem. Mater.*, 2016, **28**, 2844–2851.
- 244 A. M. Nolan, Y. Zhu, X. He, Q. Bai and Y. Mo, *Joule*, 2018, **2**, 2016–2046.
- 245 H. Huo, Y. Chen, N. Zhao, X. Lin, J. Luo, X. Yang, Y. Liu, X. Guo and X. Sun, *Nano Energy*, 2019, **61**, 119–125.
- 246 A. Sharafi, S. Yu, M. Naguib, M. Lee, C. Ma, H. M. Meyer, J. Nanda, M. Chi, D. J. Siegel and J. Sakamoto, *J. Mater. Chem. A*, 2017, **5**, 13475–13487.
- 247 L. Cheng, E. J. Crumlin, W. Chen, R. Qiao, H. Hou, S. Franz Lux, V. Zorba, R. Russo, R. Kostecki, Z. Liu, K. Persson, W. Yang, J. Cabana, T. Richardson, G. Chen and M. Doeff, *Phys. Chem. Chem. Phys.*, 2014, **16**, 18294–18300.
- 248 A. Sharafi, E. Kazyak, A. L. Davis, S. Yu, T. Thompson, D. J. Siegel, N. P. Dasgupta and J. Sakamoto, *Chem. Mater.*, 2017, **29**, 7961–7968.
- 249 K. Takada, N. Ohta, L. Zhang, K. Fukuda, I. Sakaguchi, R. Ma, M. Osada and T. Sasaki, *Solid State Ionics*, 2008, **179**, 1333–1337.
- 250 K. Takada, *Langmuir*, 2013, **29**, 7538–7541.
- 251 N. Ohta, K. Takada, L. Zhang, R. Ma, M. Osada and T. Sasaki, *Adv. Mater.*, 2006, **18**, 2226–2229.
- 252 J. Haruyama, K. Sodeyama, L. Han, K. Takada and Y. Tateyama, *Chem. Mater.*, 2014, **26**, 4248–4255.
- 253 M. Sumita, Y. Tanaka, M. Ikeda and T. Ohno, *J. Phys. Chem. C*, 2016, **120**, 13332–13339.
- 254 R. Xu, F. Han, X. Ji, X. Fan, J. Tu and C. Wang, *Nano Energy*, 2018, **53**, 958–966.
- 255 M. Sumita, Y. Tanaka, M. Ikeda and T. Ohno, *J. Phys. Chem. C*, 2014, **119**, 14–22.
- 256 S. Panahian Jand and P. Kaghazchi, *MRS Commun.*, 2018, **8**, 591–596.
- 257 R. Sudo, Y. Nakata, K. Ishiguro, M. Matsui, A. Hirano, Y. Takeda, O. Yamamoto and N. Imanishi, *Solid State Ionics*, 2014, **262**, 151–154.
- 258 X.-B. Cheng, C.-Z. Zhao, Y.-X. Yao, H. Liu and Q. Zhang, *Chem*, 2019, **5**, 74–96.
- 259 Y. Zhu, J. Cao, H. Chen, Q. Yu and B. Li, *J. Mater. Chem. A*, 2019, **7**, 6832–6839.

- 260 K. Park, J. H. Cho, K. Shanmuganathan, J. Song, J. Peng, M. Gobet, S. Greenbaum, C. J. Ellison and J. B. Goodenough, *J. Power Sources*, 2014, **263**, 52–58.
- 261 X. Ban, W. Zhang, N. Chen and C. Sun, *J. Phys. Chem. C*, 2018, **122**, 9852–9858.
- 262 X. Yang, Q. Sun, C. Zhao, X. Gao, K. R. Adair, Y. Liu, J. Luo, X. Lin, J. Liang, H. Huang, L. Zhang, R. Yang, S. Lu, R. Li and X. Sun, *Nano Energy*, 2019, **61**, 567–575.
- 263 D. Lin, P. Y. Yuen, Y. Liu, W. Liu, N. Liu, R. H. Dauskardt and Y. Cui, *Adv. Mater.*, 2018, **30**, 1802661.
- 264 L. Chen, Y. Li, S.-P. Li, L.-Z. Fan, C.-W. Nan and J. B. Goodenough, *Nano Energy*, 2018, **46**, 176–184.
- 265 V. Chaudoy, F. Ghamouss, E. Luais and F. Tran-Van, *Ind. Eng. Chem. Res.*, 2016, **55**, 9925–9933.
- 266 S. Choudhury, R. Mangal, A. Agrawal and L. A. Archer, *Nat. Commun.*, 2015, **6**, 10101.
- 267 I. Kim, B. S. Kim, S. Nam, H. J. Lee, H. K. Chung, S. M. Cho, T. H. T. Luu, S. Hyun and C. Kang, *Materials*, 2018, **11**, 543.
- 268 K.-H. Lee, K.-H. Kim and H. S. Lim, *J. Electrochem. Soc.*, 2001, **148**, A1148–A1152.
- 269 Q. Lu, J. Fang, J. Yang, G. Yan, S. Liu and J. Wang, *J. Membr. Sci.*, 2013, **425–426**, 105–112.
- 270 C. Ma, J. Zhang, M. Xu, Q. Xia, J. Liu, S. Zhao, L. Chen, A. Pan, D. G. Ivey and W. Wei, *J. Power Sources*, 2016, **317**, 103–111.
- 271 L. Porcarelli, C. Gerbaldi, F. Bella and J. R. Nair, *Sci. Rep.*, 2016, **6**, 19892.
- 272 T. Sakakibara, M. Kitamura, T. Honma, H. Kohno, T. Uno, M. Kubo, N. Imanishi, Y. Takeda and T. Itoh, *Electrochim. Acta*, 2019, **296**, 1018–1026.
- 273 W. K. Shin, J. Cho, A. G. Kannan, Y. S. Lee and D. W. Kim, *Sci. Rep.*, 2016, **6**, 26332.
- 274 D. Zhang, L. Zhang, K. Yang, H. Wang, C. Yu, D. Xu, B. Xu and L. M. Wang, *ACS Appl. Mater. Interfaces*, 2017, **9**, 36886–36896.
- 275 J. Zhang, X. Li, Y. Li, H. Wang, C. Ma, Y. Wang, S. Hu and W. Wei, *Front. Chem.*, 2018, **6**, 186.
- 276 K. Zhao, H. Song, X. Duan, Z. Wang, J. Liu and X. Ba, *Polymers*, 2019, **11**, 444.
- 277 Y. Zhang, W. Lu, L. Cong, J. Liu, L. Sun, A. Mauger, C. M. Julien, H. Xie and J. Liu, *J. Power Sources*, 2019, **420**, 63–72.
- 278 Z. Fan, B. Ding, T. Zhang, Q. Lin, V. Malgras, J. Wang, H. Dou, X. Zhang and Y. Yamauchi, *Small*, 2019, **15**, 1903952.
- 279 Q. Zhao, P. Chen, S. Li, X. Liu and L. A. Archer, *J. Mater. Chem. A*, 2019, **7**, 7823–7830.
- 280 S.-S. Chi, Y. Liu, N. Zhao, X. Guo, C.-W. Nan and L.-Z. Fan, *Energy Storage Mater.*, 2019, **17**, 309–316.
- 281 Y. Liu, D. Lin, Y. Jin, K. Liu, X. Tao, Q. Zhang, I. Zhang and Y. Cui, *Sci. Adv.*, 2017, **3**, eaao0713.
- 282 C. Yang, L. Zhang, B. Liua, S. Xu, T. Hamann, D. McOwen, J. Dai, W. Luo, Y. Gong, E. D. Wachsman and L. Hu, *Proc. Natl. Acad. Sci. U. S. A.*, 2018, **115**, 3770–3775.
- 283 D. W. McOwen, S. Xu, Y. Gong, Y. Wen, G. L. Godbey, J. E. Gritton, T. R. Hamann, J. Dai, G. T. Hitz, L. Hu and E. D. Wachsman, *Adv. Mater.*, 2018, **30**, 1707132.
- 284 M. Du, K. Liao, Q. Lu and Z. Shao, *Energy Environ. Sci.*, 2019, **12**, 1780–1804.
- 285 H. Huo, Y. Chen, R. Li, N. Zhao, J. Luo, J. G. Pereira da Silva, R. Mücke, P. Kaghazchi, X. Guo and X. Sun, *Energy Environ. Sci.*, 2020, **13**, 127–134.
- 286 H. Duan, Y. X. Yin, Y. Shi, P. F. Wang, X. D. Zhang, C. P. Yang, J. L. Shi, R. Wen, Y. G. Guo and L. J. Wan, *J. Am. Chem. Soc.*, 2018, **140**, 82–85.
- 287 X. Han, Y. Gong, K. K. Fu, X. He, G. T. Hitz, J. Dai, A. Pearse, B. Liu, H. Wang, G. Rubloff, Y. Mo, V. Thangadurai, E. D. Wachsman and L. Hu, *Nat. Mater.*, 2017, **16**, 572–579.
- 288 J. Fu, P. Yu, N. Zhang, G. Ren, S. Zheng, W. Huang, X. Long, H. Li and X. Liu, *Energy Environ. Sci.*, 2019, **12**, 1404–1412.
- 289 Y. Ruan, Y. Lu, X. Huang, J. Su, C. Sun, J. Jin and Z. Wen, *J. Mater. Chem. A*, 2019, **7**, 14565–14574.
- 290 X. Judez, H. Zhang, C. Li, G. G. Eshetu, J. E. A. González-Marcos, M. Armand and L. M. Rodríguez-Martínez, *J. Electrochem. Soc.*, 2018, **165**, A6008–A6016.
- 291 R. Fang, S. Zhao, Z. Sun, D. W. Wang, H. M. Cheng and F. Li, *Adv. Mater.*, 2017, **29**, 1606823.
- 292 R. Fang, S. Zhao, P. Hou, M. Cheng, S. Wang, H. M. Cheng, C. Liu and F. Li, *Adv. Mater.*, 2016, **28**, 3374–3382.
- 293 X. Yang, X. Gao, Q. Sun, S. P. Jand, Y. Yu, Y. Zhao, X. Li, K. Adair, L. Y. Kuo, J. Rohrer, J. Liang, X. Lin, M. N. Banis, Y. Hu, H. Zhang, X. Li, R. Li, H. Zhang, P. Kaghazchi, T. K. Sham and X. Sun, *Adv. Mater.*, 2019, **31**, 1901220.
- 294 Y. J. Nam, S. J. Cho, D. Y. Oh, J. M. Lim, S. Y. Kim, J. H. Song, Y. G. Lee, S. Y. Lee and Y. S. Jung, *Nano Lett.*, 2015, **15**, 3317–3323.
- 295 J. M. Whiteley, P. Taynton, W. Zhang and S.-H. Lee, *Adv. Mater.*, 2015, **27**, 6922–6927.
- 296 T. Hakari, M. Nagao, A. Hayashi and M. Tatsumisago, *Solid State Ionics*, 2014, **262**, 147–150.
- 297 T. Hakari, M. Nagao, A. Hayashi and M. Tatsumisago, *J. Power Sources*, 2015, **293**, 721–725.
- 298 B. R. Shin, Y. J. Nam, J. W. Kim, Y. G. Lee and Y. S. Jung, *Sci. Rep.*, 2014, **4**, 5572.
- 299 T. Hakari, Y. Sato, S. Yoshimi, A. Hayashi and M. Tatsumisago, *J. Electrochem. Soc.*, 2017, **164**, A2804–A2811.
- 300 Y. Zhang, R. Chen, T. Liu, B. Xu, X. Zhang, L. Li, Y. Lin, C. W. Nan and Y. Shen, *ACS Appl. Mater. Interfaces*, 2018, **10**, 10029–10035.
- 301 H. Nagata and Y. Chikusa, *Energy Technol.*, 2016, **4**, 484–489.
- 302 J. Hassoun and B. Scrosati, *Adv. Mater.*, 2010, **22**, 5198–5201.
- 303 H. Zhang, U. Oteo, X. Judez, G. G. Eshetu, M. Martínez-Ibañez, J. Carrasco, C. Li and M. Armand, *Joule*, 2019, **3**, 1689–1702.
- 304 J. Gao, C. Sun, L. Xu, J. Chen, C. Wang, D. Guo and H. Chen, *J. Power Sources*, 2018, **382**, 179–189.
- 305 L. Chen and L. Z. Fan, *Energy Storage Mater.*, 2018, **15**, 37–45.

- 306 S. Suriyakumar, S. Gopi, M. Kathiresan, S. Bose, E. B. Gowd, J. R. Nair, N. Angulakshmi, G. Meligrana, F. Bella, C. Gerbaldi and A. M. Stephan, *Electrochim. Acta*, 2018, **285**, 355–364.
- 307 P. Zhu, C. Yan, J. Zhu, J. Zang, Y. Li, H. Jia, X. Dong, Z. Du, C. Zhang, N. Wu, M. Dirican and X. Zhang, *Energy Storage Mater.*, 2019, **17**, 220–225.
- 308 J. Liu, T. Qian, M. Wang, J. Zhou, N. Xu and C. Yan, *Nano Lett.*, 2018, **18**, 4598–4605.
- 309 J. Hassoun and B. Scrosati, *Angew. Chem., Int. Ed.*, 2010, **49**, 2371–2374.
- 310 S.-J. Cho, G. Y. Jung, S. H. Kim, M. Jang, D.-K. Yang, S. K. Kwak and S.-Y. Lee, *Energy Environ. Sci.*, 2019, **12**, 559–565.
- 311 D. D. Han, Z. Y. Wang, G. L. Pan and X. P. Gao, *ACS Appl. Mater. Interfaces*, 2019, **11**, 18427–18435.
- 312 X. Wang, X. Hao, Y. Xia, Y. Liang, X. Xia and J. Tu, *J. Membr. Sci.*, 2019, **582**, 37–47.
- 313 Y. Xia, Y. F. Liang, D. Xie, X. L. Wang, S. Z. Zhang, X. H. Xia, C. D. Gu and J. P. Tu, *Chem. Eng. J.*, 2019, **358**, 1047–1053.
- 314 D. Yang, L. He, Y. Liu, W. Yan, S. Liang, Y. Zhu, L. Fu, Y. Chen and Y. Wu, *J. Mater. Chem. A*, 2019, **7**, 13679–13686.
- 315 J. Zhou, H. Ji, J. Liu, T. Qian and C. Yan, *Energy Storage Mater.*, 2019, **22**, 256–264.
- 316 C. Long, L. Li, M. Zhai and Y. Shan, *J. Phys. Chem. Solids*, 2019, **134**, 255–261.
- 317 S. H. Kim, J. H. Kim, S. J. Cho and S. Y. Lee, *Adv. Energy Mater.*, 2019, **9**, 1901841.
- 318 X. Cai, B. Cui, B. Ye, W. Wang, J. Ding and G. Wang, *ACS Appl. Mater. Interfaces*, 2019, **11**, 38136–38146.
- 319 B. Sun, K. Liu, J. Lang, M. Fang, Y. Jin and H. Wu, *Electrochim. Acta*, 2018, **284**, 662–668.
- 320 D. Bosubabu, J. Sivaraj, R. Sampathkumar and K. Ramesha, *ACS Appl. Energy Mater.*, 2019, **2**, 4118–4125.
- 321 A. Hayashi, R. Ohtsubo, T. Ohtomo, F. Mizuno and M. Tatsumisago, *J. Power Sources*, 2008, **183**, 422–426.
- 322 M. Nagao, A. Hayashi and M. Tatsumisago, *Electrochem. Commun.*, 2012, **22**, 177–180.
- 323 T. A. Yersak, C. Stoldt and S.-H. Lee, *J. Electrochem. Soc.*, 2013, **160**, A1009–A1015.
- 324 M. Chen and S. Adams, *J. Solid State Electrochem.*, 2014, **19**, 697–702.
- 325 H. Nagata and Y. Chikusa, *Energy Technol.*, 2014, **2**, 753–756.
- 326 A. Sakuda, N. Taguchi, T. Takeuchi, H. Kobayashi, H. Sakaebe, K. Tatsumi and Z. Ogumi, *Solid State Ionics*, 2014, **262**, 143–146.
- 327 T. Hakari, A. Hayashi and M. Tatsumisago, *Chem. Lett.*, 2015, **44**, 1664–1666.
- 328 W. J. Li, M. Hirayama, K. Suzuki and R. Kanno, *Mater. Trans.*, 2016, **57**, 549–552.
- 329 Y. Zhang, K. Chen, Y. Shen, Y. Lin and C.-W. Nan, *Solid State Ionics*, 2017, **305**, 1–6.
- 330 Q. Ge, L. Zhou, Y.-M. Lian, X. Zhang, R. Chen and W. Yang, *Electrochem. Commun.*, 2018, **97**, 100–104.
- 331 Y. Cao, P. Zuo, S. Lou, Z. Sun, Q. Li, H. Huo, Y. Ma, C. Du, Y. Gao and G. Yin, *J. Mater. Chem. A*, 2019, **7**, 6533–6542.
- 332 A. Kizilaslan and H. Akbulut, *ChemPlusChem*, 2019, **84**, 183–189.
- 333 M. Shin and A. A. Gewirth, *Adv. Energy Mater.*, 2019, **9**, 1900938.
- 334 E. Umeshbabu, B. Zheng, J. Zhu, H. Wang, Y. Li and Y. Yang, *ACS Appl. Mater. Interfaces*, 2019, **11**, 18436–18447.
- 335 R. Xu, J. Yue, S. Liu, J. Tu, F. Han, P. Liu and C. Wang, *ACS Energy Lett.*, 2019, **4**, 1073–1079.
- 336 Q. Zhang, H. Wan, G. Liu, Z. Ding, J. P. Mwizerwa and X. Yao, *Nano Energy*, 2019, **57**, 771–782.
- 337 Q. Zhang, N. Huang, Z. Huang, L. Cai, J. Wu and X. Yao, *J. Energy Chem.*, 2020, **40**, 151–155.
- 338 X. Xu, L. Wang, H. Fei and L. Ci, *J. Mater. Sci.: Mater. Electron.*, 2019, **30**, 19119–19125.
- 339 T. Takeuchi, T. Kojima, H. Kageyama, H. Kobayashi, K. Mitsuhashi, K. Nakanishi and T. Ohta, *Energy Technol.*, 2019, **7**, 1900509.
- 340 J. Yi, L. Chen, Y. Liu, H. Geng and L. Z. Fan, *ACS Appl. Mater. Interfaces*, 2019, **11**, 36774–36781.
- 341 B. W. Zhang, T. Sheng, Y. X. Wang, S. Chou, K. Davey, S. X. Dou and S. Z. Qiao, *Angew. Chem., Int. Ed.*, 2019, **58**, 1484–1488.
- 342 C. Ye, Y. Jiao, D. Chao, T. Ling, J. Shan, B. Zhang, Q. Gu, K. Davey, H. Wang and S.-Z. Qiao, *Adv. Mater.*, 2020, DOI: 10.1002/adma.201907557.
- 343 J. Schnell, T. Günther, T. Knoche, C. Vieider, L. Köhler, A. Just, M. Keller, S. Passerini and G. Reinhart, *J. Power Sources*, 2018, **382**, 160–175.